TÉCNICO LISBOA

Numerical and Experimental Analysis of a Slingsby Firefly Light Aircraft

Ana Filipa Oliveira das Neves

Thesis to obtain the Master of Science Degree in

Mechanical Engineering

Supervisors: Prof. Luís Rego da Cunha de Eça
Prof. Nicholas Lawson

Examination Committee

Chairperson: Prof. Carlos Frederico Neves Bettencourt da Silva
Supervisor: Prof. Luís Rego da Cunha de Eça
Member of the Committee: Prof. João Manuel Melo de Sousa

November 2019

Dedicated to my Mom and Dad.

Acknowledgments

I would like to express my gratitude to Professor Nicholas Lawson and Dr. Christopher Bennett for the opportunity of developing this thesis and for their continuous support throughout the project.

I also wish to thank Professor Luís Eça for his support, guidance in the present work and for teaching me to think critically.

To my parents who have supported all my decisions even if that meant being away from home to follow my dreams. They taught me that with hard-work everything is possible. They were my biggest motivation and kept me sane throughout this project.

I would like to thank my friends, specially Miguel and Sofia who shared this journey with me since the very beginning of the Mechanical Engineering Course.

To João for his unconditional support, patience and for always believing in me when I could not.

Lastly I would like to thank Leonardo Da Vinci for inspiring me to become an engineer.

Resumo

A presente dissertação estuda o fenómeno de perda aerodinâmica de um avião acrobático, Slingsby Firefly T67 M260. O objetivo é obter o ângulo de ataque crítico, o coeficiente de sustentação máximo, o padrão de separação da camada limite na superfície superior da asa e a frequência da libertação de vórtices que gera o buffet.

De modo a alcançar os objetivos, análise numérica com Computational Fluid Dynamics (CFD) e ensaios em voo foram realizados. O modelo de turbulência RANS $k-\omega$ SST foi aplicado a um modelo computacional representativo do Slingsby com diversos ângulos de ataque estudados, em condições pré e pós perda. Estes estudos em CFD permitiram obter o ângulo de ataque e o coeficiente de sustentação críticos e o padrão de separação da camada limite. Adicionalmente, o modelo Detached-Eddy Simulation com $k-\omega$ SST, foi aplicado aos estudos previamente obtidos com RANS, particularmente em condições pós-perda, com o objetivo de determinar a frequência de libertação de vórtices. A frequência foi obtida com a monitorização da pressão estática em diversos pontos na esteira da asa.

Os resultados obtidos com CFD foram comparados com diversos ensaios em voo. Voos retilíneos, horizontais em regime estabilizado para diferentes velocidades foram realizados para obter o coeficiente de sustentação em função do ângulo de ataque. A superfície da asa foi também coberta por tiras de lã para visualização do escoamento. A frequência de buffet foi monitorizada com o auxílio de acelerómetros que foram implementados no cockpit Esta foi comparada com a frequência de libertação de vórtices.

Palavras-chave: Perda, Avião, CFD, Libertação de vórtices, Ensaios em voo.

Abstract

This work aims at investigating the stall characteristics of a light aircraft, more specifically the Slingsby Firefly T67M260. The objective was to obtain critical angle of attack, maximum lift coefficient, flow patterns visualisation of the boundary layer separation and vortex shedding frequency.

In order to accomplish these objectives, both CFD and flight tests were performed. The RANS $k-\omega$ SST turbulence model was applied to half-model of the aircraft and a range of angles of attack were studied, pre and post-stall angles of attack. These flow calculations allowed for the identification of the critical angle of attack and respective maximum lift coefficient and the flow visualisation of the boundary layer separation pattern on the upper surface of the wing. In addition, Detached-Eddy Simulations, with $k-\omega$ SST, were performed for the stall condition and post-stall with the objective of computing the vortex shedding frequency. This was accomplished by monitoring the static pressure at several probes in the wing's wake and the lift coefficient.

In order to evaluate the quality of the results, several flight tests were performed. Straight and level flights were performed at different speeds in order to determine the lift coefficient of the aircraft as a function of the angle of attack. In addition, wool tufts were implemented on the upper surface of the wing to visualise the pattern of the flow separation. Moreover, the aircraft was stalled and the buffet frequency was recorded with accelerometers inside the cockpit in order to compare it with the vortex shedding frequency.

Keywords: Stall, Aircraft, CFD, Vortex Shedding, Flight tests.

Contents

List of Tables

List of Figures

Nomenclature

Greek symbols

α	Angle of attack.
α_0	Zero lift angle.
α_{stall}	Critical angle of attack.
β	Angle of a reference line in the fuselage.
$\delta_{i,j}$	Kronecker delta.
ϵ	Turbulent dissipation.
γ	Flight path angle.
λ	Taper Ratio.
μ	Molecular viscosity coefficient.
μ_t	Eddy viscosity.
ν	Kinematic Viscosity.
ω	Specific turbulent dissipation rate.
$\Omega_{i,j}$	Mean of rotation tensor.
ϕ	Inclinometer angle.
ρ	Density.
σ	Thrust angle.
τ_{ij}	Reynolds stress tensor.
θ	Pitch angle.
$\widetilde{\nu}$	Kinematic Eddy Viscosity.

Roman symbols

$\overline{c}$	Mean aerodynamic chord.

τ_w	Wall shear stress.
b	Wing Span.
C_D	Coefficient of drag.
C_f	Skin friction coefficient.
C_L	Coefficient of lift.
C_M	Coefficient of moment.
C_{Lmax}	Coefficient of lift.
c_{root}	Root chord.
c_{tip}	Tip chord.
Cp	Pressure Coefficient.
f	Frequency.
f_{vs}	Vortex Shedding Frequency.
h	Specific Enthalpy.
k	Turbulence kinetic energy.
L_a	Length of the aircraft.
m	Meters.
n	Normal component.
P_{static}	Static Pressure.
q_j	Convective heat flux.
$s_{i,j}$	Strain-rate tensor.
St	Strouhal Number.
St	Wing Area.
$t_{i,j}$	Viscous Tensor.
u_i	Cartesian velocity components.
x_i	Cartesian directions.
y^+	Dimensionless wall distance.
$Æ$	Aspect Ratio.
c	Chord.

D	Drag Force.
K	Kelvin.
L	Lift Force.
P	Power.
Pa	Pascal.
Re	Reynolds Number.
T	Thrust.
t	Thickness.
p	Pressure.
$\mathbf{u}$	Velocity vector.
u, v, w	Velocity Cartesian components.

List of Abbreviations

AOPA Aircraft Owners and Pilots Association. 7

AUSM Advection Upstream Splitting Method. 40

AoA Angle of attack. 10, 16, 43, 45, 46, 75

BSL Baseline. 27

CAD Computer-aided design. 31

CFD Computational Fluids Dynamics.. xi, xii, 2, 4, 18, 19, 21, 31, 32, 39, 41, 51, 55, 56, 62–64, 66, 68, 75, 76

CFL Courant–Friedrichs–Lewy. 18, 40

DES Detached-Eddy Simulation. 20–22, 27–29, 34, 38, 41, 51, 76

DNS Direct Numerical Simulation. 20, 21

EASA European Aviation Safety Agency. 7

ESDU Engineering Sciences Data Unit. 11

FDS Flux-difference splitting. 40

FFT Fast-Fourier Transform. 48, 68

IAS Indicated Airspeed. 44

IBM International Business Machines. 18

IGES Initial Graphics Exchange Specification. 2, 31

ISA International Standard Atmosphere. 41

LES Large-Eddy Simulation. 2, 20, 21

NACA National Advisory Committee for Aeronautics. 5, 6

NSE Navier-Stokes Equations. 23

QDNS Quasi-Direct Numerical Simulation. 21

RANS Reynolds-Averaged Navier-Stokes. 2, 4, 20–22, 40, 51, 68, 76

TAS True Airspeed. 44

TDPF Tail Damping Power Factor. 6

TDR Tail-Damping Ratio. 6

URANS Unsteady Reynolds-Averaged Navier-Stokes. 20–22

URVC Unshielded Rudder Volume Coefficient. 6

Chapter 1

Introduction

1.1 Motivation

Stall and Spin have received continuous attention from the aeronautical industry since the early flight days [1]. Spin is an autorotating descent in an helical pattern about the vertical axis. In order for this to occur the aircraft must be stalled, i.e., the critical angle of attack (α_{stall}) is exceeded. The α_{stall} is the angle after which increasing the angle of attack will no longer result in an increase in lift. At high angles of attack, the adverse pressure gradients on the upper surface of the wing often result in the boundary layer separation [2]. If approximately 50% of the boundary layer on the upper surface of the wing is separated, a further increase in the angle of attack results in a loss of lift and a massive increase in drag [3]. Usually, before stall occurs a natural stall warning takes place, buffet, which is a consequence of the vortex shedding resultant from the separated flow of the wing [4]. Buffet has a characteristic frequency which ought to be known due to structural requirements. The complex separated flow resultant from a stalled aircraft, which is still poorly understood owing to its unsteadiness, three-dimensionality and configuration dependence, often results in a design challenge.

The stall characteristics of an aircraft are required to comply with the regulations in order for the aircraft to be certified. The latter depend on several components of the aircraft and its study as a whole is usually only accomplished with flight tests. However, flight tests are performed in a later design stage of an aircraft. Thus performing changes to comply with stall requirements, at the flight tests stage, is often costly and might not even be implemented due to time concerns [3]. Hence, it is of utmost importance that the stalling behaviour of an aircraft is understood, from an aerodynamics and structural dynamics point of view, from an early design stage.

The wing of an aircraft is the main component that affects how a stall will develop since it is the main lift device, for instance how the flow separation develops on the upper surface of the wing. Ergo, the design of an aircraft usually begins by defining the planform and aerofoil section(s) of the wing and its structural requirements. Frequently, the objective is to have an aircraft with good performance, fair stall characteristics and a structural design that prioritizes low weight. The knowledge of the maximum lift coefficient (C_{Lmax}), α_{stall} and development of the boundary layer separation is of utmost importance

in order to understand how an aircraft will stall. In addition, the wing's structure must be designed in order to endure the vortex induced vibrations when approaching stall, hence the buffet frequency ought to be known.

The design of an aircraft with acceptable stall behaviour is accomplished by understanding the previously mentioned stall characteristics. In the early days, these were often analysed with theory, data gathered from wind-tunnel testing and flight tests. In fact, in order to understand the required design changes of an aircraft, wool tufts on the upper surface of the wing and stall related vibrations, i.e., buffet would be monitored in flight tests [3] .

In the past decades, Computational Fluid Dynamics (CFD) has started to be applied as a complementary design and analysis tool to the ones referred previously. Although wind-tunnel testing is able to provide data in a greater range of flight envelope it often fails to meet the flight test conditions, moreover it is more costly and time-consuming. Flight tests are usually performed in a later stage, and used rather as a validation tool not as a design tool. In addition, it represents a tremendous cost and hazard to the test pilots. Thus, CFD is gaining relevance in the aeronautical industry due to its lower cost when compared to the standard design and validation tools and required time, which is a very important constraint. Moreover, it gives information of the flow properties in all the flow field [5]. Nevertheless, this does not mean that wind-tunnel and flight test should be eliminated, but rather that CFD should be used as a complementary tool.

Ultimately, the design of an aircraft where its stall characteristics are fully understood represents a current challenge for the aeronautical industry, hence the importance of acquiring knowledge about its stall characteristics from an early design stage.

1.1.1 Aim of the thesis

The project of an aircraft where the stall characteristics are known from an early design stage is still a challenge in industry. This is owing to the complexity of the phenomenon and tools available to understand it. An accurate understanding of the stall characteristics of an aircraft from an early design change will prevent later and costly modifications to the design.

Owing to what was stated, the present work evaluates the application of CFD, more specifically a widely used steady Reynolds-Averaged Navier-Stokes (RANS) turbulence model and a recent hybrid RANS/Large-Eddy Simulation (LES) model. The aim is to understand if CFD can be applied as an early design tool for the understanding of the aerodynamic stall characteristics of an aircraft, representing an alternative to the standard methods used (wind-tunnel and flight tests).

In order to accomplish this, a qualitative study was performed of certain aerodynamic features of a light aircraft, the Slingsby Firefly T67M260. This aircraft was chosen due to the existence of an accurate Initial Graphics Exchange Specification (IGES) file and the possibility of performing flight tests in order to evaluate the quality of the results obtained with CFD.

The Slingsby Firefly T67M260 is a two seat aerobatic training aircraft with a six-cylinder, 260 horsepower (191.22 kW) normally aspirated engine with fuel injection and inverted lubrication for aerobatic use [6], these technical specifications can be seen in table 1.1. The aircraft's wing is straight

tapered with geometric twist and dihedral. The aerofoils sections of the wing's root and tip are different, NACA 23015 and NACA 23013, respectively. The geometric specifications referred above are described in more detail in table 1.2. The flying controls are conventional consisting of ailerons, elevator and rudder operated via pushrods and cables, figure 1.1 illustrates the flying controls. Since 2012, this aircraft is operated by the National Flying Laboratory Centre at Cranfield University, as a supplement to the Scottish Aviation Bulldog. They are used for pilots' training and for the MSc students flight experience.

(a) Cranfield University Slingsby Firefly T67M260.

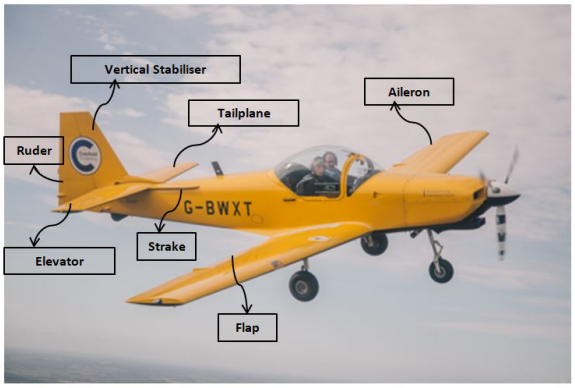

(b) Slingsby Firefly T67M260 flying controls, Modified from: [7].

Figure 1.1: Slingsby Firefly T67M260.

Table 1.1: Engine technical specifications (Adapted from: [8]).

Number of Engines	1
Engine Manufacturer	Textron Lycoming
Model	AEIO-540-D4A5
Compression Ratio	8.5:1
Horsepower	260

Table 1.2: Slingsby Firefly overall specifications (Adapted from: [9]).

Overall Length	7.29 m
Overall height	2.36 m
Wing Span (b)	10.60 m
Wing Area (S)	12.6 m^2
Dihedral	3° 30'
Incidence at the wing root	3°
Incidence at the Tip	0° 20'
Profile Root	NACA 23 015
Profile Tip	NACA 23 013

In the present work, the critical angle of attack, maximum lift coefficient, flow separation pattern of the boundary layer on the upper surface of the wings and vortex shedding frequency was computed with the application of CFD. Ultimately, these results were evaluated with different flight tests performed in the Slingsby Firefly.

The detailed objectives of the present thesis are the following:

• Compute the lift curve for the pre and post stall condition with the application of a steady RANS turbulence model, $k-\omega$ SST, and compare it with the lift curve obtained from steady and level flight tests;

• Identification of the maximum lift coefficient, critical angle of attack and zero lift angle with the application of CFD and evaluation of the results with data obtained from the steady and level flight test and an additional test where the critical angle of attack was obtained;

• Flow visualization of the boundary layer flow separation on the upper surface of the wing with CFD, with contours of the limiting streamlines and skin friction coefficient. Evaluate the quality of the results with a flight test where wool tufts were used as a visualisation technique while stalling the aircraft.

• Obtain the vortex shedding frequency of several probes in the wing's wake with Detached-Eddy Simulation (DES) model and comparison with the buffet frequency obtained from a stalled flight test where the frequency was recorded with accelerometers;

1.2 Thesis Outline

This thesis contains a total of six chapters. The first chapter is the introduction and motivation to the subject and the enunciation of the objectives. The second chapter is the literature review where the theory of an aircraft stall and factors that affect stall is explained. Furthermore, an introduction to turbulence and characteristic stall flow patterns are presented. In addition, an overview of CFD is done and its application is explained. Chapter three is the mathematical formulation of the mathematical models applied in this thesis, namely the steady RANS $k-\omega$ SST turbulence model and the mathematical model, DES with $k-\omega$ SST. Chapter four explains the methodology of the CFD flow calculations and flight tests performed. The meshing method and numerical settings are explained. In addition, the different flight tests are described. Chapter five presents the results of CFD and compares them with the flight test data. Chapter six presents the conclusions and future work is proposed.

Chapter 2

Literature Review

2.1 Stall of an Aircraft

2.1.1 An overview on Stall

In the very beginning of flight history, the Wright brothers would begin to suspect the cause of many of the fatalities in the attempt of flying. They found out that at low speeds the wings would start a downward movement, which if not corrected would result into a spin, ultimately resulting in an accident. In order to overcome this, they designed a control system in which a rudder and warp (now aileron) would push the wings upwards. This discovery would allow the control of stall, hence reducing stall related accidents [10]. In the subsequent years, during World War I, stall research stagnated due to the diverted funding for military purposes.

In post war times, flying had become an every day event and so were the fatalities. In fact stall was responsible for two-thirds of all the aviation accidents [10]. In 1919 researchers at National Advisory Committee for Aeronautics (NACA) were conducting stall related studies on a Curtiss ”Jenny”. At the same time at the British Royal Aircraft Establishment, the first stall control was accomplished, by designing a wing with ailerons. This was what the Wright brothers were trying to accomplish in the early flight days. The Handley Page automatic slot, shown in figure 2.1, is a representation of this mechanism, the slot remains open in a stall and closes when the aircraft is unstalled.

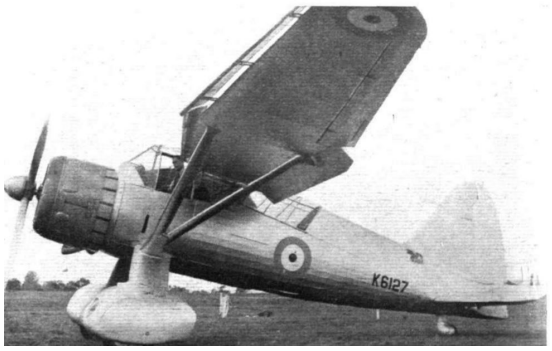

Figure 2.1: Handley Page Automatic Slot [11].

In the 1920s the Guggenheim Safe Aeroplane Competition was created and had a strict set of rules, for instance the aeroplane would have to maintain controlled, level flight at 35mph without stalling among others. This led to the development of high-lift devices including the full-span flap and slat. Ten years later F. E. Weick at Langley performed several wind-tunnel and flight test in order to design an aircraft that would have stall proof characteristics, the Ercoupe aircraft. In the UK, Melvill Jones was at that time performing several experiments on several model wings in a 28x20 inches wind-tunnel, measuring pressures and forces. It was concluded, from those experiments, that for different aerofoils thickness there were three categories of stall behaviour [10]. Namely, the trailing-edge stall and two types of leading edge stall that will be discussed in detail in section 2.2.1. Moreover, flight tests were performed in which an aircraft was equipped with wool tufts. If the aeroplane was unstalled the wool tufts would point backwards, however, if stalled the wool tufts would move in an agitated behaviour. The wool tufts behaviour for the unstalled and stalled condition, obtained from the flight tests, is shown in figure 2.2.

(a) Unstalled Aircraft

(b) Stalled Aircraft

Figure 2.2: Wool tufts flight test experiment [10].

The late 1930s were marked by great accomplishments in stall proof design of an aircraft. Increasing the wing washout and aspect ratio were some of the stall design procedures. However, World War II had began and with that a lot of the funding that was being used for stall research was now essential for military aircraft design and testing.

Post World War II there was an increase in the personal aircraft owned, which resulted in several stall and spin related accidents. In fact, it is believed that 48 percent of all fatal accidents were due to stall/spin [1]. Owing to this, NACA stall and spin scientists gathered several data regarding the spin of light aircraft [12]. In addition, from several scientists worldwide, the Tail Damping Power Factor (TDPF) was heavily studied [13], [14], [15]. The TDPF is an empirical parameter that gives an indication of the effectiveness of the vertical tail to terminate the spin. It is the product of tail-damping ratio (TDR) and unshielded rudder volume coefficient (URVC) (see equation 2.1). The terms of equation 2.1 are shown in figure 2.3. This criterion was later disproved in 1989 by NACA [16]: *"The criterion can give misleading results and should never be used."*

$$TDPF = \left[\frac{FL^2}{S(b/2)^2}\right]\left[\frac{R_1L_1 + R_2L_2}{S(b/2)}\right], \tag{2.1}$$

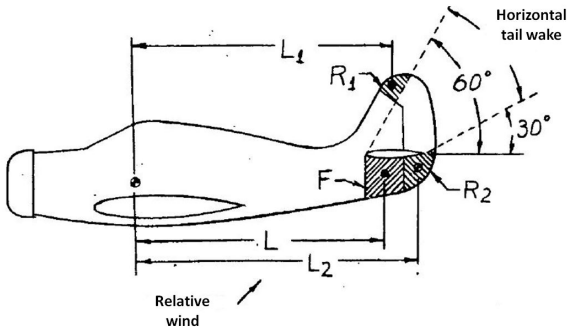

Figure 2.3: Tail Damping Power Factor geometric representation (Adapted from: [12]).

In the following decades, there were several publications and workshops on stall and spin, from those important breakthroughs were achieved, namely, in the area of *"(...) aerodynamics at high angles of attack; factors affecting the spin and spin recovery; stall and spin prevention concepts; model flight test procedures; emergency spin recovery systems; and analytical techniques"* [1].

In recent years, the publications on stall and spin seem to have diminished compared to the early days of flight research. Nevertheless, the type of stall that different thickness aerofoils possess [17] and wing stall [18] are still analysed. In addition, flight tests have been performed in several light aircraft [19], [20] to determine their stall characteristics and stall recovery procedures. Due to recent research in designing transport aircraft for low altitude and low speeds, the aircraft must be checked for its behaviour at high angle of attack. Thus, extensive stall testing needs to be performed [21]. Regarding spin research, the focus has been mainly on light aircraft spinning properties [22],[23],[24]. Moreover, spin flight-test equipment is being developed in order to fully characterize a spin [25]. In 2008, the European Aviation Safety Agency (EASA) funded a study on the concept of spin resistance light aircraft in order to increase spin design awareness to the European aeronautic industry and to verify the spin certification of aircraft [26].

Despite all the research on design and recovery from stall and spin, it still represents one of the major causes of aviation accidents of light aeroplanes. In the UK only, between 1980 and 2008, there were 359 fatal accidents of aeroplanes below 5,700 kg. In fact, 36 $\%$ of these accidents were due to stall and spin [27]. These results are shown in figure 2.4.

According to an American institution report, Aircraft Owners and Pilots Association (AOPA), accidental stalls result in more fatalities than non-stall accidents [28]. In the report, between 2010 and 2014, 2015 (both commercial and non-commercial) stall accidents were analysed and it was concluded that stall was responsible for 10 $\%$ of all non-commercial accidents with 24$\%$ of fatal accidents. *"Nearly 95 percent of them (1,901) occurred on non-commercial flights, including 911 of the 945 fatal accidents (96 percent)"*. The data discussed above is shown in figure 2.5.

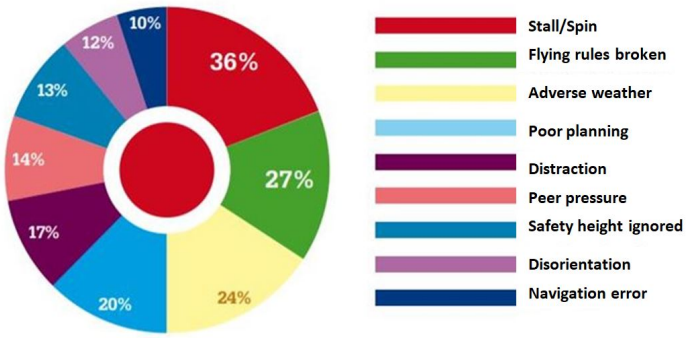

Figure 2.4: Percentage of fatal accidents in aeroplanes of 5,700 kg and less (1980 – 2008) (Adapted from: [27]) .

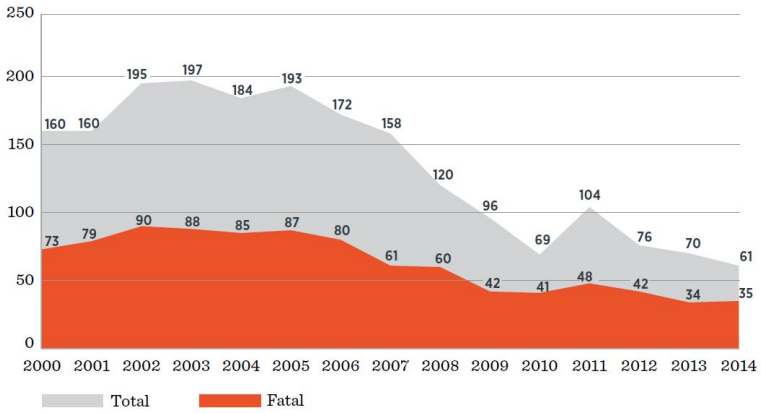

Figure 2.5: Number of stall accidents reported in the AOPA Institute report [28].

It is concluded that Stall and Spin are still potential hazards, hence continuous research needs to be performed in this area in order to prevent inadvertent spins/stalls that ultimately lead to fatalities.

2.1.2 Stall and Spin definition

A Stall occurs when the main lift device, the wing, is no longer able to produce lift in order to sustain the weight of the aircraft [29]. When an aircraft exceeds a certain angle of attack, α_{stall}, it experiences a sudden reduction in lift and a significant increase in drag, as shown in figure 2.6. This is a result of the intense adverse pressure gradients on the upper surface of the wing that leads to the separation of the boundary layer [2]. In other words at small angles of attack an increase in this angle will result in an increase of lift, however, when a certain angle, i.e., the α_{stall} is reached, increasing the angle of attack any further will no longer produce more lift.

Stalling an aircraft is often accompanied by buffet which is the vibration of the airframe due to changes in pressure caused by the shedding of vortices resultant from the wing's flow separation, it acts as a natural stall warning. This is characteristic of low speed flight at high angle of attack [29]. Moreover, the aircraft attitude changes and there is a "g-break" that the pilot detects as a reduction in g in the accelerometer [30], which often leads to a wing or nose drop. The normal acceleration and angle of attack for pre and post stall conditions are shown in figure 2.7.

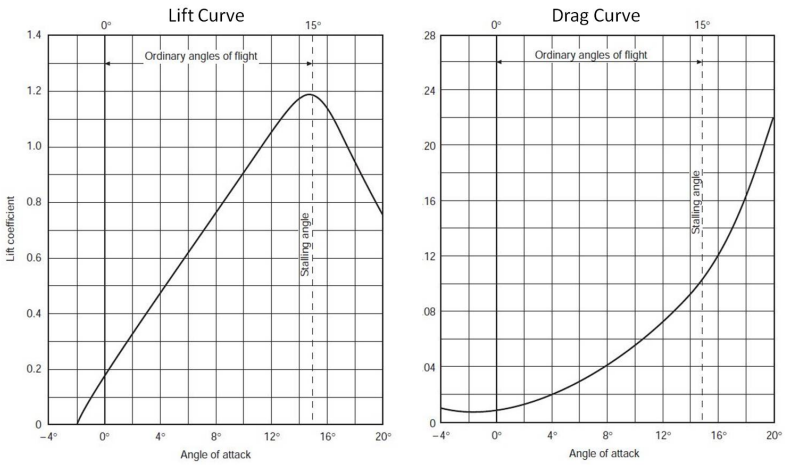

Figure 2.6: Typical lift and drag curve of an aircraft (Adapted from: [31]).

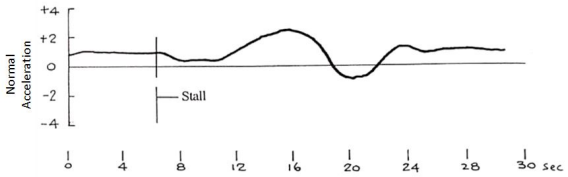

(a) Normal Acceleration (g)

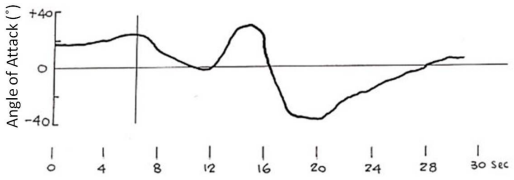

(b) Angle of attack (deg)

Figure 2.7: Aircraft stall timeline (Adapted from: [31]).

During stall, if a wing drop occurs, the aircraft stall might develop into a spin. A Spin is an intended or unintended flight manoeuvre, which differs from others, in the sense that the wings are stalled [32]. Spin is defined as an autorotating spiral motion of the aeroplane about the vertical axis (figure 2.8) that might be due to mishandling or by asymmetry in stall. Spins can be divided in two categories: erect and inverted spin. The erect spin is usually the most common type of spin and also the most difficult to recover from. An erect spin will have the yawing and rolling motions in the same direction. In the inverted spin yawing and rolling motion are in opposite directions [33].

A spin [25] is divided in three stages. The first one is the incipient stage which is the transition between straight and level to a stalled flight resulting in the auto-rotating vertical descent. The second stage is the developed stage, the radius and spin frequency are stabilised. The final stage is the recovery which is often accomplished by reducing power to idle, centralise the ailerons, apply full opposite rudder, apply forward elevator, in this order. In this study the focus is on the beginning of the incipient stage, i.e., stalled aircraft.

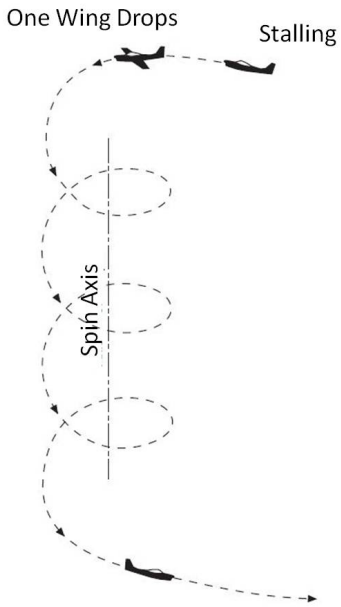

Figure 2.8: Spin Maneuver (Adapted from: [32]).

2.2 Factors that affect stall behaviour of an aircraft

The stall of aeroplane depend on several variables namely the aerofoil section, wing planform, fuselage interference, surface roughness and many more [34]. In addition a complete understanding of stall relies on the mechanism and pattern of boundary layer separation. The type of stall depends on the flow separation behaviour, i.e., if it starts from the trailing-edge or leading-edge and from the tip or root. The first are defined by the aerofoil thickness ratio and the second by the wing planform.

2.2.1 Aerofoil Section

Aerofoils at high angle of attack (AoA) are subjected to adverse pressure gradients on the upper surface of the aerofoil, which often results in the boundary layer flow separation. As mentioned in section 2.1.1, there was a need to correlate the geometric properties of the aerofoil with its stall behaviour. Hence in the early 1930's, a classification of the different types of stall was introduced. In fact, after the work of Jones [10], McCullough and Gault [34] performed further stall experiments testing defining the following stall types.

From the mentioned research three types of stall were discovered and they were dependent on the thickness of the aerofoils, those were: trailing-edge, leading-edge and thin aerofoil stall. As the AoA increases the turbulent separation point moves from the trailing-edge to the leading-edge, this is the typical flow behaviour of a trailing-edge stall. The leading-edge stall has, near the leading-edge, an abrupt separation of the flow usually with no following reattachment. The thin aerofoil stall begins with flow separation at the leading-edge with reattachment at a point that will move towards the trailing-edge [34].

Trailing-Edge Stall is a type of stall characteristic of aerofoils with thickness ratios (t/c) higher

than 12 percent of the chord length (t/c >%12). The flow begins to separate at the trailing-edge and as the AoA is increased there is a progression of the separated flow towards the leading-edge. From figure 2.9, it is observed that the C_{Lmax} is around 1.5 and after that the loss of lift is gradual, hence this being the least undesirable type of stall. The maximum lift is obtained when about 50% of the of the chord is immersed in separated flow [3].

Leading-edge stall is characteristic of aerofoils with intermediate thickness (%9 $<$ t/c $<$%12). These aerofoils still possess plenty of curvature forming a separation bubble, however, it can stay attached longer at higher AoA. When it breaks down the flow will not be able to reattach resulting in an abrupt leading-edge stall. The C_{Lmax} is higher then the latter, however, the loss of lift after the critical angle of attack is achieved, is abrupt. Due to this, leading-edge stall is the most undesirable type of stall [3].

Aerofoils with thickness ratios lower than 9% of the chord length suffer a **Thin Aerofoil Stall**. The extreme case of this type of stall is the flat plate. As seen in figure 2.9 this type of aerofoils present lower lift coefficient values when compared to the ones mentioned above. Thin aerofoils are often sharply curved behind the leading-edge, inducing a pressure gradient even at low angles of attack. Due to this, laminar separation is inevitable, the flow becomes turbulent. The flow might reattach producing a separation bubble. It can be the size of a small fraction of the chord to a chord length size. Increasing the angle of attack will increase its size, the aerofoil is stalled typically when the bubble reattaches close to the trailing-edge.

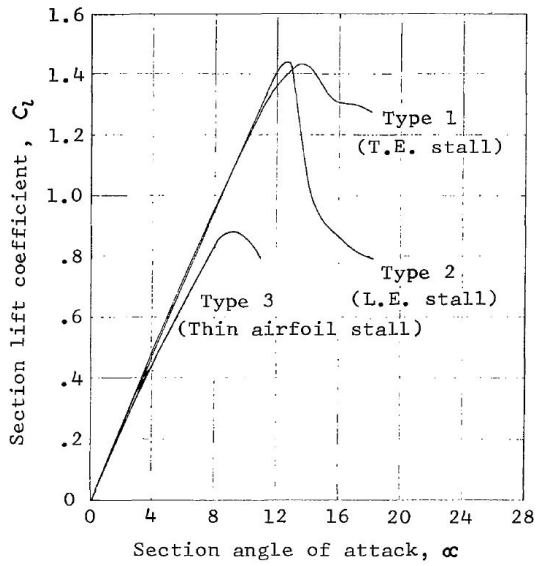

Figure 2.9: Representative lift curves for different types of stall [3].

In addition, to what was stated above, the shape of the leading-edge, aerofoil thickness to chord ratio and the Reynolds number are correlated between them. A graph is presented in the Engineering Sciences Data Unit (ESDU) report [35] that shows the correlation between the chord based Reynolds number and and upper-surface ordinate at the 1.25 per cent chord. This allow for the definition of the

type of stall of an aerofoil.

The Slingsby Firefly has a chord based Reynolds number of approximately $2.3 \cdot 10^6$ for the flight test conditions shown in section 4.2.1 and the aerofoils sections used are NACA 23013/23015 at the tip and root, respectively. Based on this specific characteristics the expected type of stall is the trailing-edge stall.

2.2.2 Wing Planform

Stalling characteristics of an aeroplane strongly depend on the wing design. Stall can also be affected by gusts and turbulent air, however, this is out of the scope of this thesis. Wing planform parameters, i.e., aspect ratio, taper ratio, sweep, twist and dihedral, define the wing design that will affect its stall behaviour.

A wings' shape will dictate where the stall will begin. According to Swatton [29], swept wings tend to stall first at the tip. Increasing the sweepback will also increase the spanwise flow of the boundary layer, the induced drag follows the same tendency. In this wing configuration the stall moves from the tip to the root owing to the separation of the boundary layer occurring at the tip first. Elliptical wings possess constant lift coefficient from tip to root, therefore the stalling angle will be the same for all the wing sections. This results in an evenly development of stall from the trailing edge to the leading-edge. Unswept and untapered wings, commonly know as rectangular wings, stall first at the wing root near the trailing-edge and moves progressively to the rest of the wing. This is a result of the lift coefficient being greater at the wing root. The schematic of the flow separation progression for different wing planform are shown in figure 2.10. The Slingsby Firefly's wings are tapered, for this wing shape stall begins at the trailing-edge and moves towards the leading-edge, at a faster rate at the wing root.

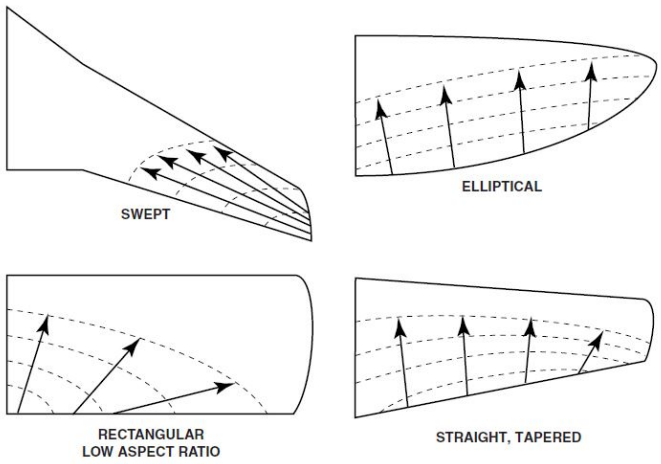

Figure 2.10: Wing planform and respective boundary layer separation [29].

The aspect ratio is defined as the ratio between the square of the wingspan and the projected wing area (equation 2.2). The lower the aspect ratio, the more the lift slope decreases with the increase of AoA and this greatly affects stall and post-stall behaviour. Low aspect ratio wings have softer stall characteristics, thus stalling at higher angles of attack. At stall, high aspect ratio wings, tend to have a

sharper lift curve than low aspect ratio wings. Although a higher maximum lift coefficient is achieved, the critical angle of attack is lower. Figure 2.11 shows how the lift depends on the aspect ratio. The CL_{max} and the slope of the curve differ for each aspect ratio. The stalling angle is higher with low aspect ratios. However, the zero lift angle remains unchanged.

$$AR = \frac{b^2}{S} \tag{2.2}$$

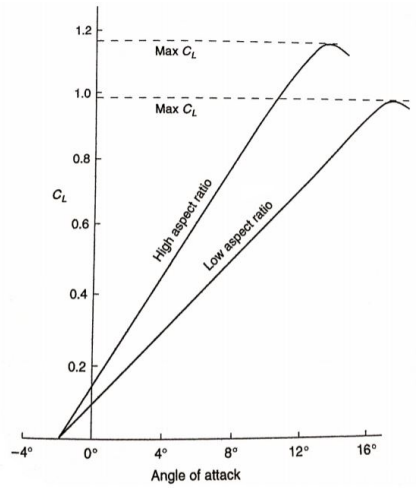

Figure 2.11: Effect of the aspect ratio on the lift curve [32].

In addition to the aspect ratio, the wing planform may be tapered from the centre of the wing to wing tip. It is also common to have different aerofoils near the tips. Tapering a wing gives several structural and aerodynamic advantages. However, there are some drawbacks. Highly tapered wings cause the lift coefficient to have a maximum near the tip, in this situation tip stall might occur. If the wing tip stalls before the rest of the wing, there might be an unexpected roll of the aircraft. In addition highly tapered wings give small chord Reynolds numbers near the tips. This will reduce the C_{Lmax} that the tips can achieve and aggravate tip stalling even further. On the other hand, untapered wings will have a centred stall which will not cause roll.

The **taper ratio** is the ratio of the tip chord (c_{tip}) to root chord (c_{root}) (equation 2.3).

$$\lambda = \frac{c_{tip}}{c_{root}} \tag{2.3}$$

Moreover, washout is often implemented in order to obtain desirable stall characteristics. This consists of twisting the tip section relative to the root section of the wing, thus reducing the lift coefficient at the tip and increasing it at the root (see figure 2.12). Ultimately, the wing will stall first at the root than at the tip, tip stalling is avoided.

The Slingsby's wing has washout, i.e., the angle of incidence at the tip is smaller than at the root. This will result in different stalling conditions along the wing, i.e., when the centre and root of the wing are stalled, the wing tip is below the stalling angle allowing for the normal function of the aileron. The

geometric characteristics of the Slingsby wing are shown in table 2.1.

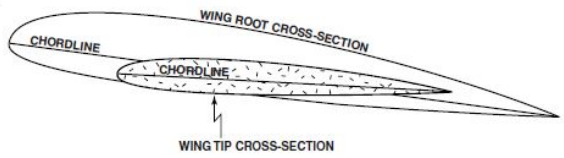

Figure 2.12: Aerofoil Washout representation [29].

Table 2.1: Wing geometric features of the Slingsby Firefly.

Aspect Ratio ($\mathcal{R}$)	9
Taper ratio (λ)	0.5
Mean Aerodynamic Chord ($\overline{c}$)	1.19 m

2.2.3 Propeller Slipstream

In the previous sections it was mostly mentioned factors of the wing design that would affect the aircraft stall. Thus, the wing is the main factor that affects stall, it will also depend on other several aircraft components. For instance the aircraft elevator travel, the wing-fuselage fairings, propeller slipstream, etc. Moreover, the external factors (atmospheric turbulence, gustiness, etc.) are always present and will also have an impact on stall. The stability and control of an aircraft are out of the scope of this thesis, however, its understanding is essential.

The propeller will have a direct impact on the results that will be later discussed and it has a very important effect on how the stall will develop. In a power-on flight the propeller accelerates the flow in the wing subjected to the slipstream (see figure 2.13), thus changing its angle of attack. Ultimately, it increases the angle of attack behind the up going blades [3], resulting in an asymmetric stall. This occurrence is usually verified for single engine aircraft, such as the Slingsby Firefly.

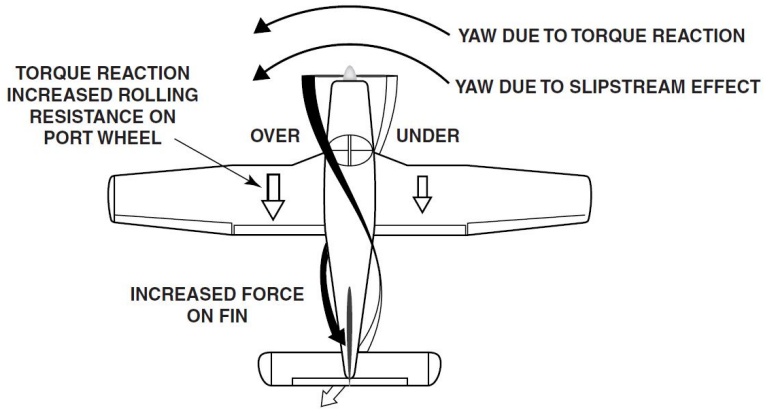

Figure 2.13: Propeller Slipstream [29].

2.3 Unsteady Flow features in stalled wings

Stall of an aircraft is accompanied by highly three-dimensional separated, unsteady and complex flow structures such as vortex shedding. The flight conditions of an aircraft are often performed at Reynolds numbers where the flow is turbulent. Hence exact modelling and understanding of the flow characteristics still remains a challenge for fluid dynamicists [36].

2.3.1 Turbulence

Turbulence represents one of the major challenges of science. Leonardo Da Vinci is believed to be one of the pioneers on the study of turbulence. In fact, he observed the difference between mean flow and the turbulent fluctuations and commented on them [37]. Some of his work is shown in figure 2.14 and according to Ugo Piomelli's translation Da Vinci stated: "Observe the motion of the surface of the water, which resembles that of hair, which has two motions, of which one is caused by the weight of the hair, the other by the direction of the curls; thus the water has eddying motions, one part of which is due to the principal current, the other to the random and reverse motion".

Figure 2.14: Leonardo da Vinci's water studies [38].

In 1932 Sir Horace Lamb gave a speech to the British Association for the Advancement of Science where according to Mullin [39] he stated: "I am an old man now, and when I die and go to heaven, there are two matters on which I hope for enlightenment. One is quantum electrodynamics and the other is the turbulent motion of fluids. About the former, I am really rather optimistic" and later Richard Feynman "Turbulence is the most important unsolved problem of classical physics" [40].

The field of turbulence experienced major breakthroughs after Osborne Reynolds (1983) experiments on pipe flow, where the definition of Reynolds number was introduced and transition from laminar to turbulent flow [41]. At low velocities the water flow in the pipe was a straight line but when the velocity was increased small eddies would appear, figure 2.15 shows data from the experiment.

Turbulence has had several definitions over the years, Hinze [42] defined turbulence as: "Turbulent fluid motion is an irregular condition of flow in which the various quantities show a random variation with time and space coordinates, so that statistically distinct average values can be discerned.". Later Bradshaw [43] added that "turbulence has a wide range of scales".

Turbulent flows are irregular in space and time, contrary to laminar flows. These flows have a time-dependent nature and are characterized by random fluctuations, hence the need of applying statistical

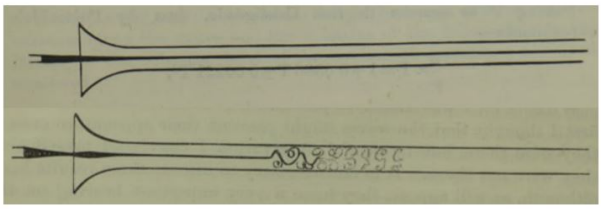

Figure 2.15: Osborne Reynolds Pipe flow experiment (Adapted from: [41]).

methods to analyse it. Associated with these flows are high Reynolds numbers, i.e., the inertial forces overcome the viscous ones. Moreover, they are characterized by having a continuous spectrum of scales, from smaller to larger scales. The larger eddies carry smaller ones, in a cascade process, the turbulence kinetic energy transfer is from larger to smaller eddies. The smaller eddies dissipate that energy into heat, thus the dissipative nature of turbulent flows. Finally, the diffusivity is enhanced, which augments the transfer of mass, momentum and energy [44].

To sum up, turbulent flows are highly complex due to their irregularity in space and time, wide range of interacting scales, highly dissipative nature and three-dimensionality [45].

2.3.2 Stall Mushroom Cells

Stalling an aircraft, as previously mentioned, generates highly separated and three-dimensional flow. In order to fully understand the flow aerodynamics several experiments were undertaken.

In 1980, Winkelmann *et al.* were investigating the effect of drooped leading edge wings at high AoA. Oil visualization of the upper surface wing flow was performed and counter-rotating swirl patterns were observed and designated as ”mushroom” shaped stall cell [46]. Both NACA 0015 2-D and 3-D wing oil flow patterns just beyond stall are shown in figure 2.16.

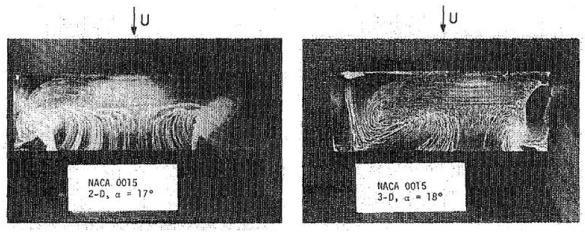

Figure 2.16: Oil flow patterns of 2-D and 3-D wing with section NACA 0015 [46].

In the following year, Winkelmann conducted a study on the formation of stall cells in a low aspect ratio rectangular wing [47]. From these experiments a model of the flow was formulated based on the flow visualization of low aspect ratio wings. This model states that the counter-rotating flow, shown in figure 2.16, is generated by the time averaged of the vortex flow that encircles from one point node to the other [48]. The model is presented in figure 2.17. When the wing is fully stalled these pattern merge and extend in the upper surface of the wings.

The mentioned studies have been performed in low aspect ratio wings. As described by Winkelmann et al. [49] when studying two rectangular wings with Clark Y-14 aerofoil with aspect ratios of 4 and

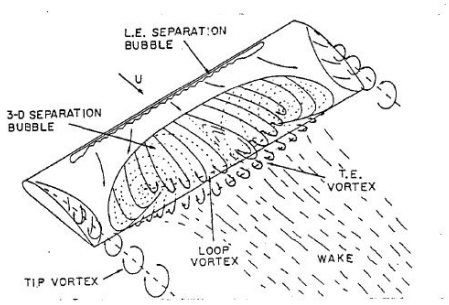

Figure 2.17: Model of the flow beyond stall on low aspect ratio wings [48].

9, the wing with the lower aspect ratio has only one stall cell whereas the high aspect ratio wing has three cells. The oil flow patter for the wing with aspect ratio of 9 is presented in figure 2.18.

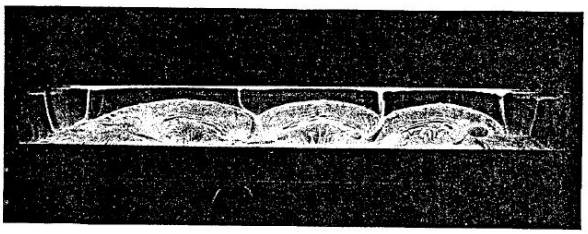

Figure 2.18: Oil flow pattern of a wing with aspect ratio of 9 [49].

Weihs and Katz described the formation of stall cells in further detail [50], a separation line is formed when the critical angle of attack is reached and it moves towards the leading edge. The location od this line is dependent on the Reynolds number, angle of attack and the aerofoil section. In the separation line there is a constant generation of vorticity due to the shear flow. The vorticity will result in vortex cores that generate the von Kármán street vortex pattern. However, this is not stable, a wavy disturbance is developed and a stall cell is formed. The process of formation of a stall cell is shown in figure 2.19.

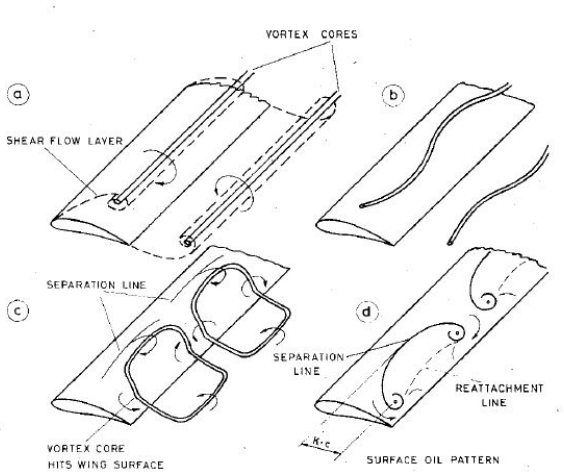

Figure 2.19: Schematic of the formation of a stall cell [50].

Moreover, they proposed that the multiple stall cells observed were a result of the Crown's [51] symmetrical mode of longitudinal waves. In fact, a mathematical expression, to determine the number of cells, was formulated as a function of the aspect ratio. The number of cells is the smallest closer integer (n): $n = AR/2.28$. According to the previous mathematical expression, for an aspect ratio of 3 one stall cell is developed, two for an aspect ratio of 6 and three for the aspect ratio of 9. Studies performed in several wings with different aspect ratio [52] show the expected outcome from what was stated above. Hence for the Slingsby Firefly wing, which has an aspect ratio of 9, three stall cells should be expected. Nevertheless, the previous mentioned studies only account for a finite wing, i.e., the interference of the fuselage is not accounted for. Ergo, some differences should be expected from the stall cells observed on the aircraft.

2.4 Computational Fluid Dynamics

2.4.1 An Overview on CFD

In the beginning of 1970s fluid dynamics was experiencing a major revolution, the introduction of CFD. In the middle of the 19th century the Euler equations for inviscid flow and Navier-Stokes equations for viscid flows were well established. However, they could not be solved owing to their system of non linear partial differential equations. The approach was to make several assumptions and simplifications about the flow dynamics, needless to say that part of its physics was not represented.

According to Toro [53], CFD is generally defined as *"The science of computing numerical solutions to partial differential or integral equations that are models for fluid flow phenomena"*.

The beginning of the CFD era is believed to have begun with the British scientist L.F. Richardson [54], he first introduced a finite difference technique for numerical solution of Laplace's equation. In fact, he created a relaxation technique for solving Laplace's equation. In 1928, which is considered the beginning of the numerical analysis era, Courant, Friedrichs and Lewy [55] were studying hyperbolic partial differential equations. They defined the Courant–Friedrichs–Lewy (CFL) stability criterion for the numerical solution of hyperbolic partial differential equations. Southwell (1940), developed a relaxation scheme which was used for both structural and fluid dynamics problems [56]. The World War II was a period of great research in this field, this was when Professor John Von Neumann evaluated the stability of numerical methods in order to solve time-marching problems. Peter Lax in 1954 created a technique to represent discontinuities in flow variables such as shocks. The contributions were mainly focused on solving one of the major challenges in fluid dynamics, the discontinuous fluid phenomena in a discrete space, commonly known as the Riemann problem [57]. In terms of viscous flow simulation Thom [58] was the first to produce a numerical solution by solving the partial differential equation for a low speed flow past a circular cylinder. At Los Alamos National Laboratory (1962), Harlow [59] proposed the method of particle-in-cell (PIC), that is a combination of Lagrangian-Eulerian description of the fluid motion [60]. Later in 1969, MacCormack developed one of the most used tools in CFD, an explicit, predictor–corrector procedure that carries his name.

During the 1950s, International Business Machines (IBM), developed the first high speed digital computers, this was the beginning of the computer era. These was a major breakthrough since it allowed the creation of computing tools essential for the numerical solutions for the governing flow equations. This was the beginning of CFD.

2.4.2 CFD in aeronautical industry

CFD revolutionized the aeronautical industry in the sense that the design of aircraft is now performed with mainly CFD and wind-tunnel testing due to the high costs associated with flight tests. Wind-tunnel testing is often unable to provide data at flight conditions, hence the application of CFD. Although CFD is capable of providing information everywhere in the flow field, it is limited by the simplifications of the mathematical model and solution algorithm [5]. The aim is not to eradicate wind-tunnel testing but to use CFD as a complementary tool.

In the early days of the application of CFD in the aeronautical industry, aeroplanes began to be designed with the aid of CFD. In the 1970s, Boeing designed the Boeing 757 and 767 with CFD, specifically the cockpit, wings and engine installations. In the following designs, Boeing 777 and Boeing 737 CFD was used extensively, figure 2.20 show the CFD impact on the design.

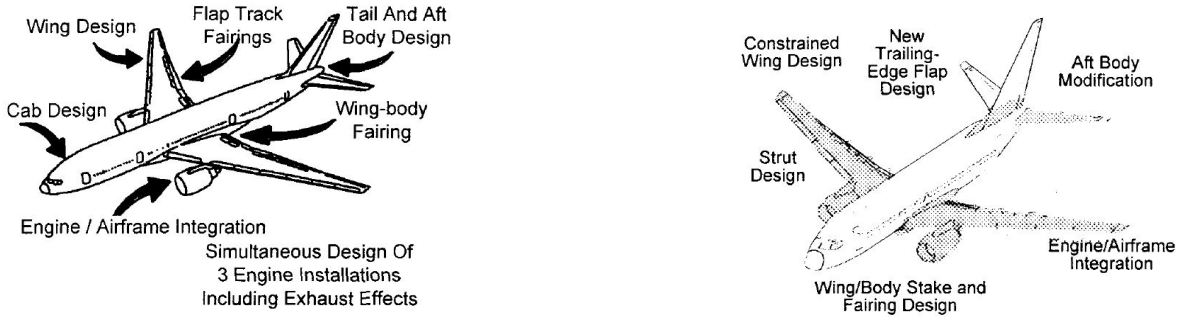

(a) Boeing 777 (b) Boeing 737

Figure 2.20: CFD contribution to aircraft design [5].

2.4.3 Mesh Generation

The mesh generation of complex geometries has been a challenge in the world of CFD. The mesh generation process is characterized according to the algorithm used, i.e., structured or unstructured mesh generation methods. Structured meshes can be pictured as a grid of points that are arranged in a regular manner throughout a cuboid. In an unstructured mesh the points are not connected with a regular topology. Structured mesh generation of complex geometries is often undesirable due to the difficulty in meshing complicated adjacent surfaces. Unfortunately this is the reality of most industries, for instance the aerospace field where several components of an aircraft are designed with complex geometries and are attached to several components. An example case is the engine and wing assembly [61]. Hence unstructured mesh generation methods have been often used and researched. An unstructured mesh compared to a structured one has the disadvantage of requiring "...a factor of 2-3 increase in

memory requirements and computer run times on a per grid point basis"[62]. Despite this, the time spent generating a mesh is reduced and the mesh adaptation is a possibility [62]. In the past few decades unstructured meshes have suffered great progress as seen in these publications [63], [64], [61], [62]. As mentioned complex geometries complicates the meshing process and in order to tackle this problem automated meshing algorithms have been developed.

Commonly used are the Octree, Delaunay and Advancing front for the generation of triangular and tetrahedral mesh. The Octree method [65] relies on involving the domain in four squares if it a 2-D problem or eight cubes if it is a 3-D one, and sub-divide them until the necessary definition is obtained. The Delaunay meshing algorithm ([66], [67]) is explained as followed: "...if a node lies inside a circle then the element that the circle is attached to should be deleted" [68]. The Advancing front method ([69], [70], [71]) guarantees that no area that lies outside the boundaries is included in the triangulated computational domain.

2.4.4 Turbulence modelling

According to Spalart, numerical prediction of turbulence is a current challenge, even for simple 3D geometries. These challenges are due to the computing cost and mesh generation [72]. In addition, it faces two main challenges: growth and separation of the boundary layer and momentum transfer after separation [72]. Turbulence requires a statistical approach due to its random fluctuations. In 1985 Reynolds introduced a procedure in which all quantities would be expressed a sum of their mean and fluctuating parts. Modelling turbulence is usually accomplished with the following mathematical models: RANS models (simple or complex), Unsteady RANS (URANS), Detached-Eddy Simulation (DES) LES and Direct Numerical Simulation (DNS). The main focus is the RANS two equation models and DES due to their application in the present work. The mathematical formulations are explained in detail in chapter 3.

DNS is a CFD mathematical model that solves numerically the Navier-Stakes equations, thus solving the whole range of spatial and temporal scales of turbulence. Hence it does not require the application of a turbulence model and it offers a high-fidelity solution [73]. However, DNS requires fine three-dimensional meshes and a large amount of time steps to obtain the time-averaged quantities.

Ergo, LES was created in order to reduce the computationally demanding simulations in DNS. "Large-eddy simulation (LES) is a technique intermediate between the direct simulation of turbulent flows and the solution of the Reynolds-averaged equations" [74]. In LES the large eddies (energy-carrying structures) are computed exactly, and only the smaller scales of turbulence are modelled.

Nevertheless, both methods are computationally demanding. According to Spalart, only around 2045 high Reynolds number calculations of a three-dimensional wing will be possible. In the following section, table 2.2 shows the computational cost of the refereed models.

According to Nichols, the application of RANS turbulence models to unsteady flows was shown to be limited and inaccurate [75] due to their overproduction of eddy viscosity and over-damping of unsteady motion of the fluid. In addition, they tend to over-predict the pressure of the vortex core. Nichols and Nelson stated that: "The problem is inherent in the construction of the turbulence models

and is caused by the assumption that all scales of the unsteady motion of the fluid are to be captured and modelled by the turbulence model" [75].

In 1997, Spalart proposed a new approach [76] named DES which is an hybrid model created to treat turbulence of separated flows at any Reynolds number and overcome the computational constraints of LES and DNS. In a simplistic explanation, it combines RANS in the boundary layer and LES in the separated regions. This approach will be explained in detail in section 3.3.

2.4.5 Cost of Turbulence Modelling

Ultimately, choosing a turbulence model relies on the accuracy of the modelled flow and the cost aspect. Spalart [72] compared the cost of several models, by the readiness date. The flow is of an airliner or a car. The different strategies for turbulence modelling are presented in table 2.2, the models compared are: URANS (2/3D URANS), RANS (3D RANS), DES, LES, Quasi-Direct Numerical Simulation (QDNS)(QDNS) and DNS. The "aim" column refers to the objective of the mesh refinement: numerical or physical. In RANS refining the mesh is a synonym of enhanced numerical accuracy and the aim is numerical accuracy. Conversely, in LES and DES finer meshes allow solving smaller sized eddies representing a more complete eddy cascade, aiming for physical accuracy, mesh spacing dependent. The Reynolds number dependence is due to the number of mesh points, weak dependence means a slow logarithmic dependence, a strong is similar to a viscous sublayer thickness. The "3/2D" column means that simulations that are 2D in geometry are 3D. The mesh spacing for RANS and DES is based on present data, for a wing according to Spalart [77], the mesh count is 10^{11}. The time step follows the same mesh information. The readiness is based on the estimate that the computer power increases by a factor of 5 every five years. Ultimately, it is believed that with massively separated flows, RANS will be discarded for both steady and unsteady. However, with hybrid methods, the more capable the RANS models are the lower the cost the hybrid calculation will be, giving an incentive to proceed with RANS technology.

Table 2.2: Strategies for turbulence modelling (Adapted from: [72]).

Name	Aim	Unsteady	Re-dependence	3/2D	Empiricism	Mesh	Steps	Ready
2D URANS	Numerical	Yes	Weak	No	Strong	10^5	$10^{3.5}$	1980
3D RANS	Numerical	Yes	Weak	No	Strong	10^7	10^3	1990
3D URANS	Numerical	Yes	Weak	No	Strong	10^7	$10^{3.5}$	1995
DES	Hybrid	Yes	Weak	Yes	Strong	10^8	10^4	2000
LES	Hybrid	Yes	Weak	Yes	Weak	$10^{11.5}$	$10^{6.7}$	2045
QDNS	Physical	Yes	Strong	Yes	Weak	10^{15}	$10^{7.3}$	2070
DNS	Numerical	Yes	Strong	Yes	None	10^{16}	$10^{7.7}$	2080

2.4.6 CFD approaches in the present work

For the purpose of this thesis, a steady RANS turbulence model and a hybrid RANS/LES model was chosen. In order to obtain the maximum lift coefficient, the critical angle of attack and the flow separation patterns on the upper surface of the wing, the steady turbulence model $k-\omega$ SST was used. The vortex shedding frequency was obtained with the hybrid RANS/LES model - Detached Eddy Simulation.

The $k-\omega$ SST [78], [79] is widely used in industry and it was created in order to deal with adverse pressure gradients and flow separation. The previous models, for instance $k-\epsilon$, failed to predict accurately the turbulent boundary layer separation. Hence this model was developed and it has been applied and studied intensively [80], [81], [82]. The mathematical formulation is presented in section 3.2.2. Ultimately, decision based on the limited computational time and accuracy of the model, the $k-\omega$ SST proved to be the most suitable RANS model.

In order to compute the vortex shedding frequency, an unsteady phenomena, URANS, DES, LES and DNS could be applied. However, as it was previously explained in section 2.4.5, LES and DNS were not feasible in terms of computational and processing time. Hence the decision was between DES and URANS. Though it could be argued that URANS could be applied in order to compute the vortex shedding frequency, URANS has been shown [83], [84], [85] to be less accurate than DES. According to Spalart (see table 2.2) the computational cost of URANS is similar DES .

Hence DES was the approach chosen to compute the vortex shedding frequency. DES was created with the intent of dealing with massively separated flows for geometries and Reynolds numbers that are not yet possible with DNS and LES. In 1997, Spalart [77] presented this approach that functions as a sub-grid model where the mesh is fine enough to activate LES and as RANS in the remaining regions. The mathematical formulation is presented in section 3.3. This model has been widely studied [86], [87], [88], [89], [90], thus giving the author confidence of its application.

The RANS turbulence model chosen for DES was the $k-\omega$ SST. The reason for this was based on the work developed by Spalart et al. [91] and Strelets [86]. They purposed this mathematical model in order to overcome the limitations of the Spalart-Allmaras model to predict separation. The aim was to apply one of the best two-equation RANS models, $k-\omega$ SST, to predict the separation of the boundary layer.

Chapter 3

Mathematical Model

In this section the mathematical models applied in the present thesis are presented, i.e., the RANS two-equation turbulence model $k-\omega$ SST and mathematical approach DES $k-\omega$ SST.

3.1 Navier-Stokes Equations

The motion of a viscous fluid is described by Navier-Stokes equations (NSE). Assuming a compressible, steady flow, the NSE in the conservation form are:

$$\frac{\partial}{\partial x_i}\left(\rho u_i\right) = 0 \tag{3.1}$$

$$\frac{\partial}{\partial x_j}(\rho u_j u_i) = -\frac{\partial p}{\partial x_i} + \frac{\partial \tau_{ij}}{\partial x_j} \tag{3.2}$$

$$\frac{\partial}{\partial x_j}\left[\rho u_j\left(h + \frac{1}{2}u_i u_i\right)\right] = \frac{\partial}{\partial x_j}(u_j \tau_{ij}) - \frac{\partial q_j}{\partial x_j} \tag{3.3}$$

where $h = e + p/\rho$ is the specific enthalpy, τ_{ij} is the viscous stress tensor and q_j is the heat flux vector. For gases, the ideal gas law is:

$$p = \rho RT = (1-\gamma)\rho e \tag{3.4}$$

The viscous stress tensor is given by:

$$\tau_{ij} = 2\mu\left(s_{ij} - \frac{1}{3}\frac{\partial u_k}{\partial x_k}\delta_{ij}\right), \tag{3.5}$$

where s_{ij} is the strain-rate tensor and is formulated as:

$$s_{ij} = \frac{1}{2}\left(\frac{\partial u_i}{\partial x_j} + \frac{\partial u_j}{\partial x_i}\right), \tag{3.6}$$

The convective heat flux q_j is defined as

$$q_j = -\kappa \frac{\partial T}{\partial x_j} \tag{3.7}$$

where κ is the thermal conductivity. Moreover, the specific internal energy, e, and specific enthalpy h are given by:

$$e = c_v T \tag{3.8}$$

$$h = c_p T \tag{3.9}$$

where c_v and c_p are the specific-heat coefficients ($\gamma = c_p/c_v$ and $R = c_p - c_v$). Thus the heat flux is defined as:

$$q_j = -\kappa/c_p \frac{\partial h}{\partial x_j} = -\frac{\mu}{Pr}\frac{\partial h}{\partial x_j} \tag{3.10}$$

where Pr is the Prandtl number and is defined as:

$$Pr = \frac{c_p \mu}{\kappa} \tag{3.11}$$

Assuming a density weighted time (Favre) average, where any dependent variable $\Phi(x,t)$ is decomposed as $\Phi = \tilde{\Phi} + \Phi$", the Favre averaged NSE are defined as follows:

$$\frac{\partial}{\partial x_i}\left(\overline{\rho}\tilde{u_i}\right) = 0 \tag{3.12}$$

$$\frac{\partial}{\partial x_j}(\overline{\rho}\tilde{u_i}\tilde{u_j}) = -\frac{\partial \overline{p}}{\partial x_i} + \frac{\overline{\tau_{ij}}}{\partial x_j} - \frac{\partial}{\partial x_j}(\overline{\rho u_i'' u_j''}) \tag{3.13}$$

$$\frac{\partial}{\partial x_j}\left[\overline{\rho}\tilde{u_j}\left(\tilde{h} + \frac{1}{2}\tilde{u_i}\tilde{u_i}\right) + \tilde{u_j}\frac{\overline{\rho u_i'' u_i''}}{2}\right] = \frac{\partial}{\partial x_j}\left[\tilde{u_i}(\overline{\tau_{ij}} - \overline{\rho u_i'' u_j''}) - \overline{q} - \overline{\rho u_j'' h''} + \overline{\tau_{ij} u_i''} - \overline{\rho u_j'' \frac{1}{2} u_i'' u_i''}\right] \tag{3.14}$$

$$\overline{p} = (\gamma - 1)\overline{\rho}\tilde{e} \tag{3.15}$$

The Reynolds Stresses are:

$$\overline{\rho}\tau_{ij} = \overline{-\rho u_i'' u_j''} = 2\mu_t\left(s_{ij} - \frac{1}{3}\frac{\partial \tilde{u_k}}{\partial x_k}\delta_{ij}\right) - \frac{2}{3}\overline{\rho}k\delta_{ij} \tag{3.16}$$

3.2 Turbulence Models

Due to the nonlinearity of the Navier-Stokes equations, the Reynolds stresses appear as unknowns. Hence, a turbulence model is required in order to model the stresses. The Reynolds stresses can be determined either via eddy-viscosity hypothesis or more directly from modelled Reynolds-stress transport equations [92]. In this chapter only the eddy viscosity models will be discussed.

The following mathematical formulations will be presented in their original presented form, for an incompressible flow. A Favre averaged ought to be performed in order to apply the mathematical models to a compressible flow.

3.2.1 Eddy Viscosity Models

In 1877, Boussinesq [93] introduced the concept of Eddy Viscosity, he postulated that the momentum transfer caused by turbulent eddies can be modelled with a eddy viscosity. According to his hypothesis, the Reynolds Stresses are given by:

$$\rho\tau_{ij} = 2\mu_t s_{ij} - \frac{2}{3}\rho k\delta_{ij} \tag{3.17}$$

In equation 3.17 the term s_{ij} is the strain rate tensor (eq. 3.18), δ_{ij} is the Kronecker delta, k the Turbulence Kinetic Energy and μ_t the eddy viscosity.

$$s_{ij} = \frac{1}{2}\left(\frac{\partial u_i}{\partial x_j} + \frac{\partial u_j}{\partial x_i}\right) \tag{3.18}$$

The Boussinesq assumption is used by algebraic models, one-equation models and two equation models.

3.2.2 Two-Equation Models

Two equation models solve two separate equations, the turbulent velocity and length scales that are required to define the eddy-viscosity for both a turbulent and a time scale. The most common and used in industry are the $k-\varepsilon$ and the $k-\omega$ models. The first transported variable is k, the turbulence kinetic energy. The second variable depends on the chosen model: the turbulent dissipation, ε, for the $k-\varepsilon$ model and the specific dissipation rate, ω. This variables determine the scale of turbulence and k determines the velocity scale.

The two-equation RANS model used in this thesis is the $k-\omega$ SST, hence this section is focused on its mathematical formulation. The turbulence model $k-\omega$ SST differs from the remaining $k-\omega$ models in the sense that accounts for the transport of the turbulence shear stress in the definition of the eddy viscosity [94]. The following formulation is presented for an incompressible flow as it was formulated by Menter [78], hence for a compressible flow the Favre averaging should be applied.

The turbulence kinetic energy, k, and the specific dissipation rate, ω, are respectively defined as follows:

$$\tau_{ij}\frac{\partial u_i}{\partial x_j} - \beta^*\rho\omega k + \frac{\partial}{\partial x_j}\left[(\mu + \sigma_k\mu_t)\frac{\partial k}{\partial x_j}\right] = 0 \tag{3.19}$$

$$\frac{\gamma}{\nu_t}\tau_{ij}\frac{\partial u_i}{\partial x_j} - \beta\rho\omega^2 + \frac{\partial}{\partial x_j}\left[(\mu + \sigma_\omega\mu_t)\frac{\partial \omega}{\partial x_j}\right] + 2\rho(1-F_1)\sigma_{\omega 2}\frac{1}{\omega}\frac{\partial k}{\partial x_j}\frac{\partial \omega}{\partial x_j} = 0, \tag{3.20}$$

The constants ϕ of the model are calculated from the constants, ϕ_1, ϕ_2 as follows:

$$\phi = F_1\phi_1 + (1-F_1)\phi_2 \tag{3.21}$$

The function F_1 is defined as:

$$F_1 = tanh(arg_1^4) \tag{3.22}$$

$$arg_1 = min(max(\frac{\sqrt{k}}{0.09\omega y}; \frac{500\nu}{y^2\omega}); \frac{4\rho\sigma_{\omega 2}k}{CD_{k\omega y^2}}) \tag{3.23}$$

$$CD_{k\omega} = max(2\rho\sigma_{\omega 2}\frac{1}{\omega}\frac{\partial k}{\partial x_j}\frac{\partial \omega}{\partial x_j}, 10^{-20}) \tag{3.24}$$

where y is the distance to the next surface and $CD_{k\omega}$ is the cross-diffusion term.

In this model the eddy viscosity is defined as follows:

$$\nu_t = \frac{a_1\kappa}{max(a_1\omega; \Omega F_2)} \tag{3.25}$$

where Ω is the strain rate, and F_2 define as:

$$F_2 = tanh(arg_2^2), \tag{3.26}$$

$$arg_2 = max\left(2\frac{\sqrt{\kappa}}{0.09\omega y}; \frac{500\nu}{y^2\omega}\right), \tag{3.27}$$

The constants of $k-\omega$ SST model for the set 1 and 2 are shown in tables 3.1 and 3.2, respectively.

Table 3.1: Set 1 $k-\omega$ SST Model Constants [78].

σ_{k1}	$\sigma_{\omega 1}$	β_1	a_1	β^*	κ	γ_1
0.85	0.5	0.0750	0.31	0.09	0.41	$\beta_1/\beta^* - \sigma_{\omega 1}\kappa^2/\sqrt{\beta^*}$

Table 3.2: Set 2 $k-\omega$ SST Model Constants [78].

σ_{k2}	$\sigma_{\omega 2}$	β_2	β^*	κ	γ_2
1.0	0.856	0.0828	0.09	0.41	$\beta_2/\beta^* - \sigma_{\omega 2}\kappa^2/\sqrt{\beta^*}$

3.3 Detached Eddy Simulation (DES)

The approach DES was first introduced by Spalart et al. [77] and it has been improved in the past decades [95], [96], [97], [98] . DES is commonly referred as hybrid LES/RANS models, using LES for the largest eddies and RANS for boundary layers. It has been designed to target High-Reynolds number wall bounded flows, where applying LES would be too costly. The RANS part of the computation may have different turbulence models: Spalart-Allmaras, realisable $k-\varepsilon$, $k-\omega$ BSL or SST, etc.

The DES $k-\omega$ SST model was applied in the present work. This model was formulated as a modification to the length scale which is involved in the RANS turbulence model. The length scale of the RANS turbulence model $k-\omega$ SST in terms of k and ω is the following:

$$l_{k-\omega} = k^{1/2}/(\beta^*\omega) \tag{3.28}$$

The challenge found was to choose which specific terms of the model this length scale should be replaced by the DES length scale

$$\tilde{l} = min(l_{k-\omega}, C_{DES}\Delta) \tag{3.29}$$

The only restriction was that the the eddy viscosity would be proportional to the magnitude of the local strain rate and to the square of the grid spacing, following the Smagorinski LES model. Following this line of thought, the only term modified was dissipative term of the k- transport equation (see equation 3.19):

$$D^k_{RANS} = \rho\beta^* k\omega = \rho k^{3/2}/l_{k-\omega} \tag{3.30}$$

The only modification is the length scale, $\tilde{l}$ substitutes $l_{k-\omega}$

$$D^k_{DES} = \rho k^{3/2}/\tilde{l} \tag{3.31}$$

This formulation has two branches, $k-\omega$ and $k-\omega$, similarly to the $k-\omega$ SST RANS model. Hence, the C_{DES} constants ought to be calibrated for the two branches and blended with the values obtained from the $k-\omega$ SST RANS model.

$$C_{DES} = (1-F_1)C^{k-\epsilon}_{DES} + F_1 C^{k-\omega}_{DES} \tag{3.32}$$

where F_1 is computed with the $k-\omega$ SST RANS model blending function (equation 3.22).

DES Mesh

Spalart's DES guide [76] mentions different regions and Super-regions which one should be careful when preparing the mesh. The regions shown in figure 3.1 do not have separate equations but different grid spacing.

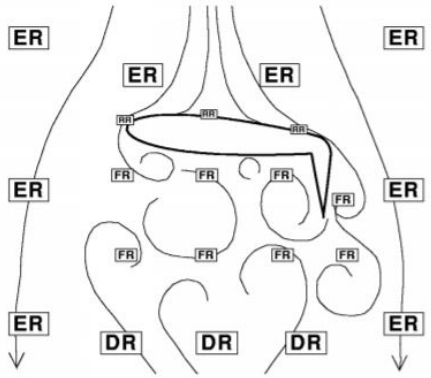

Figure 3.1: Different flow regions of DES [76].

The **Euler Region (ER)** extends to infinity and covers most of the volume. This region is never entered by turbulence or vorticity, except in the generation of shocks. The grid should have isotropic spacing in the three directions [76].

RANS Region (RR) represents the boundary layer and initial separation. The mesh should not be too fine in order not activate LES in this region, since in this region it is assumed pure-RANS calculations. It is decomposed into the viscous region (VR) and RANS Outer Region (OR).

The VR, in the wall-normal direction, the standard viscous sublayer, buffer layer and log layer are created. The time-dependence is weak and it is not significant. The RANS model dictates the first spacing. Applying the Spalart-Allmaras model, it is advised to use a $\Delta y^+ = 2$ or less. In addition, the stretching ratio, $\Delta y_{j+1}/\Delta y_j$, should be around 1.25 or less. The boundary layer in the OR region is modelled with turbulence, without activating the LES equations. Normal to the wall, the grid, is treated as in the RANS region. It is advised to overestimate the boundary layer thickness then to underestimate it.

LES regions (LR) region contains turbulence and vorticity, but no boundary layers are present. This region is divided into the Viscous Region (VR), the Focus Region (FR) and the Departure Region (DR). In the VR the grid requirements are the same as the RANS region. The VR applies requires the same mesh procedure as the RANS region. LES is activated in the Focus region, separated flow must be resolved and a grid spacing Δ_0 needs to be set. The grid spacing determines the spatial resolution in DES. In the departure region the grid resolution may exceed Δ_0, it will return to a quasi-steady RANS. The DR no longer requires the same grid refinement as the FR. However, the transition between these two regions must be done carefully.

The final regions are the grey regions, which are the zones between all the regions mentioned above, i.e., the boundaries between regions. Grey areas raised complaints as soon as 2000 when DES was applied to an expanded nozzle flow calculation. Moreover, users quickly encountered grid spacings that disturbed the RANS model. This motivated a relatively deep change in its formulation with shielded DES and delayed DES as the DES length-scale limiter now depends on the solution, rather than on the grid only [83].

Chapter 4

Methodology

4.1 Computational Fluid Dynamics of the Slingsby Firefly

The following sections will outline the 3D CFD half model of the Slingsby Firefly meshing and flow calculations procedure. The model was meshed with the ANSYS ICEM CFD software and the flow filed calculations were performed with the solver ANSYS Fluent.

4.1.1 Geometry preparation for the meshing process

1. Slingsby CAD Model

A Slingsby Firefly computer-aided design (CAD) was given by Cranfield University in a IGES format. The CAD model represented accurately the Slingsby Firefly aircraft. The model had sliver surfaces and intersecting geometry and in order to have a good meshing process a cleaner geometry was required. Hence, the model was improved with the aid of the Space Claim ANSYS Software. The model given and the improved one are shown in figure 4.1. Only half of the model was mesh due computational resources available.

The propeller was removed from the model since its effect on the flow was not to be analysed, however this will have an impact on the solutions that will be discussed in section 5.2.1. The control surfaces remained due to their relevance to the stalling of the aircraft. In addition, the undercarriage remained in order to have a more accurate representation of the aircraft. The CAD model dimensions are marginally different to the aircraft dimensions, see table 4.1.

The model was then imported to the meshing software ICEM CFD. Prior to the meshing phase the model requires checking. The *Clean Topology* tool allows the user to understand if the geometry is represented correctly, i.e., if there are no curves unattached to a surface. It uses a colour scheme to represent the curves that are attached to surfaces. Red curves are attached to two surfaces, yellow curves are only attached to one surface and have a gap between them, blue are attached to more than three surfaces and green ones unattached curves. The *Clean Topology* tool, according to a given tolerance, eliminates unwanted curves and holes in the geometry.

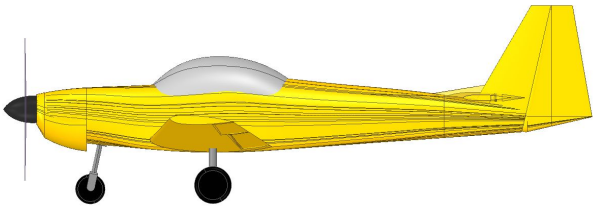

(a) Slingsby Firefly initial model.

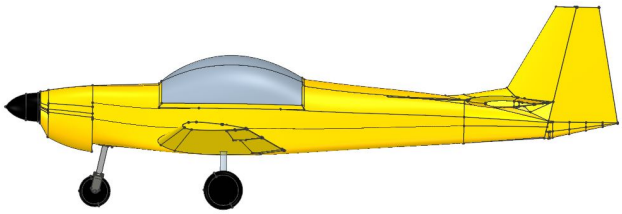

(b) Slingsby Firefly improved model.

Figure 4.1: Initial and Improved model of the Slingsby Firefly.

Table 4.1: CAD model and Slingsby Firefly dimensions (Adapted from: [99]).

Dimensions	Slingsby Firefly	CAD Model
Overall Length	7.29 m	7.37 m
Overall height	2.36 m	2.46
Wing Span	10.60 m	10.6 m
Wing Area	12.6 m^2	12.43 m^2
Dihedral	3° 30’	-
Incidence at the wing root	3°	-
Incidence at the Tip	0° 20’	-
Profile Root	NACA 23 015	-
Profile Tip	NACA 23 013	-

A tolerance of 0.001 m was used in order to close unjointed surfaces and to maintain the overall features of the model. The aim is to have the geometry with only red and blue curves, this was accomplished with the Slingsby Firefly model and is presented in figure 4.2.

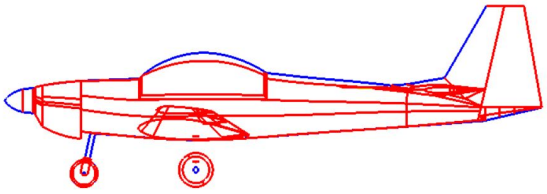

Figure 4.2: Topology of the Slingsby Firefly CAD model.

2. Geometry division into parts

The model was divided in different parts, as shown in figure 4.3, with the ANSYS ICEM CFD meshing software. Performing CFD in a complex geometry is a challenge on its own and for this project

the correct division of the model into parts would facilitate the meshing process. This enabled for different mesh sizes on the model and for local refinement, feature particularly important when the focus of the mesh is only on one part and not on the entire geometry.

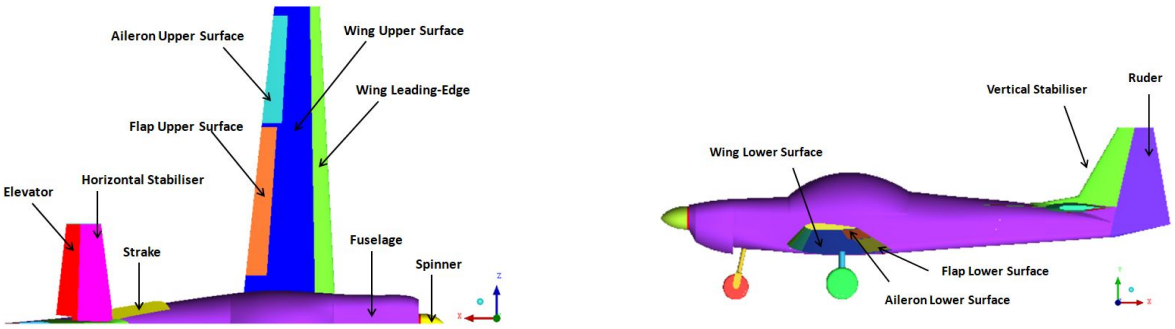

(a) Top view. (b) Lateral view.

Figure 4.3: Geometry division in different parts.

3. Computational Domain

The computational domain adopted for the flow calculations was a semi-cylinder described in a Cartesian coordinate system (x, y, z). This decision was based on several publications [100], [101], [102], [103], where CFD of an aircraft was performed. They opted for a fluid computational domain with the same shape. Moreover, this computational domain reduces the number of mesh elements when compared to another commonly used shape, the parallelepiped.

Due to the boundaries conditions applied (see section 4.1.3), there is a requirement that the domain ought be large enough so that the boundaries conditions can be met. Hence, it is advised that the domain size is typically 10 times the largest characteristic length of the body being studied [104]. The largest characteristic length is the fuselage length (L). The domain possesses an inlet, outlet, far field and symmetry plane. Thus, the inlet distances 10L from the aircraft, the outlet 15L and the radius of the cylinder is 5L. These dimensions are similar to the ones used in previous studies [101], [100], [102], [105], [104], [103]. The applied fluid computational domain schematic is shown in figure 4.4.

Both steady and unsteady simulations use the same domain dimensions and positioning of the model.

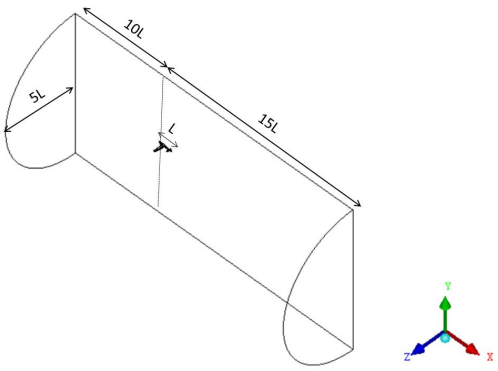

Figure 4.4: Isometric view of the computational fluid domain.

4.1.2 Meshing Process

The following mesh process was applied for the meshes used for both RANS and DES simulations.

The mesh was generated first with a top-down approach Octree method [65] which means that it does not need any initial surface mesh and use the volume meshing distribution to impose a surface mesh onto the geometry and boundaries. Due to the viscous nature of the flow, prism layers were then computed in order to represent the boundary layer. The final mesh was computed with the Delaunay method [66], [67], a bottom-up approach which requires an initial surface mesh. The surface mesh is composed of triangles, the boundary layer with prisms and the volume mesh with tetrahedra (see figure 4.5).

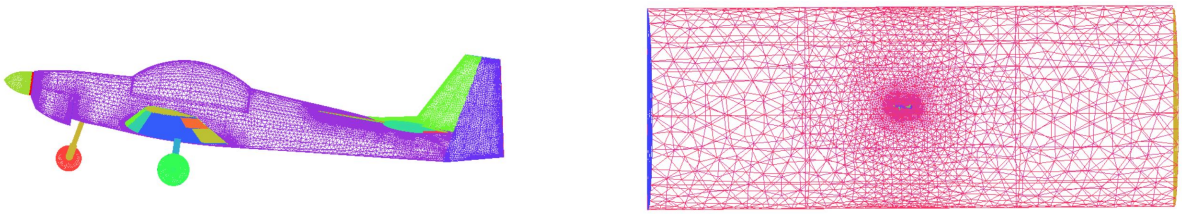

(a) Slingsby Firefly surface mesh.

(b) Complete model surface mesh.

Figure 4.5: CFD model mesh.

An unstructured mesh allows for a rapid local mesh refinement exercise for both RANS and DES flow calculations. This type of mesh provides a rapid generation of a mesh for complex geometries and also allows for the generation of a density region, essential for the DES flow calculations. According to Spalart [76], there are several mesh regions with different densities in order to be able to apply DES. In this particular work, the region of interest is the wing's wake where the vortex shedding is computed. This is the focus region where nearly isotropic cells are required in order to in to resolve unsteady and time-dependent features [106]. Hence, a density region with near isotropic cells is generated, with a grid spacing (Δ) of 0.03 m, which is approximately 2.5$\%$ of the mean aerodynamic chord, shown in figure 4.6. The criteria used in order to choose the grid spacing of the focus region was a previous DES study developed by Bauer [99]. A grid spacing bigger than 0.025 $\bar{c}$ had failed to predict any LES content in his work, hence the author chose the grid spacing that had previously worked.

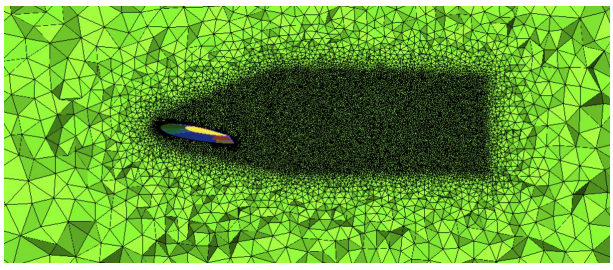

Figure 4.6: DES focus region of the mesh.

In order to be able to model the boundary layer in the mesh, prism layers were created. The thickness of the boundary layer was computed assuming a turbulent boundary layer in a flat plate. The

author is aware that up to 25% of the mean aerodynamic chord the flow is laminar, and that after that there is transition and the flow becomes turbulent. However, since all of the CFD results will be compared with flight tests where the flow is mainly turbulent, there was a decision of considering a fully turbulent boundary layer.

$$\delta \approx \frac{0.37x}{Re^{\frac{1}{5}}}\,. \tag{4.1}$$

The Reynolds number is based on the mean aerodynamic chord ($\bar{c}$), and is computed as:

$$Re = \frac{\rho V \bar{c}}{\mu}\,. \tag{4.2}$$

where ρ is the density, V is the velocity and μ the dynamic viscosity.

The simulations were performed with a flow speed of 31.9 m/s, which is 62 knots the stall speed of the aircraft for a cruise configuration, i.e., the flaps and bank angle are at 0°, this is shown in table 4.2. The density and dynamic viscosity have the values shown in section 4.2 in table 4.7.

Table 4.2: Stall speeds (knots) for different flight configurations (Adapted from: [8]).

Angle of bank	0°	30°	45°	60°
0°	62	67	74	88
18°	58	63	69	82
40°	54	58	65	77

The Reynolds number is $2.3 \cdot 10^6$, hence the assumption of a turbulent boundary layer. The boundary layer thickness (δ) is computed with equation 4.1 and it has a value of 0.024 m.

Prism layers were generated in order to accurately represent the boundary layer, see figure 4.7. A initial height and total height were set so that the three regions of the turbulent boundary layer, viscous layer, buffer layer and log-law region were modelled [103]. The various layer of a turbulent boundary layer are shown in figure 4.8.

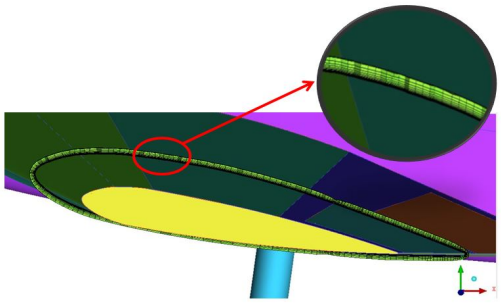

Figure 4.7: Mesh boundary layer representation with prisms.

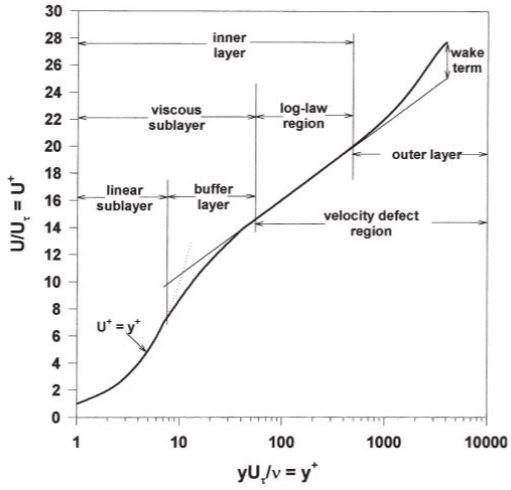

Figure 4.8: Normalized mean velocity profile in a turbulent boundary layer in semi-log coordinates [107].

Hence, a dimensionless wall distance of $y^+ < 1$ and a total height that represented 20 % ($\delta^+ = 0.2$) of the boundary layer were imposed in the prisms generation. The reasoning for choosing to represent the 20% of the boundary layer was based on the profile of the turbulent boundary layer by Brederode [2], that states that after this value the outer layer is present.

In the meshing software ICEM CFD, the desired y^+ is obtained by defining the first cell height (Δ_{y_1}) and number of prism layers (N) that ultimately will define the total height ($y_{(\delta^+=0.2)}$). The first cell height is obtained using the following expression:

$$y^+ = \frac{\rho U_\tau y}{\mu}\,. \tag{4.3}$$

The fluid properties are known (see table 4.7) and the respective Reynolds number is $2.3 \cdot 10^6$. Obtaining the friction velocity (U_τ) is accomplished by computing the skin friction coefficient (C_f), followed by the wall shear stress (τ_w) and finally calculating the friction velocity. This process is accomplished with equations 4.4, 4.5 and 4.6 in the commercial meshing software ICEM CFD. These calculations were done assuming a case of a turbulent boundary layer in a flat plane.

$$C_f = 0.058 \cdot Re_l^{-0.2}\,. \tag{4.4}$$

$$\tau_w = \frac{1}{2} \cdot C_f \cdot \rho \cdot U_\infty^2\,. \tag{4.5}$$

$$U_\tau = \sqrt{\frac{\tau_w}{\rho}}\,. \tag{4.6}$$

Ergo, the number of prism layers (N) was 22 with a geometric growth factor of 1.2, with first cell height of $9 \cdot 10^{-6}$ and a total height of 0.0047 m. The geometric growth factor was based on several publications [103],[102],[108]. After applying all these parameters and computing the prism layer, a contour of the dimensionless wall distance on the upper surface of the wing was obtained and it is shown

in figure 4.9. It is observed the the mean y^+ is below 1 as required. The summary of the boundary layer parameters computed are shown in table 4.3.

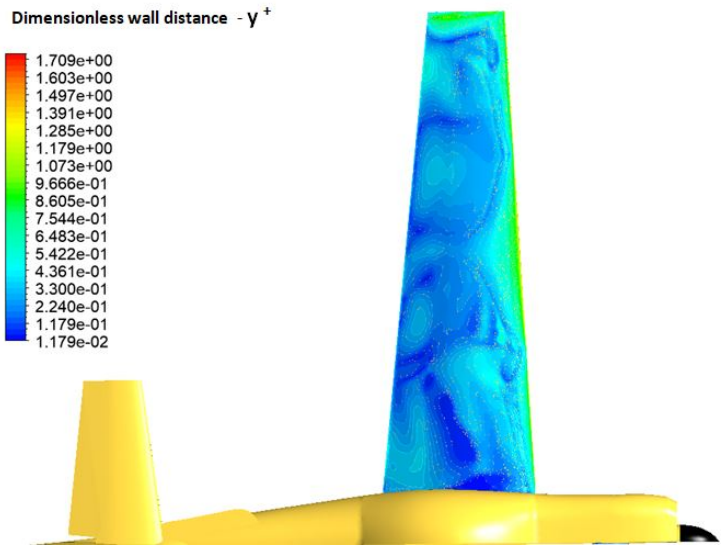

Figure 4.9: Dimensionless wall distance contour.

Table 4.3: Mesh boundary layer parameters.

Re	δ	$\delta^+ = 0.2$	C_f	τ_w	u_τ	Δ_{y_1}	N
$2.3 \cdot 10^6$	0.024	0.0047	0.0031	1.664	1.256	$9 \cdot 10^{-6}$	22

The octree mesh size is dictated by the smallest seed size. The smallest size in the model is 0.003906 m, and the octree method will multiply that value by a power of two. Hence, the maximum size of the mesh for each part was chosen according to the referred criteria. The surface and volume meshes were smoothed using the smoothing function of ICEM CFD.

Three different mesh densities were initially created: a coarse, medium and fine mesh. Due to time restrictions in order to obtain the numerical solution of the different angles of attack, a mesh sensitivity analysis was performed and it will be later discussed in section 5.1. This was performed in order to choose the most suitable mesh according to all the constraints involved. The mesh density and quality are shown in table 4.4.

Table 4.4: Mesh parameters of the three mesh densities.

Parameter	Coarse	Medium	Fine
Density (in million cells)	7.57	11.3	17.15
Mean Quality	0.825	0.8596	0.8597
Max Quality	1	1	1
Min Quality	4.674e-05	4.287e-05	8.328e-05

4.1.3 Numerical Solving

The chosen commercial software was the ANSYS Fluent for the numerical calculation performed in the present work, due to his code verification throughout the years and for being widely used in industry [109], [110]. It provides the capability of modelling compressible and incompressible, viscid or inviscid, laminar or turbulent, steady or transient fluid flows. Regarding this work, turbulent and viscous flows are of interest and for that purpose one can model the flow with: RANS models, DES or LES. The RANS models available are the one equation model Spalart-Allmaras, two equation models $k-\epsilon$, $k-\omega$, Transition $k-kl-\omega$ and Transition SST.

Numerical settings and boundary conditions

The meshes generated in ANSYS ICEM CFD were imported to the commercial solver ANSYS FLUENT, which is an industry standard CFD solver. The double precision was chosen in order to minimise the round-off error, which are the aftermath of the computer's finite precision [111]. The mesh was then imported and checking was performed in order to evaluate the quality and topology of the mesh.

The turbulence model chosen for the steady calculations was the two-equation model $k-\omega$ SST due to its better performance when dealing with separated flows. This is explained in further detail in section 2.4.6. The unsteady calculations were performed with DES $k-\omega$ SST.

The solver can be chosen between the pressure-based and density-based solver. In the pressure-based solver the velocity field is achieved by solving a pressure equation. The pressure equation is formulated from the continuity and the momentum equations, so that the velocity field, corrected by the pressure, satisfies the continuity. The density-based solver solves the governing equations of continuity, momentum, energy and species transport simultaneously. Both numerical methods use finite-volume approach.

In in the first versions of the ANSYS Fluent software the criteria to choose between the two solvers was flow compressibility, i.e., the pressure-based solver for incompressible flows and the density-solver for compressible flows. The case is different in recent versions: "However, recently both methods have been extended and reformulated to solve and operate for a wide range of flow conditions beyond their traditional or original intent" [94]. Both methods solve the governing integral equations for the conservation of mass and momentum, and (when appropriate) for energy and other scalars such as turbulence and chemical species [94]. This is accomplished with the application of pre-conditioning techniques that allow for the density-based solver to work in a wide-range of flow conditions, namely low Mach number and incompressible flows [112], [113], [114]. In fact, ANSYS Fluent 18.2 applies the preconditioning: "Time-derivative preconditioning modifies the time-derivative (...) by premultiplying it with a preconditioning matrix. This has the effect of re-scaling the acoustic speed (eigenvalue) of the system of equations being solved in order to alleviate the numerical stiffness encountered in low Mach numbers and incompressible flow" [94]. Moreover, in a Cranfield University CFD guide, it is advised to use the density-based solver due to perform the flow calculations with greatest stability and speed for

the High-performance computing (HPC) cluster used [104].

A first approach was to apply the pressure-based solver, however this attempt was not successful and the solution diverged after a few iterations. The author followed the guidelines of the ANSYS Fluent Users Guide in order to solve the convergence problem. It is advised to: "A safe approach is to start your calculation using conservative (small) under-relaxation parameters (...)" [115]. Although under relaxation values of 0.2 and 0.3 were applied, the solution continued to diverge. Due to time limitations, the author was not able to understand the reason for the divergence of the solution. Since the density-based solver had been previously applied successfully for similar applications [102], [103], [101], [100], [105], this was the solver applied.

After this, the reference values, which are used to calculate the lift and drag coefficients, etc. were set. The reference values are the following: area of the main lift device (in this work is the area of one wing), the density for the test conditions (flight test altitude is 5000 ft $\approx$ 1524 m), the length which is the mean aerodynamic chord of the wing, the ambient pressure and temperature of the test conditions, viscosity and ratio of specific heats. The reference values are shown in table 4.5. The atmospheric reference values were extrapolated for a altitude of 1524 meters (5000 feet) [116]. The density of the air inside the fluid volume was treated as an ideal gas and the viscosity described by the Sutherland law [101] .

Table 4.5: Reference values of the CFD calculations.

Area (wing) (m^2)	6.2
Density (kg/m^3)	1.061
Enthalpy (kJ/kg)	278.33
Length ($\overline{c}$) (m)	1.19
Pressure (kPa)	83.53
Temperature (K)	278.24
Velocity (m/s)	31.9
Viscosity ($kg/(m \cdot s)$)	$1.737 \cdot 10^{-5}$
Ratio of specific heats	1.4

The CFD model possesses five boundaries: inlet, outlet, far field, symmetry plane and the aircraft model. The flow direction is $(1, 0, 0)$, i.e., in the positive x direction. The boundary conditions applied were based several studies performed in an aircraft [103], [102], [101] . At the inlet, outlet and far field, pressure far field boundary conditions were applied. At the symmetry plane located at $z = 0$, symmetry conditions were applied. At the aircraft surface due to the no-slip and impermeability, the wall boundary condition was applied.

The set-up of the pressure far field boundary condition (see table 4.6) requires the free stream Mach number (M), flow Cartesian components, temperature and gauge pressure to be set. The Mach number was defined with the sound speed value at 5000 ft. The flow direction is in the x direction, the angle of attack could be defined by the flow components. However, due to to the errors associated with the flow-cell distortion effect, the author decided to generate a different mesh for each angle of attack. Hence, the flow direction is always with the Cartesian components: (1,0,0). The gauge pressure is zero: "...for low Mach number flows (M $<$ 0.3), the 'Operating Pressure' is set as the ambient atmospheric

pressure and therefore the gauge pressure can be set to zero." [104].

Table 4.6: Pressure far field boundary condition set-up.

Gauge Pressure (Pa)	0
Mach Number	0.095
Flow direction (x,y,z)	(1,0,0)
Temperature (K)	278.24

The governing equations might be linearised in an explicit or implicit manner, i.e., the unknown value in each cell is computed with both existing and unknown from the neighbouring cells or the unknown value in each cell is computed from existing values of the neighbouring cells, respectively. The implicit formulation was chosen due to being faster to achieve convergence, however it requires more memory than the explicit formulation [94]. For the density-based solver the convective flux type Roe flux-difference splitting Roe-(FDS) or Advection Upstream Splitting Method (AUSM) is available. The default flux is Roe-FDS and it is advised for most cases, hence it was the chosen one.

In the spatial discretization the gradient chosen was the Green-Gauss Node-Based gradient which is known to be more accurate than the cell-based gradient, however increasing the computation cost. The spatial discretization schemes available are either first or second-order. Although first order scheme often offers better convergence, for tetrahedral meshes (which is the case), where the flow is not aligned with mesh first order schemes are less accurate. Hence, the second-order upwind scheme was applied.

The CFL number for the Density-Based Implicit Formulation has a default value of 5. The implicit formulation is unconditionally stable according to linear stability theory. In theory the CFL number can be 100 or even higher. However, non-linearities in the governing equations often limit stability depending on the complexity of the problem. The flow simulation began with a CFL of 1, and it was gradually increased to 2 and then 5, since in general taking larger time steps leads to a faster convergence. This meant that the flow calculations would take less time to converge, which is an advantage for the present work due to the time constraints.

The unsteady calculations were performed with the mathematical model DES $k-\omega$ SST by changing the mathematical model and time to unsteady of the converged steady RANS solutions, this was advised by Professor Bidur from Coventry University. The previously mentioned settings remained the same, however the time step of 0.00067 s was defined following the DES guidelines of Spalart [76]. Spalart states that the time step is computed as the division between the grid spacing (Δ) of the focus region and the highest velocity found in the same region. The maximum speed found is usually 1.5 time bigger then the free stream velocity, hence the time step was computed with a velocity of 45 m/s.

Ultimately, steady RANS flow calculations applying the turbulence model $k-\omega$ SST of eight different angles of attack were perform, namely AoA = 5, 7.5, 10, 12, 14, 16, 18 and 20 $^\circ$. Due to time concerns and in order to perform the mesh sensitivity analysis, three mesh densities were performed for the pre-stall AoA=12 $^\circ$ and post-stall AoA = 18 $^\circ$.

Moreover, unsteady flow calculations were also performed with the application of the mathematical model DES with $k-\omega$ SST for the AoA= 14, 16 and 18 $^\circ$. The reasoning for this was the objective of

computing the vortex shedding frequency, which an unsteady phenomenon, at the same AoA where buffet was present in the flight tests. This is explained in further detail in the following sections.

4.1.4 CFD-Quantities of interest

The steady RANS flow calculations were performed in order to obtain the characteristic lift curve, the critical angle of attack, zero lift angle and maximum lift. In addition, to obtain the Drag coefficient values for the different AoA. Hence, the lift and drag coefficients were monitored and obtained from the flow calculations reports. Furthermore, the boundary layer separation pattern was visualised by obtaining the limiting streamlines contours on the upper surface of the wing and the skin friction coefficient contours, in the post-processing analysis of the results with the commercial software, ANSYS CFD-POST.

Applying DES was with the objective of computing the shedding frequency in the wing's wake and for that some probes in wake and the lift coefficient were monitored, see figure 4.10. In those probes, static pressure was monitored and they were chosen based on the vorticity contours on the x direction (flow direction) obtained with the post-processing tool, CFD-Post, obtained from the steady RANS flow calculation.The vorticity contour for the AoA=18° is shown in figure 4.11. The probes were located in the regions where the vorticity was captured with the RANS model. Moreover, the lift and drag coefficient were obtained to compare the results with the steady RANS flow calculations.

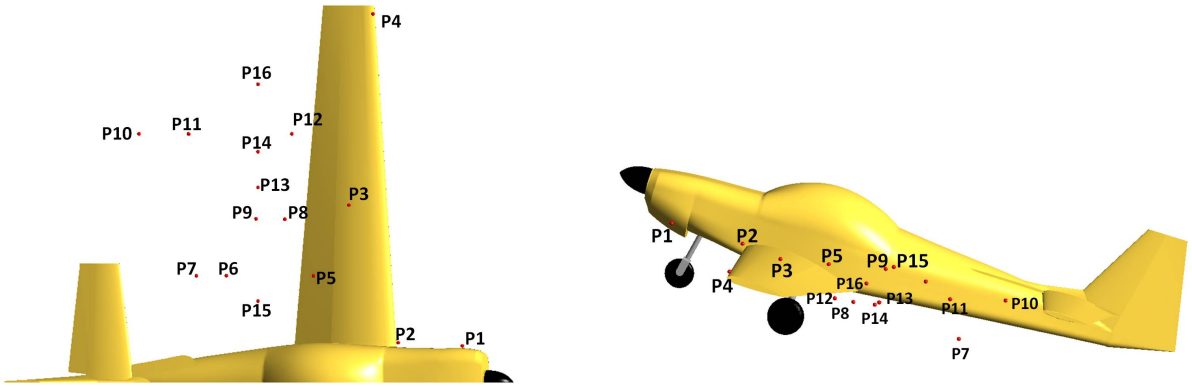

(a) Upper view of the DES probes in the wake.

(b) Side view of the DES probes in the wake.

Figure 4.10: Probes monitored in the CFD flow calculation with the application of the mathematical model DES.

Figure 4.11: Vorticity Contour for the steady RANS flow calculations for an AoA = 18 ° .

4.2 Flight Tests

4.2.1 Flight test conditions

In order to obtain a qualitative evaluation of the CFD results several flight tests were performed. The flight tests were performed in the Slingsby Firefly T67M260 and at a constant altitude of 1524 m (equivalent to 5000 ft). The flight test conditions were obtained from the International Standard Atmosphere (ISA) data [117] and are shown in table 4.7.

Table 4.7: ISA conditions at 1524 m [117].

Altitude (m/ft)	Ambient pressure (kPa)	Ambient temperature (K)	Density (kg/m^3)	Viscosity (kg/ms)
$1524/5000$	83.53	278.24	1.061	$1.737 * 10^{-5}$

The tests were structured and planned by the author in order to obtain the characteristic lift curve of the Slingsby for a pre-stall flight condition, the critical angle of attack, the boundary layer flow separation pattern and the buffet frequency.

4.2.2 Straight and Level flight test

A flight test was performed at a straight and level (unaccelerated) flight in which the aircraft was flown at different constant airspeeds. The maximum airspeed was 120 knots and the minimum was 60 knots. The altitude is maintained constant, in this case 5,000 ft. By doing so, a range of pre-stall angles of attack can be obtained and the respective lift and drag force can be estimate.

During flight, directly obtaining the angle of attack of the wing would be a difficult task with the resources available, hence it was computed based on different reference lines and with the CAD model available of the aircraft. Thus, an inclinometer was placed inside the cockpit in the reference line in green, shown in figure 4.12. Prior to the flight test, while the aircraft was parked, the angle of the mentioned reference line (ϕ) was recorded and had a value of 2.75 $^\circ$. This was done in order to know the angle variation for the different airspeeds during the flight test. In addition, another angle was measured, the angle of the reference line in blue (β) and had a value of 8.25 $^\circ$. In theory, the angle ϕ could be used to directly compute the AoA, however this line was not accurately represented in the Slingsby model. Hence, the variation of β was used to compute the wing's AoA, since this line was accurately represented in the Slingsby CAD model and the difference between the angle ϕ and β was known prior to the flight test. The wing AoA has a difference of 5.63 $^\circ$ to the angle β, according to the CAD model. Ultimately, the AoA could be computed.

The values measured during flight of the previously mentioned angles are shown in table 4.8. It is observed that the maximum AoA reached in the flight test was 11.27 $^\circ$, which is below the usual critical angle of attack of a light aircraft. In fact, the stall speed was reached but the condition was not maintained for a significant time for the aircraft to be stalled, i.e., a wing drop did not occur. Ergo, this flight test only characterizes the pre-stall condition of the aircraft.

Figure 4.12: Aircraft reference lines.

Table 4.8: Steady and Level flight test airspeeds and angles measured.

IAS (knots)	ϕ (°)	β(°)	AoA (°)
120	2.57	8.07	2.44
100	3.58	9.08	3.45
80	5.55	11.05	5.42
70	9.69	15.19	9.56
62	10.3	15.8	10.17
60	11.4	16.9	11.27

An aircraft flying in a straight and level flight is subjected to four main forces: thrust (T), weight (W), drag (D) and lift (L). The lift is balanced by the weight and thrust by drag, the balance of forces is shown in equations 4.7 and 4.8.

$$Lift = Weight \quad [N]\,. \tag{4.7}$$

$$Thrust = Drag \quad [N]\,. \tag{4.8}$$

However, in the mentioned flight test the speed is reduced and to maintain the same altitude the aircraft will increase the AoA of the wing to produce more lift. This results in a vertical component of thrust, hence the balance of forces will change as shown in equations 4.9 and 4.10. The angle σ is the angle between the engine reference line and the horizontal. The angle σ is 6 ° lower than the β, shown in figure 4.12. The schematic of the forces is shown in figure 4.13.

$$Lift = Weight - Thrust \cdot sin(\sigma) \quad [N]\,. \tag{4.9}$$

$$Drag = Thrust \cdot cos(\sigma) \quad [N]\,. \tag{4.10}$$

Thus, lift was computed with the weight of the aircraft minus the vertical component of thrust. The total weight is a combination of the passengers, fuel and empty aircraft weight. The fuel in the Slingsby is inside both wings and it can be read in the fuel gauge. Before the flight test was performed, the value in both wing tanks was measured and had a value of 65 in the left wing and 56.5 litres in the right wing. The fuel is AVGAS which has a density of 0.721 kg/m^3, hence the fuel weighted 860 N. The two passengers and the empty aircraft had a total wight of 8848.6 N. The total weight of the aircraft was

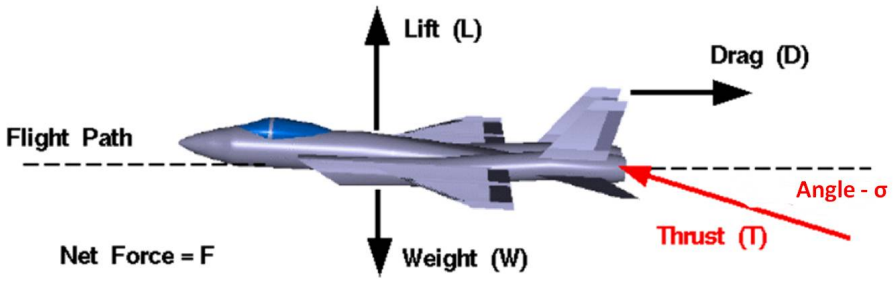

Figure 4.13: Diagram of forces in an aircraft (Adapted from: [118]).

9708 N, which corresponds to the lift force of the aircraft. The lift coefficient is then computed as follows:

$$C_L = \frac{Lift}{\frac{1}{2}\rho TAS^2 S}\,. \tag{4.11}$$

where ρ is density for the flight conditions, S is the wing area and TAS is the True Air Speed.

The speed measured during flight with the Air Speed indicator gauge, is the Indicated Air Speed (IAS) . The IAS is the airspeed relative to the standard sea-level, hence it needs to be converted to the TAS, which accounts for the difference in density at 1524 m. In present work it is assumed that the only correction needed to be made is the one to obtain the TAS. It is important to refer, if some more data were to be available, a Calibrated Air Speed and a Equivalent Air speed should be equated. These two speeds account for the correction of the calibration of the measuring instrument and in the presence of compressibility effects, a Bernoulli equation correction, respectively [32]. The IAS measured by the Air Speed Indicator is calibrated for sea level conditions. hence the conversion to True Air Speed is done as followed:

$$dynamic\ pressure@5000ft = dynamic\ pressure@sea-level \tag{4.12}$$

$$(\frac{1}{2}\cdot\rho\cdot v^2)_{@5000ft} = (\frac{1}{2}\cdot\rho\cdot v^2)_{@sea-level}\,. \tag{4.13}$$

$$v_{5000ft} = \sqrt{\frac{(\rho\cdot v^2)_{@sea-level}}{\rho_{5{,}000ft}}} \tag{4.14}$$

The thrust (T) is computed from the power (P) and True Air Speed (TAS), i.e., $T = \frac{P}{TAS}$. The power is obtained from an engine graph [6] from the engine supplier of the Slingsby that correlates the manifold pressure (MP), which measures the pressure inside induction system of the engine, and RPM to obtain the horse power (HP). Hence, the manifold pressure and RPM were also monitored for each air speed. The manifold pressure gauge indicates the manifold pressure (measured in inches of mercury) and the RPM is indicated in the tachometer, the location of the gauges inside the cockpit is shown in figure 4.14. The Drag is obtained with equation 4.10 and the drag coefficient is similar to the lift coefficient (equation 4.11), however the lift force is substituted with the drag force. The data processed from the flight test are shown in table 4.9.

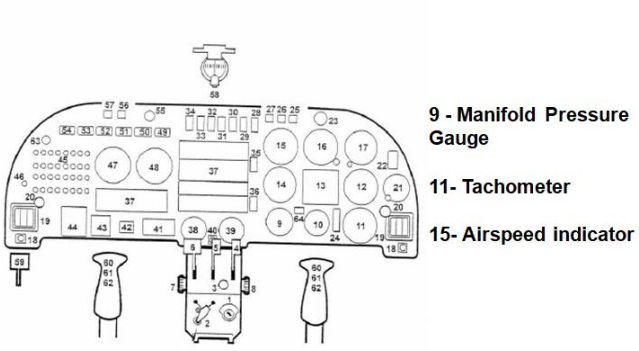

Figure 4.14: Instrument panel of the Slingsby Firefly (Adapted from: [8]).

Table 4.9: Post-processed data from steady and level flights.

IAS (knots)	TAS(knots)	RPM	MP (in. Hg)	HP	P (Kw)	σ (°)	T (N)	L(N)	D(N)
120	129.28	2700	20	175	130.5	2.07	1962.015	9637.12	1960.74
100	107.74	2600	18	148	110.36	3.08	1991.165	9601.01	1988.29
80	86.19	2400	17	136	101.42	5.05	2287.15	9506.66	2278.27
70	75.42	2300	16	100.5	74.94	9.19	1931.58	9399.50	1906.79
62	66.79	2200	16	85	63.38	9.8	1844.48	9394.04	1817.57
60	64.64	2100	15	20	14.91	10.9	448.46	9623.19	440.37

The standard estimated errors of flight tests are shown in table 4.10 and they were based on the study developed by Lawson et al. [102]. Additional errors are present that are difficult to estimate. For instance the measurement of the angle ϕ, that was recorded with fotographs, as the test pilot maintained a constant altitude and air speed. Nevertheless, there will always be deviations in the results and external factors that affect the results obtained. It is observed, that the angle measured in the inclinometer would oscillate between values for the same power set, hence for one, three measurements were taken and averaged. Moreover, the HP was extrapolated from a theoretical graph from the engine supplier, Lycoming [6], thus extrapolation errors are present.

Ideally, the flight test should be repeated several number of times in order to minimize these errors, however the resources were limited and that was not possible.

Table 4.10: Summary of the estimated errors in the flight test (Adapted from: [102]).

Variable	Standard error
Inclinometer (ϕ, β)	$\pm$ 0.01 °
Aircraft empty mass	$\pm$ 0.1%
Fuel Mass	$\pm$0.3%
TAS	$\pm$ 2 Knots
Manifold Pressure gauge	$\pm$ 1 in. Hg
Tachometer	$\pm$ 1 RPM

4.2.3 Stall angle of attack flight test

The α_{stall} was obtained with a different flight test due to the previous flight test only accounting for the pre-stall condition of the aircraft. The aircraft was stalled at a constant deceleration rate and engine idle, maintaining a straight and level flight.

In order to compute the α_{stall}, a camera mounted inside the cockpit recording the instruments panel, an inclinometer with the camera recording the angle and an iPad with the software Airbox RunwayHD were used. The camera was recording the artificial horizon gauge that shows the pitch attitude hence obtaining the pitch angle (θ), the vertical speed indicator and altitude. The software used is a GPS that logs both the altitude and air speed. It can be argued that one could used the Airspeed Indicator to obtain the aircraft speed, however due to the increase AoA the air speed indicator is not reliable. This is owing to the pitot tube is no longer aligned with the flow, thus the airspeed indicator is actually showing a lower speed than it is in reality. The aim was to compute the flight path angle (γ) with both the vertical and horizontal air speeds thus obtaining the angle of attack with the pitch attitude angle. The pitch angle (attitude) is the angle between longitudinal axis and the horizon. The AoA is obtained by the difference between the pitch angle and the flight path angle. The relation between these angles is shown in figure 4.15 . Although the inclinometer was positioned at the same reference line as the previous flight test in order to validate the flight tests AoA, the video image was not perceptible. The inclinometer would be used as a confirmation tool of the AoA computed from the horizontal and vertical airspeeds.

The monitored quantities are shown in table 4.11 and a colour code is shown to differ the three different parts of the flight test data. The cells in green represent the deceleration until the stall speed is reached, up to this point the stall warning was still disabled. The Slingsby stall warning is both visual and auditory. The cells in blue represent the time between the beginning of the stall warning and the wing drop. The natural stall warning, buffet, occurred in the final four seconds before the wing dropped. The cells in red represent the post-stall data, where a wind drop occurred, the stall was recovered hence the aircraft did not develop a spin.

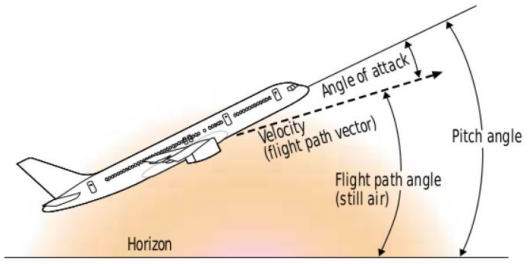

Figure 4.15: Different angles in an aircraft [119].

The errors associated with this flight tests are due to the aircraft gauges and the GPS software that recorded the airspeed. The estimated errors associated with the aircraft instruments are shown in table 4.12.

Table 4.11: Data obtained from the critical angle of attack flight test.

Time (s)	IAS(knots)	Vertical Speed (knots)	Pitch attitude angle (θ))
1	73	-0.00987	0
2	70	-0.014805	0
3	70	-0.014805	0
4	68	-0.014805	0
5	67	-0.01974	0
6	66	- 0.01974	0
7	64	- 0.01974	0
8	63	- 0.01974	0
9	62	-0.01974	5
10	62	-0.014805	7
11	62	-0.01974	7
12	61	-0.01974	9
13	60	- 0.01974	10
14	58	-0.01974	10
15	58	-0.014805	11
16	57	-0.01974	12
17	55	- 0.01974	13
18	55	- 0.014805	15
19	55	-0.00987	13
20	55	-0.004935	7

Table 4.12: Summary of the estimated errors present in the critical angle of attack flight test.

Variable	Standard error
Artificial horizon gauge (θ)	$\pm$ 1 $^\circ$
Vertical Speed Indicator	$\pm$ 50 ft/min
TAS	$\pm$ 2 Knots

4.2.4 Flow visualisation flight test with wool tufts

In order to be able to identify the boundary layer flow separation patterns on the upper surface of the wing, flow visualisation techniques in-flight were required. The most suitable flow visualisation techniques to detect flow direction and boundary layer separation are either flow cones and tufts or emitted fluid technique [120]. The wool tufts visualisation technique was chosen due to the its practicality but also for being a standard method of flow visualisation.

Ergo, the third flight test consisted in the observation of the boundary layer separation progression with wool tufts on the upper surface of the wing, while the aircraft was stalled and a wing drop occurred. The aircraft was stalled twice by reducing its speed until its stall speed which is around 62 knots ($\approx$ 32 m/s), engine idle, maintaining level flight and in cruise configuration. The wool tufts were placed on the boundary layer ($\delta = 2.4\ cm$, according to what was presented in section 4.1.2) and it should be expected that the wool tufts remained aligned with the flow and undisturbed when the aircraft is not approaching stall. When the aircraft is stalled the boundary layer will begin to separate and the wool tufts will possess a disturbed behaviour in the sense that they will not be aligned with the flow direction.

The left wing of the Slingsby Firefly was covered by wool tufts of 5 mm thickness 15 cm length in a structured pattern, i.e., the tufts were vertically and horizontally spaced 24 cm. This structure was

based on the work developed by Hoff [9], in which this structured allowed for the observation of several patterns upon spinning an aircraft. Due to the fuel tank and taper of the wing some of the tufts were reduced in length and spacing in order to be able to cover most of the wing upper surface. The tufts schematic is shown in figure 4.16, the green arrows represent the spacing and the blue the length of the wool tuft. This resulted in 62 wool tufts that were attached to the upper surface of the wing with paper tape. There was a camera installed inside the cockpit with a view towards the wing in order to record the wool tufts behaviour.

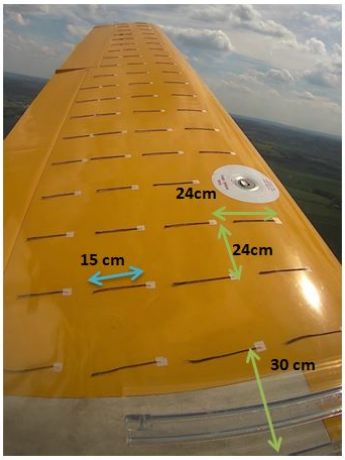

Figure 4.16: Wool tufts scheme on the upper surface of the wing.

The error associated with this flight test is only applying a wool tuft structure and length. In order to understand the coherence of the flow separation pattern, different structures of the wool tufts should be tested and also different lengths. However, that was not possible due to time available to perform the flight test.

4.2.5 Buffet Frequency flight test

Approaching stall there will be a vibration of the structured of the aircraft known as buffet, induced by the vortex shedding resultant from the separation of the flow. In the cockpit three sensors were mounted in three different locations shown in figure 4.17. The available sensors were the Shimmer3 [121] which have an accelerometer, magnetometer and a gyroscope. The vertical acceleration was analysed in order to compute the buffet frequency induced by the vortex shedding of the wing's wake. The sensor has a range of $\pm$ 2 g. The aircraft was stalled with the same procedure describe in the critical angle of attack flight test, in section 4.2.3.

The data frequency acquisition was 100 Hz and a Fast Fourier Transform (FFT) was performed in order to convert the signal in the time domain to the frequency domain. In this flight test there was also a camera in the cockpit in order to synchronize the sensors with the events. There was a mechanical tap in each sensor while approaching stall that can be seen in the signal as a peak, see figure 4.19. The camera is important since the time before the mechanical tap and stall warning can be known, with visual and auditory data, figure 4.18 shows the activated stall warning. In figure 4.19 the flight test signal,

captured by one of the accelerometers, from pre-stall and post-stall conditions are shown. There is a g-break, as explained in section 2.1.2, characteristic of stall where there is a reduction in lift. Prior to that, there is a 4 second buffet that warns the pilot of imminent stall that is shown inside the rectangle in figure 4.19. As previously mentioned, the buffet had a duration of 4 seconds and the FFT was performed in this interval in order to compute its frequency.

The error associated with the measured vertical acceleration is not specified in the technical specifications of the sensor. In addition, the synchronization errors are present, i.e., with the data signal and the recorded video in the flight test. Sensor number 1 and 3, located on the sides of the cockpit were able to capture the buffet frequency, however sensor number 2 was not. The signal obtained from the latter had too much noise from the engine and it was not properly mounted to the structure of the aircraft.

Figure 4.17: Sensor's position inside the cockpit.

Figure 4.18: Stall warning of the Slingsby Firefly.

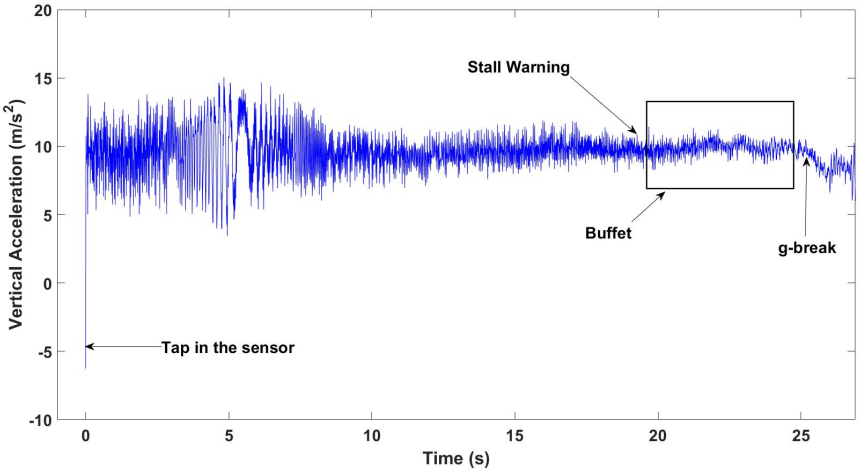

Figure 4.19: Data signal obtained from the accelerometers in the buffet flight test.

Chapter 5

Results

In this chapter the mesh sensitivity analysis is performed and the results obtained from CFD and flight tests are analysed and compared. The lift curve, the critical angle of attack and the maximum lift obtained from the simulations performed with the steady turbulence model $k-\omega$ SST and the mathematical model DES with $k-\omega$ SST are presented and compared with data gathered from the steady and level flight tests. In addition, the boundary layer flow separation pattern is obtained with the same turbulence model ($k-\omega$ SST) with limiting streamlines contours. The contours of the limiting streamlines were compared with wool tufts flight test where the aircraft was stalled and the wool tufts behaviour recorded. In addition, DES were performed to the converged solutions of the AoA =14, 16, 18 $^\circ$ of the RANS $k-\omega$ SST results. The aim of this study was to monitor the static pressure at several probes in the wing's wake and the lift coefficient for the three AoA, in order to compare the results with the buffet frequency. This frequency was obtained using accelerometers while stalling the aircraft.

5.1 Mesh Sensitivity Analysis

A mesh sensitivity analysis was performed, for two solutions at different AoA obtained from the steady $k-\omega$ SST flow calculations, in order to evaluate the most suitable mesh density that the simulations could be performed. The aim was to understand the influence of the mesh density on the boundary layer flow separation progression, lift and drag coefficients and finally the pressure coefficient at three different sections on the wing. Ultimately, choosing the mesh density that should be applied to perform the CFD flow calculations at the different AoA, with regard to its computational time and physical accuracy.

Three different mesh densities were used to perform the mesh sensitivity analysis, at a pre-stall AoA = 12° and a post-stall AoA = 18°. The coarse mesh had a total of 7.57, the medium had 11.3 and the fine mesh had 17.15 million. The modifications performed on the mesh were only applied to the wing due to its importance on the results obtained. Detailed information about the three mesh densities' size and quality is presented in appendix A.1 and A.2.

The flow calculations performed in this chapter of results were obtained with double-precision in order to have a negligible contribution of the round-off error. The convergence criteria was chosen according the guidelines of ANSYS Fluent, the globally scaled residuals should drop to 10^{-3} . Lift and drag coefficients were monitored, and convergence was obtained when perturbations in lift and drag coefficient reached less than 10^{-4} in both cases. Moreover, the mass imbalance (MI) was also monitored. The values of the drop in residuals and mass imbalance are shown in table 5.1.

Table 5.1: Percentage of mass imbalance and decrease in residuals for the AoA = 12 and 18 °.

AoA (°)	Mesh density	MI (%)	Continuity	x-velocity	y-velocity	z-velocity	k	ω
12	Coarse	0.0013	10^{-4}	10^{-4}	10^{-4}	10^{-4}	10^{-3}	10^{-5}
12	Medium	0.0011	10^{-3}	10^{-4}	10^{-4}	10^{-4}	10^{-3}	10^{-5}
12	Fine	0.0009	10^{-3}	10^{-4}	10^{-4}	10^{-4}	10^{-3}	10^{-5}
18	Coarse	0.0075	10^{-3}	10^{-4}	10^{-4}	10^{-4}	10^{-3}	10^{-5}
18	Medium	0.0018	10^{-3}	10^{-4}	10^{-4}	10^{-4}	10^{-3}	10^{-5}
18	Fine	0.00044	10^{-3}	10^{-4}	10^{-4}	10^{-4}	10^{-3}	10^{-5}

The results of the lift (C_L) and drag (C_D) coefficient and their respective deviation to the fine mesh for the AoA = 12° and 18° are shown respectively in tables 5.2, 5.3. The results from the flow calculations with an AoA = 12 ° for the drag coefficient show that in general the coarse and medium mesh over predict the drag coefficient. The relative deviation for the coarse mesh has a value of 5.65 % and the medium mesh a value of 2.42 %. The lift coeffcient has a contrary trend, the coarse and fine mesh under predict the value of C_L when compared with the fine mesh, however the deviation is higher for the coarse mesh. For the CFD solution with AoA = 18 °, the same trend is verified for the drag coefficient. However, for the C_L the coarse mesh under predicts its value and the medium over predicts, as shown in table 5.3.

In addition, the computational time required for the convergence to be obtained for each mesh was of utmost importance due to the time available to perform the simulations. The computational time increases substantially with the increase in mesh density. The fine mesh requires more computational time than the other two mesh densities, hence performing all the CFD flow calculations with this mesh density would not be feasible. The choice was then between the coarse and medium mesh. Compared to the fine mesh, the medium mesh showed lower deviation of C_L and C_D than the coarse mesh.

Table 5.2: Mesh sensitivity analysis: Lift and Drag coefficients and respective relative deviations for the flow calculations at AoA=12 °.

Mesh	Nº of cells	C_D	ΔC_D (%)	C_L	ΔC_L (%)	CPU Time (hours) *
Coarse	7.57	0.131	5.65	1.074	-6.77	31
Medium	11.3	0.127	2.42	1.129	-1.99	59
Fine	17.15	0.124	-	1.152	-	85

* The CPU time is relative to the same amount of iterations performed: 8000 iterations.

Table 5.3: Mesh sensitivity analysis: Lift and Drag coefficients and respective relative deviations for the flow calculations at AoA = 18 °.

Mesh	Nº of cells	C_D	ΔC_D (%)	C_L	ΔC_L (%)	CPU Time (hours)*
Coarse	7.57	0.252	3.27	1.060	-5.19	45
Medium	11.3	0.249	2.05	1.134	1.43	58
Fine	17.15	0.244	-	1.118	-	84

*The CPU time is relative to the same amount of iterations performed: 8000 iterations.

Nevertheless, evaluating the mesh based solely on its numerical deviation and computational time is not sufficient. Ergo, the physics was also compared in order to understand which mesh would produce the most physically accurate solutions, always comparing to the fine mesh. Hence, the limiting streamlines contours where compared for the three meshes.

For the AoA= 12 ° (see figure 5.1) the coarse mesh over predicts the area where the flow separation occurs this is the reason why the lift coefficient was highly under predicted. The medium mesh is quite similar to the fine mesh, hence the C_L deviation of -1.99 %.

In AoA = 18 ° (see figure 5.2), the structures observed resultant from flow separation are quite different between the three mesh densities. The fine mesh captures two stall cells, and the coarse and medium mesh only one. From section 2.3.2, it is known that the fine mesh presents the number of stall cells that would be expected. Moreover, the area correspondent to the flow separation on the upper surface of the wing is similar between the medium and fine meshes. A red line is shown in figure 5.2 and it represents a structure that has a triangular shape of the boundary layer flow separation. It is observed that the location of that structured has a similar span location for the medium and fine meshes, contrary to the coarse mesh where that structure appears in a further span location. Moreover, the area of attached flow is smaller for the coarse mesh than for the medium and fine mesh, this explains why the lift coefficient is lower than the fine mesh.

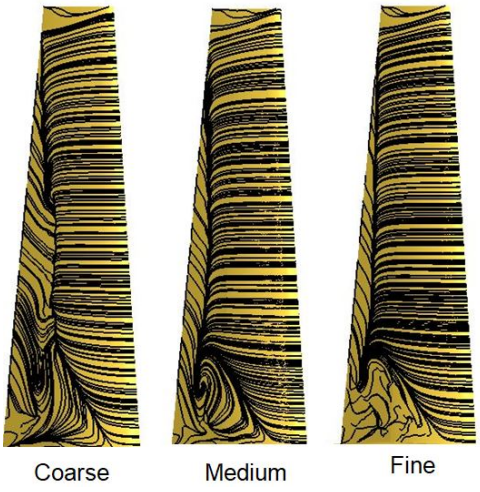

Figure 5.1: Limiting streamlines contours for the three different mesh densities: AoA=12 °.

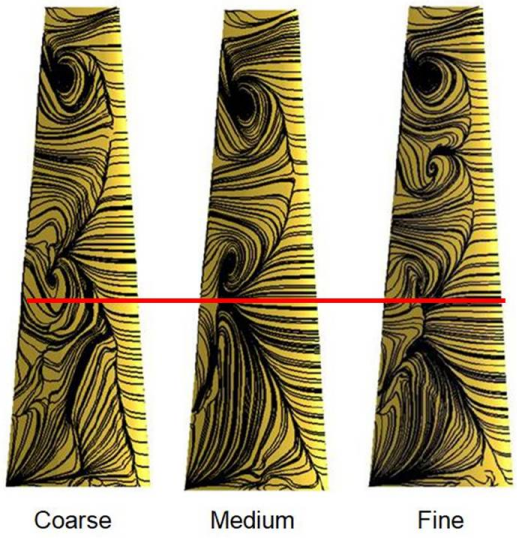

Figure 5.2: Limiting streamlines contours for the three different mesh densities: AoA=18 °.

The pressure coefficient distribution was also computed in three different sections of the wing, strategically placed in order to have different sections of the wing represented. The first plane was set at a location $z = 1.5$ m, which is a plane close to the wing root and fuselage, the second one is mid-span at $z = 2.5$ m and the final plane is closer to the tip at $z = 4$ m. Their location in the wing is shown in figure 5.3. The aim was to understand if the pressure coefficient would remain somewhat similar between the medium and fine meshes at three different sections in the wing.

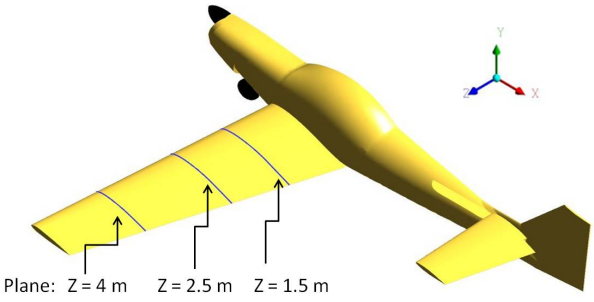

Figure 5.3: Location of the three distinct wing sections at the planes: $z = 1.5,\ 2.5\ \&\ 4$ meters where the pressure coefficient was obtained.

The negative pressure coefficient ($-Cp$) as a function of the normalized chord (x/c) was computed for each mesh density for the two different AoA = 12 and 18°. The graphs shown in figures 5.4 and 5.5, show the results of the $-Cp$ obtained for the plane $z = 1.5$ m for the AoA = 12 and 18 °, respectively. It is observed that the the medium mesh has a almost identical pressure distribution to the fine mesh, contrary to the coarse mesh that not only has a different pressure distribution but also under predicts the lift in the respective section of the wing. This is choerent with the C_L values previously showed. The same trend is verified for the remaining pressure coefficient graphs for the two different planes, $z = 2.5$ and 4 meters, see graphs in Appendix A.3. The pressure distribution shown is coherent with the lift coefficients obtained and the flow separation pattern previously shown.

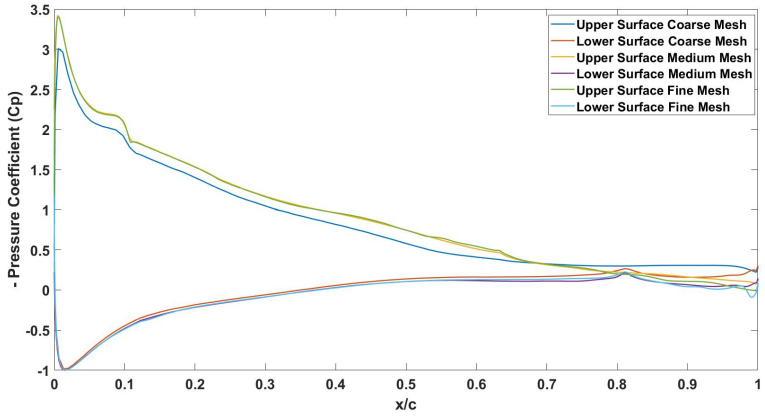

Figure 5.4: Negative Pressure Coefficient as a function of the normalized chord of the AoA= 12° for the three mesh densities at a plane $z = 1.5\ m$.

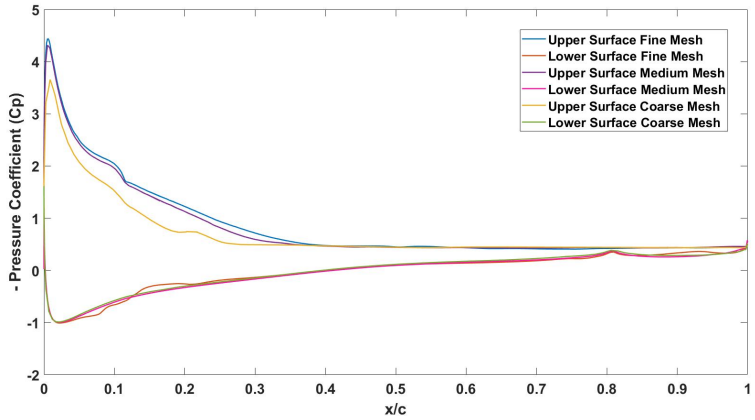

Figure 5.5: Negative Pressure Coefficient as a function of the normalized chord of the AoA= 18° for the three mesh densities at a plane $z = 1.5\ m$.

Ultimately, regarding the deviation in lift and drag coefficients, different boundary layer separation patterns and pressure distributions for the three mesh densities, it its observed the medium mesh is the most suitable mesh. Not only due to the similarity of mentioned results but also due to the computational time required for the flow calculation to be converged.

5.2 Comparisson between CFD and flight tests

5.2.1 Lift curve, critical angle of attack and maximum lift coefficient.

This section presents the results obtained from the steady RANS and DES flow calculations using a medium mesh, for the reasoning stated in the previous section. The aim is to qualitatively evaluate the CFD results with the flight tests data of the lift and drag coefficient, maximum lift coefficient, critical angle of attack and zero lift angle. The CFD results are firstly presented, followed by the flight tests data and finally they are compared qualitatively and quantitatively to the flight tests.

The lift coefficient as a function of the AoA (relative to the mean aerodynamic chord of the wing),

obtained from the CFD calculations using the steady RANS turbulence model $k-\omega$ SST and the mathematical model DES with $k-\omega$, is shown in figure 5.6. The range of AoAs studied are from 5-20 ° with a 2° interval for the steady flow calculations and the AoA= 14, 16 and 18 ° for the DES.

The lift curve obtained from the steady RANS calculations has two distinct regions: a region where a linear behaviour is observed up until a certain angle is reached, i.e., α_{stall} that corresponds to the maximum lift coefficient, and a region after which the increase of angle of attack no longer produces more lift.

The first region (AoA = 5-14°) corresponds to an approximately linear variation of lift, this means an increase in α would result in a direct increase in lift. The linear curve is defined by :

$$C_L = a \cdot \alpha + C_{L0} = a(\alpha + \alpha_0) \tag{5.1}$$

where a is the curve slope: $\frac{dC_L}{d\alpha}$ and α_0 is the zero lift angle.

The best linear fit curve for the results obtained is given by: $C_L = 0.0845\alpha + 0.0734$, this means that $dC_L/d\alpha \approx$ 0.0845 and that the zero lift angle is ≈ -0.87 °. According to the lifting line theory, the lift coefficient is obtained as follows:

$$C_{L3D} = \frac{C_{L2D}}{1 + \frac{57.3 C_{L2D}}{\pi AR}}(\alpha + \alpha_0) \tag{5.2}$$

where $C_{L2D} = 0.1097 C_L/^\circ$ is the slope of a 2D aerofoil and AR is the aspect ratio of the wing, which is 9. The lifting-line theory gives a lift coefficient of 0.0898, giving a deviation of the ≈ -6% of the CFD results obtained with the RANS turbulence model, $k-\omega$ SST. The lifting-line theory only accounts for the lift of a finite wing, whereas the CFD model has the influence of other components, hence the lift slope of the CFD results ought slightly different from the lifting line theory slope.

This linear behaviour of the lift coefficient no longer applies after the critical angle of attack is reached, which corresponds to the maximum lift coefficient (C_{Lmax}). For the mentioned results, the values of α_{stall} and C_{Lmax} are respectively 16° and 1.244.

The second region of the curve corresponds to the post-stall conditions after which increasing the angle will result in a loss of lift. At this stage the flow is massively separated, and in a flight this results in a wing or nose drop. For a trailing-edge stall a gradual loss of lift should be expected in this region. In fact from the critical angle of attack up to AoA = 20 ° there is a decrease of 0.206 in the value of the lift coefficient, it is concluded that there is a gradual loss of lift.

The DES values of lift coefficient are also presented in figure 5.6 and in table 5.4. Due to the computational time required for the DES flow calculations, which took five days in order to have one second of flow time calculated, the averaging of flow was started after one flow passage. The results presented are from an averaged flow passage. The total flow time simulated was two flow passages, which corresponds to 11 seconds of flow time. The residuals dropped to 10^{-5} in each time step, which according to ANSYS guidelines is sufficient to obtain convergence at each time step. Hence, DES was only applied to the AoA = 14, 16 and 18 ° due to time available for this project and the AoA for which buffet would occur. The values of the lift coefficient are higher for the DES than the RANS solutions. For

the AoA studied with DES the flow is highly separated and unsteady, hence the RANS model fails to accurately predict the lift coefficient. Since DES accounts for the unsteadiness of the flow and different scales of turbulence, it should be expected values of the lift coefficient closer to the flight test values.

Prior to the comparison with the flight tests results, the CFD results ought to be analysed. It has been previously mentioned that the model of the aircraft does not possess a propeller. The propeller augments lift over the section of the wing, affected by the propeller slipstream [102]. In fact not only the lift coefficient will be higher but also the α_{stall}, i.e., there will be a destalling effect [122]. Hence, it should be expected (when comparing with the flight tests results) that the lift coefficient obtained from the CFD flow calculations will be under predicted, since there is no propeller and the flight tests were performed with the propeller running. Moreover, the DES lift coefficient values are higher than the steady RANS flow calculations results. This was expected since DES accounts for the unsteadiness of the flow, thus producing more realistic solutions. Furthermore, an accurate representation of the boundary layer in the meshing process was only performed for the main lift device, i.e., the wing. Nevertheless, the aircraft has other small lifting devices, such as the horizontal tail, which if modelled correctly would contribute for the increase in the lift coefficient results. However, due to the computational resources available that was not possible.

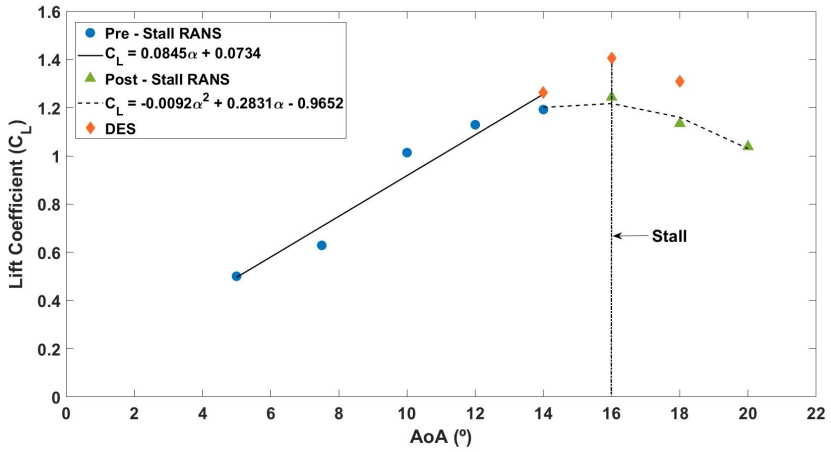

Figure 5.6: Lift Coefficient as a function of the AoA obtained from steady RANS $k-\omega$ SST and DES with $k-\omega$ SST flow calculations.

Table 5.4: Lift coefficient values obtained from steady RANS $k-\omega$ SST and DES with $k-\omega$ SST flow calculations.

AoA (°)	$C_{L(RANS)}$	$C_{L(DES)}$
5	0.508	-
7.5	0.629	-
10	1.014	-
12	1.129	-
14	1.193	1.263
16	1.244	1.407
18	1.134	1.309
20	1.038	-

The drag coefficient as a function of the AoA is shown in figure 5.7. The best fit curve is a parabola: $C_D = 0.014\alpha^2 - 0.0213\alpha + 0.1851$, as it was expected (see section 2.1.2). The total drag is the sum of the induced drag (D_i) and the profile drag ($D_{profile}$). The profile drag is divided in pressure and friction drag. The induced drag is proportional to the square of the lift coefficient and is defined as:

$$C_{Di} = \frac{C_L^2}{\pi AR}(1+\delta) \tag{5.3}$$

where $(1+\delta) = 1.050$ for a tapered with with a taper ratio of 0.5 such as the Slingsby Firefly [123]. Hence, the contribution of the induced drag to the total drag is a parabola and has the following mathematical expression: $C_{Di} = 5.3 \cdot 10^{-5} + 9.21 \cdot 10^{-4} + 0.00567$. The induced drag accounts for a small portion of the total drag, for instance for an AoA = 14 $^\circ$ is only 9 % of the total drag.

The pressure drag is due to the shape of the object, when the body is streamlined, i.e., when the wing is at low AoA, this is not the dominant type of drag. However, when flow separation is present the shape of object will increase hence so does the pressure drag. The friction drag is due to the shear-stress at the wall, when the flow is separated the wall shear-stress is negative, hence decreasing the total friction drag. Hence, for lower AoA when the flow is not highly separated the dominant drag is the friction drag. For high AoA, when the boundary layer separation occurs the pressure drag increases and it becomes the dominant source of drag.

The drag coefficient does not increase very rapidly up to the AoA = 12°. This is due to fact that, until this AoA the flow in the boundary layer is mainly attached. After this AoA, the flow begins to be highly separated, hence augmenting the total drag coefficient rapidly. The non-existence of a propeller in the CFD model has also an impact on the value of the drag coefficient. The effect of the propeller on drag is mainly owed to: the component of profile drag from the local skin friction increases and an induced component of drag due to the propeller slipstream [102], [124], [125], [126]. Ergo, an under prediction of the drag coefficient should be expected. The DES drag coefficient values are also presented, there is an increase in drag compared to the RANS solutions. The reasoning for this is the same stated for the lift coefficient. The results obtained are summarized in table 5.5.

Table 5.5: Drag coefficient values obtained from steady RANS $k-\omega$ SST and DES with $k-\omega$ SST flow calculations.

AoA ($^\circ$)	$C_{D(RANS)}$	$C_{D(DES)}$
5	0.099	-
7.5	0.121	-
10	0.124	-
12	0.1127	-
14	0.152	0.17255
16	0.196	0.211
18	0.249	0.259
20	0.329	-

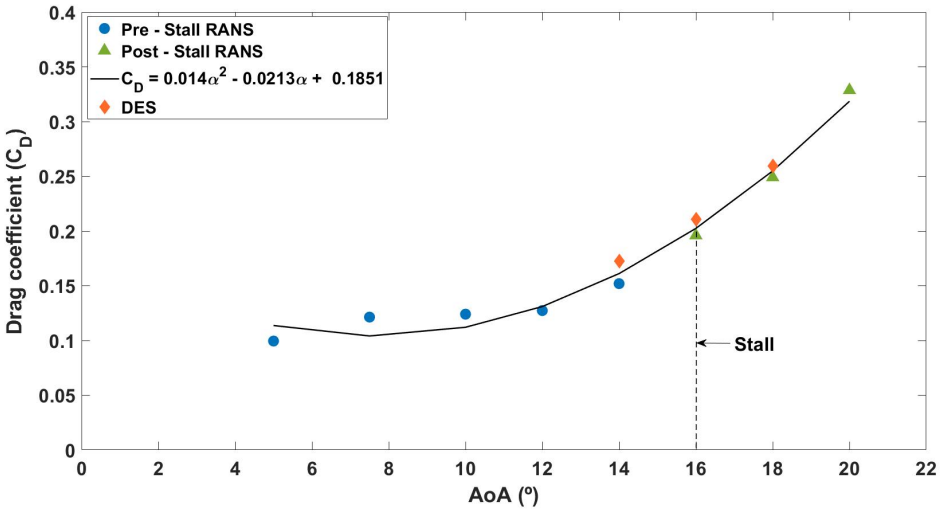

Figure 5.7: Drag coefficient of the RANS and DES flow calculations as a function of the AoA.

In addition to the data already presented, another interesting graph, presented in figure 5.8, can be computed is the lift/drag ratio curve. This curve shows the AoA that the aircraft has best performance from an aerodynamics point of view. The AoA correspondent to the most efficient setup is 12°. It is observed that the lift increases very rapidly from 8-12 °, however after this the drag increases at a higher rate than the lift coefficient hence the negative slope.

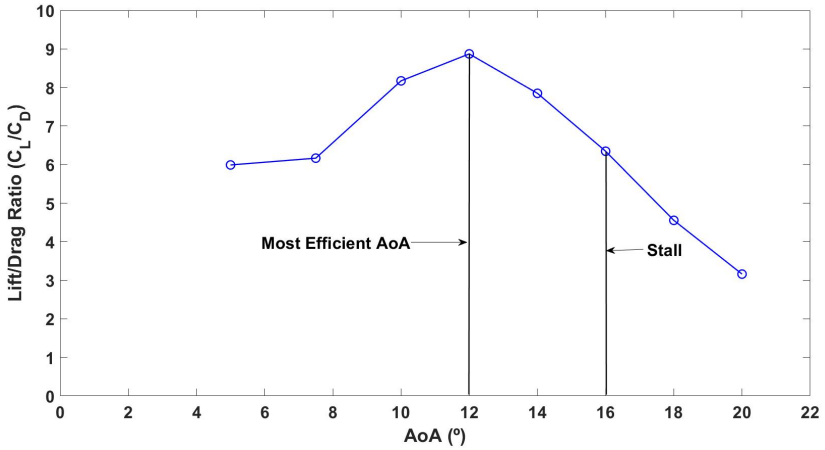

Figure 5.8: Lift/Drag ratio curve as a function of the AoA.

These results were compared with the flight tests results, more specifically the straight and level flight tests. In section 4.2 the forces applied in the aircraft are presented. The lift coefficient (C_L) is computed based on the True Air Speed and the Lift force as follows: $C_L = \frac{Lift}{\frac{1}{2} \cdot \rho \cdot S \cdot TAS^2}$, where TAS is the true air speed, ρ is density at flight test conditions and S is the wing area. The drag coefficient (C_D) is computed similarly but instead of the lift the drag force is used. Figure 5.9 and 5.10 show the lift and drag coefficient, respectively, as a function of the AoA.

The lift curve obtained from the flight tests showed a linear behaviour, this was expected since the AoA reached during the flight tests were only in the pre-stall condition. The best fit curve for the lift was:

$C_L = 0.0939\alpha + 0.0674$, with α in degrees. If it is assumed that the linear behaviour of the C_L remains up to the AoA=16°, the α_{stall} obtained from the CFD calculations, the maximum lift coefficient is 1.57. The zero lift angle is -0.7 °. The summarized results are shown in table 5.6.

The drag coefficient graph, figure 5.10, shows a approximately linear trend, which is different from the parabola observed in the CFD flow calculations. Due to the precision error of all the measurement equipments the parabolic trend of the drag coefficient was not observed. The drag coefficient was obtained by extrapolating the horse power of the engine from theoretical data sheets from the supplier, which does not account for all the interaction between the fluid and the components of the aircraft. Therefore, the values of the drag coefficient obtained from CFD could not be compared with the flight test data. Moreover, the mesh in the undercarriage was coarse and hence the flow calculations did not account for the separation inherent of bluff bodies, if modelled correctly this would result in a increase in the pressure drag. However, during flight that is very present, not only the undercarriage but also the fuselage itself, thus the drag coefficient obtained will account for an increase drag that was not accounted for in the CFD flow calculations. In addition, the propeller during flight increases the velocity of the flow on the upper surface on the wing thus increasing the induced drag and the flow remains attached longer for the same reason and it increases the skin friction drag. Ergo, the C_D could not be compared between the CFD and flight tests results. Nevertheless, one can state that the drag coefficient obtained from the RANS and DES flow calculations will be highly under predicted.

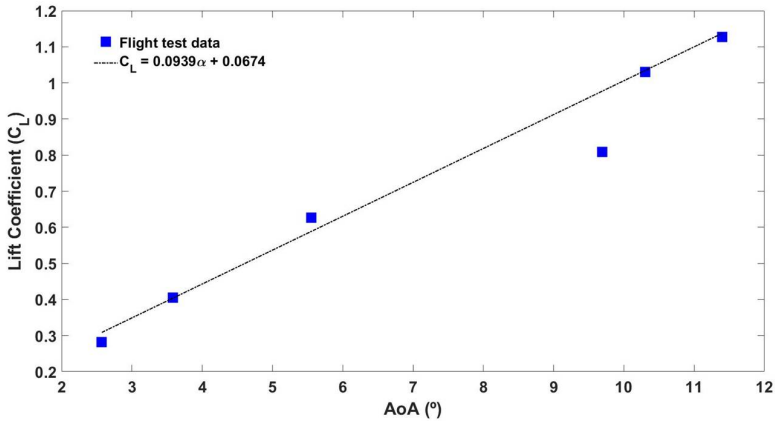

Figure 5.9: Lift Coefficient curve as a function of the AoA obtained from the flight tests.

Table 5.6: Lift and Drag coefficients obtained from the steady level flight test.

IAS (knots)	AoA (°)	C_L	C_D
120	2.57	0.282	0.052
100	3.58	0.405	0.084
80	5.55	0.627	0.130
70	9.69	0.809	0.164
62	10.3	1.031	0.1994
60	11.4	1.127	-

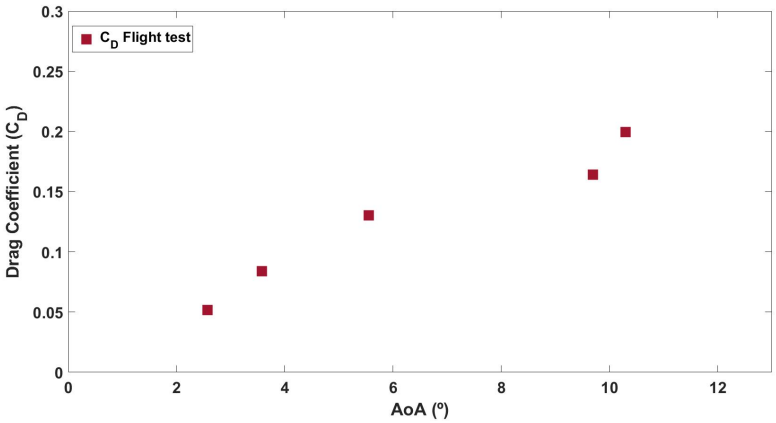

Figure 5.10: Drag Coefficient curve as a function of the AoA obtained from the flight tests.

The comparison between the CFD and flight test lift coefficient is shown in figure 5.11. The flight test lift coefficient, was computed with the lift curve presented above and the AoA studied in the CFD flow calculations, in order to have a more direct comparison. In table 5.7, the slope of the lift curve (a) and zero lift angle (a_0) are shown. In addition, the best fit curves are also presented. The steady RANS solutions have a lift curve slope that differs -10 % from the lift slope obtained from the flight tests and zero lift angle is 20% lower for the CFD calculations. This results in a general under prediction of the lift coefficient obtained from the CFD flow calculations, the deviation of the lift coefficient for both mathematical formulations is shown in table 5.8. In addition, for the DES results the lift coefficient is closer to the flight tests. This under prediction could be improved by implementing a propeller in the CFD calculations.

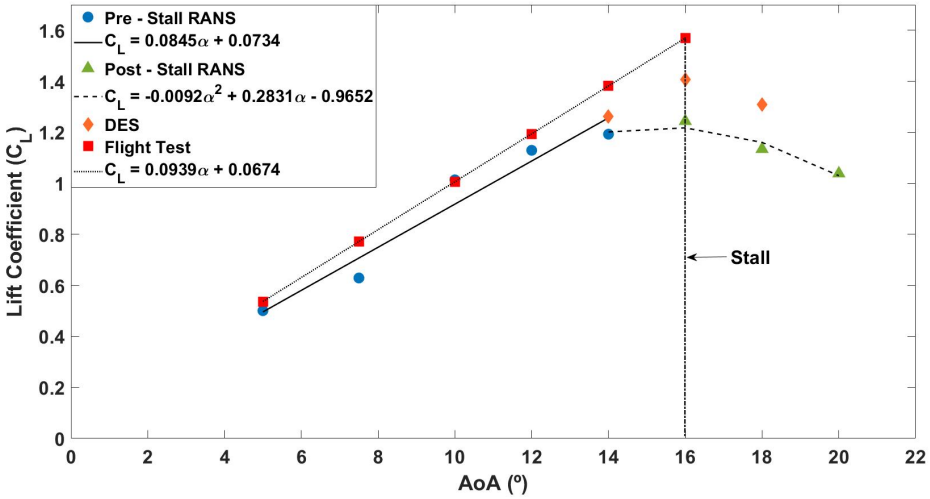

Figure 5.11: Comparison between the lift curve of the CFD and flight test results.

Table 5.7: Summary of the lift curves obtained from the CFD flow calculations and flight tests.

Data set	α_0	$a(C_L/^\circ)$	$\alpha_{stall}(^\circ)$	C_{Lmax}	Trendline equation
CFD Pre-Stall - RANS	-0.87	0.0845	-	-	$C_L = 0.0845\alpha + 0.0734$
CFD Post-Stall - RANS	-	-	16	1.24	$C_L = 0.014\alpha^2 - 0.0213\alpha + 0.185$
CFD - DES	-	-	16	1.40	-
Flight tests	-0.72	0.0939	16	1.57*	$C_L = 0.0939\alpha + 0.0674$

* Assuming a linear curve until the critical AoA = 16 °.

Table 5.8: Estimated relative deviation of the CFD flow calculations compared to the flight test results.

α	C_L-RANS	C_L-DES	C_L-Flight test	$\Delta_{rel\ RANS}$ (%)	$\Delta_{rel\ DES}$ (%)
5	0.51	-	0.54	-6.72	-
7.5	0.63	-	0.772	-18.4	-
10	1.02	-	1.006	-0.74	-
12	1.13	-	1.194	-5.41	-
14	1.19	1.26	1.382	-13.69	-8.8
16	1.24	1.40	1.57	-20.77	-10.2
18	1.13	1.31	-	-	-
20	1.04	-	-	-	-

In addition, a flight test that aimed at predicting the critical angle of attack was also performed, and its methodology is shown in section 4.2.3. The graph resultant from the post-processing of the data is shown in figure 5.12. The critical angle of attack obtained was 18°, two degrees higher than in the CFD results. This result was expected due to the lack due to the presence of a propeller in the flight tests, that has a destalling effect. The Slingsby α_{stall} had been previously computed by Hoff [9], while studying the spin of the Slingsby Firefly, and the same value was encountered.

The cells highlighted in blue represent the time between the start of the stall warning and the wing drop, this had a total duration of 7 seconds. The flow separation and buffet only begin after 3s, hence the buffet had a duration of 4s. Ultimately, in those 4s the AoA reached was 14, 15, 16 and 18°. From this information, two conclusions can be stated. The α_{stall} is 18° and the angles for which buffet occurs is between 14-18°.

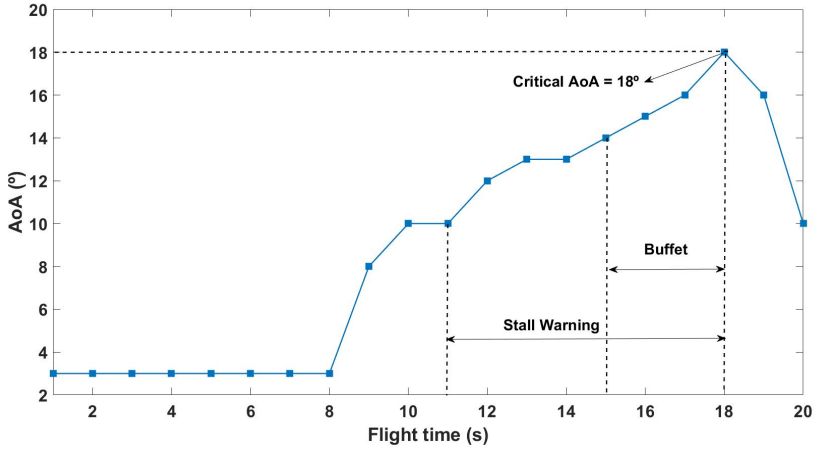

Time (s)	AoA(°)
11	10
12	12
13	12
14	13
15	14
16	15
17	16
18	18
19	16
20	10

Figure 5.12: AoA as a function of the flight time obtained from the stall angle of attack flight test.

5.2.2 Flow Visualization

The characterization of the flow separation pattern of the boundary layer on the upper surface of the wing was one of the goals to be met. In order to do so the CFD contours of the limiting streamlines and skin friction coefficient were computed. These were then qualitatively compared to the data gathered in the wool tufts flight tests.

Streamlines were used to visualise the boundary layer flow separation mechanism on the upper surface of the wing. They are the lines tangent to the shear-stress vector at the wall. They allow the detection of attached and separated flow which is highly important to understand how the boundary layer reacts to the increase of the AoA.

The Slingsby Firefly (see chapter 1) has a tapered wing with washout, i.e., the angle of incidence at the root is higher than at the tip. Due to the geometric features of the wing, it is expected that as the angle of attack is increased the flow begins to separate at the root due to its washout. Further increase of the AoA will result in an increase of flow separation in both spanwise and chordwise directions. The aerofoils used in the wing are both thick aerofoils hence a trailing-edge stall is present. This mean that the flow will separate first at the trailing-edge and move towards the leading-edge as the angle of attack increases. The flow separation mechanism described is observed in the streamline contours in figure 5.13, where the pre-stall condition is described.

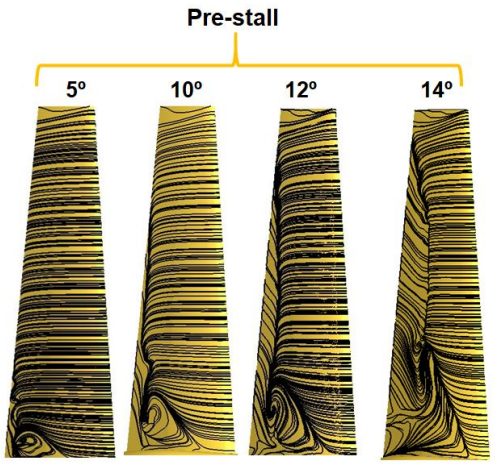

Figure 5.13: Streamlines of the flow in the upper surface of the wing for AoA: 5,10,12 and 14 °.

The aircraft will stall when about 50% of the wing's upper surface flow is separated resulting in a loss of lift. Figure 5.14 shows the streamlines for the critical angle of attack that was presented in section 5.2.1. The 16° limiting streamline contour shows that about 50% of the flow is separated (see figure 5.15). The flow separation area was calculated in order to confirm what was stated, the results are shown in the table in figure 5.15. The percentage of the total area correspondent to the boundary layer flow separation was 48.64 %, which means that the aircraft is stalled at this AoA.

Figure 5.14: Streamlines of the flow in the upper surface of the wing for AoA: 16 °.

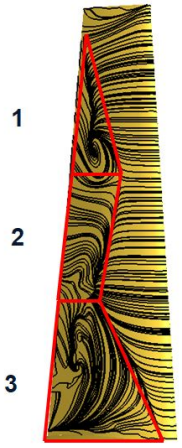

Region	Area (m^2)	Percentage of flow separation (%)
Wing Upper Surface	5.543	-
1	0.4546	8.2
2	0.6588	11.89
3	1.5823	28.55
Total flow separation		48.64

Figure 5.15: Percentage of the boundary flow separation of the upper surface of the wing for an AoA= 16 °.

In addition, the wing is unswept and due to the interaction between the shear layer that is generated close to the separation line and the wake that roll up in opposite directions, mushroom shaped cells appear just beyond stall, as explained in section 2.3.2. These flow patterns were observed in the streamline contour of the $AoA = 18°$ for three mesh densities: coarse, medium and fine, shown in figure 5.16. The cells are dependent on the aspect ratio of the wing, for the Slingsby aspect ratio of 9, about three cells should appear. In the coarse and medium mesh only a stall cell was observed, as the aircraft is only modelled half, in total there a two stall cells. The fine mesh presents in total four stall cells. However, the empirical correlation between the wing's aspect ratio and the number of stall cells do not account for the interaction with all the other components of the aircraft and were only performed in rectangular wings. This might explain the different numbers of stall cells observed from the CFD results presented.

Moreover, the negative pressure coefficient as a function of the normalized wing chord was obtained in three different wingspan locations for the mesh. The objective was to confirm that the limiting streamline contours are coherent with the pressure distribution found in the upper and lower surface of the wing. In figure 5.17, the schematic of the three different sections where the pressure distribution and

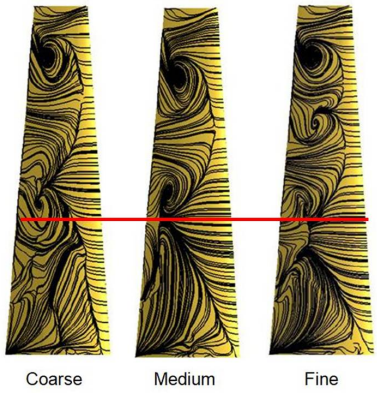

Figure 5.16: Streamlines of the flow in the upper surface of the wing for AoA: 18 °.

respective limiting streamline contour were analysed for the fine mesh are shown. It is observed that the section that has higher lift, i.e. higher pressure difference, is the section located at z = 2.5 m, which is in fact the section where the flow is attached up to a more extensive chord. The suction peak differs for the three different sections due to the wing washout, i.e., at the root the angle of attack of the wing is higher and at the tip it is lower. In fact, the suction peak is lower at the section located in the plane z = 1.5 m and higher at the plane z = 4 m which is close to the tip and has a lower AoA.

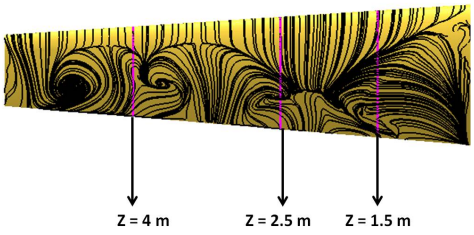

(a) Schematic of the different sections in the wing for which the pressure distributions were computed.

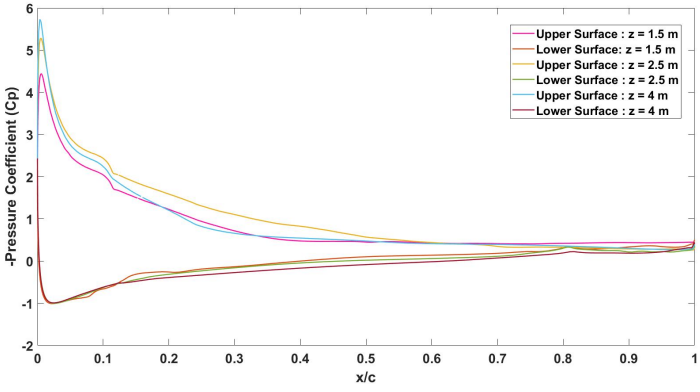

(b) Negative pressure coefficient as a function of the normalized chord at AoA = 18 ° in the planes z = 1.5, 2.5 and 4 meters

Figure 5.17: Pressure distribution of three different sections on the wing at an AoA = 18° and respective schematic.

As complement to streamline contours, contours of the skin friction coefficient were also analysed. The skin friction coefficient (C_f) is the non-dimensional shear-stress at the wall . For a finite wing the separation occurs no longer at point (as it happen for an aerofoil) but rather in a separation line. In the separation line the value of C_f is zero and when the flow is separated the skin friction coefficient is negative due to the presence of adverse pressure gradients. In order to observe where separation of the boundary layer occurred, contours of C_{fx} were obtained with the CFD-Post. The contours have the same scale.

In figure 5.18, the skin friction coefficient contours are shown for the range of angles of attack studied. The progression of the boundary layer separation is equivalent to the previous section, i.e., the C_f is zero at the wing root for lower α and it progresses both spanwise and chordwise as α is increased. At $\alpha = 16°$ the C_f is zero at approximately 50% of the upper surface of the wing. It is concluded, that the aircraft is stalled when 50 $\%$ of the boundary layer is separated.

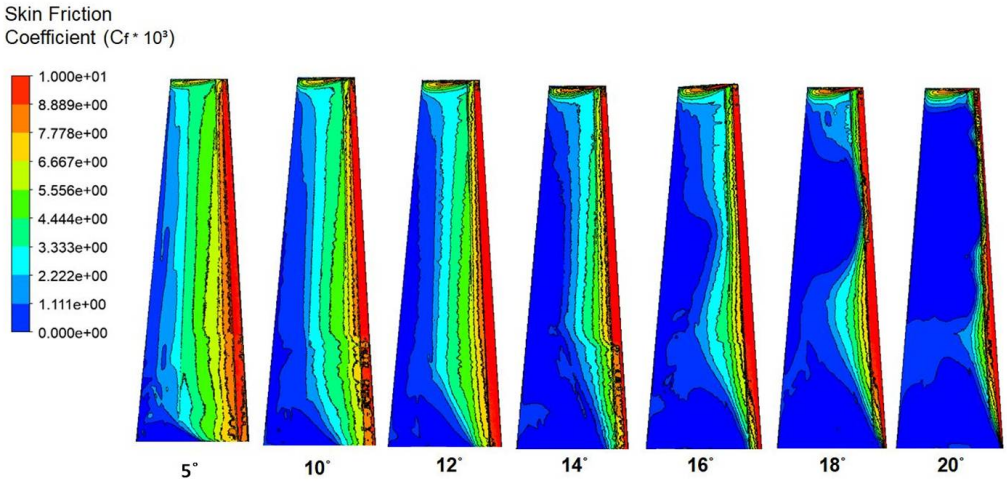

Figure 5.18: Skin Friction coefficient in the flow direction.

In order to evaluate the quality of the results obtained from the CFD flow calculations, the behaviour of wool tufts in the upper surface of the wing were monitored. As mention in section 4.2.4 the left wing of the Slingsby Firefly was covered by wool tufts of 15 cm length and 24 cm apart. The aircraft was stalled and the video imagery of the wool tufts were recorded. The flow begins to separate at the root after the stall warning is activated, however buffet only began after 4 seconds of stall warning. As the airspeed is reduce to the stall speed the AoA increases and the flow separation region follows a similar separation pattern as found in the limiting stramline contours in the CFD flow calculation.The separation progresses both spanwise and chordwise as expected for the same previous reasoning stated.

The behaviour of the wool tufts during the pre-stall and stall condition for the four seconds duration of buffet are shown in Appendix B.1. The images result from post-processing of the video recorded, the last image is just before the wing dropped and the aircraft stall is recovered before entering a spin.

Similar patterns, to the ones obtained from the CFD calculations, of the boundary layer separation were observed in the flight test. The stall cells visualization was not possible however, similar regions of attached and separated flow were observed. Although the same patterns occurred, their relative

localization was also verified. Figures 5.19, 5.20 and 5.21 show the comparison between the wool tufts flight test and the CFD limiting streamlines contours pattern and respective localization on the upper surface of the wing. It was observed that that the patterns of the flow separation and respective locus were similar between the numerical and experimental approach.

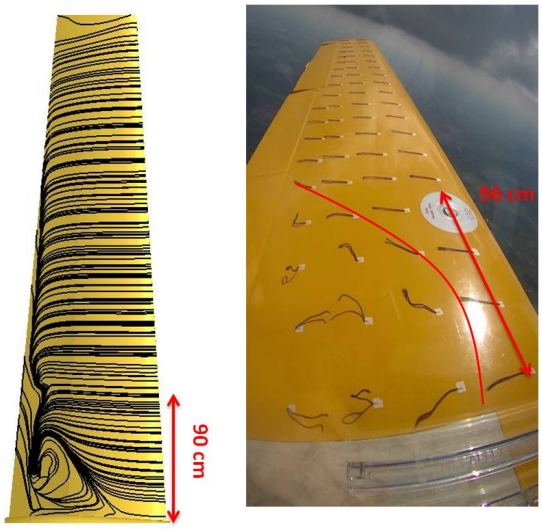

Figure 5.19: Flow visualisation of the flow with an AoA of 10 ° and equivalent flight test image.

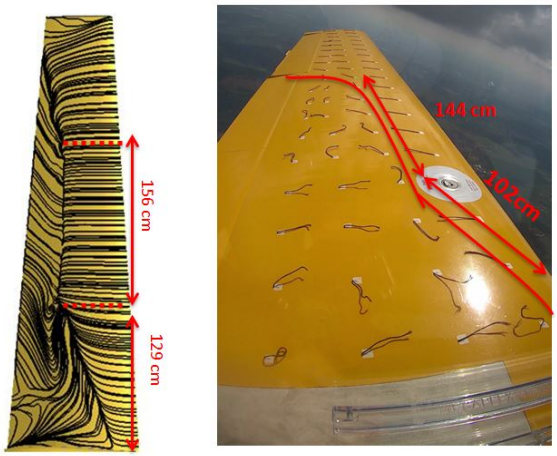

Figure 5.20: Flow visualisation of the flow with an AoA of 14 ° and equivalent flight test image.

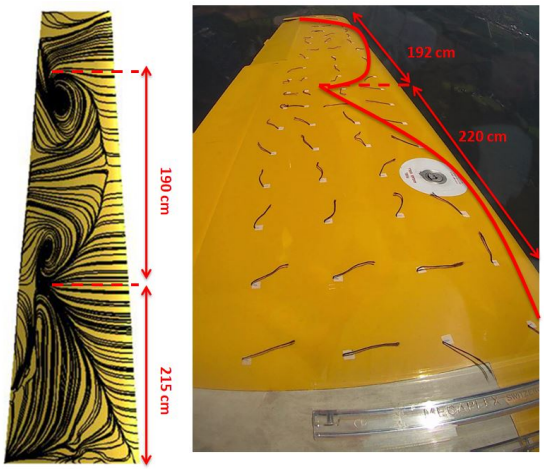

Figure 5.21: Flow visualisation of the flow with an AoA of 18 ° and equivalent flight test image.

5.2.3 Vortex Shedding Frequency

The hybrid RANS/LES model, DES with $k-\omega$ SST, was implemented after a converged RANS solution of the α=14, 16, 18° was obtained. Due to time concerns, there was a decision of only applying this model to the AoA where buffet occurred (AoA = 14, 16 and 18 °) in order to compare the vortex shedding frequency with the buffet frequency measured in the flight tests.

The frequency of the shed vortices (f_s) was computed at several probes in the wake of the wing, as previously shown in section 4.1.4. In addition, the lift coefficient was monitored. A Fast Fourier Transform was performed to transform the data that was in a time domain to a frequency domain. The mean value (DC component of the signal) of the quantities analysed was removed with the Matlab tool: *detrend*. This mean value would be represented as a peak at 0 Hz with an amplitude that corresponded to the mean value. Moreover, the amplitude was normalized in order to compare the results coherently.

The results obtained from the CFD calculations were compared with the buffet frequency of the aircraft when approaching stall. Buffet results from changes in pressure resulting in an airframe vibration, hence the reason for monitoring the static pressure (P_{static}) at several probes in the wing's wake. In the addition, the changes in pressure are responsible for variation on the lift force, since the pressure acts perpendicular to the wing's surface. During flight, buffet is the structure response to the periodic changes in lift. Hence, the buffet frequency ought to be similar to the frequency of the static pressure ($f_{P_{static}}$) wing's wake and the lift coefficient.

The FFT was applied to the static pressure for the probes monitored and to the lift coefficient of the three AoA studied. The time step used was 0.00067s which corresponds to a frequency of acquisition of 1472 Hz. The data presented are from four probes at different regions in the wake of the wing for the three AoA.

The author carefully chose four different probes situated at different regions in the wing's wake in order to capture the frequency of the vortex shedding at different locations. The probes chosen were P5, P10, P14 and P15 and are shown in figure 5.22.

(a) Front View.

(b) Lateral View.

Figure 5.22: Different views of the probes.

The FFT of the data of the probe 5 is shown in the graph 5.23, the remaining graphs are in Appendix B.2. The graphs shown have both 1472 and 50 Hz data in order to compare it with the flight tests, which had an acquisition frequency of 50 Hz.

It is observed that in the all of graphs a dominant peak exists which corresponds to the dominant shed structures frequency, i.e., the vortex shedding frequency. In addition, other smaller peaks at higher and lower frequencies were present. The several peaks found were expected due to the different length scales turbulent flow possess. Since the probes monitored were in the region where LES is activated (focus region), different frequencies ought to be captured. The lower frequency peaks occur due to the presence of large eddies (low frequencies) that are the biggest contributors for the turbulence kinetic energy and the higher frequency peaks the smaller eddies. For the same AoA the frequency remains unaltered in the different probes. Furthermore, an increase in the AoA results in a decrease in the f_{vs}. This tendency had been previously shown in a DNS study of a NACA 0012 in full stall by Rodríguez et.al [127]. The summary of the results is shown in table 5.9.

The lift coefficient was also monitored for the AoA studied and the gathered data is shown in figures 5.24, 5.25 and 5.26. The same trend was found with the increase of the AoA , i.e., an increase in the AoA resulted in a decrease in the frequency of the variation of the lift coefficient.

Table 5.9: Summary of the f_{vs} (Hz) of the probes: P_5, P_{10}, P_{14}, P_{15} and C_L for the AoA = 14, 16, 18 °.

AoA (°)	$f_{vs}P_5$	$f_{vs}P_{10}$	$f_{vs}P_{14}$	$f_{vs}P_{15}$	$f_{vs}C_L$
14	11.66	11.66	11.66	11.66	11.74
16	10.2	10.2	10.2	10.2	10.19
18	8.946	8.742	8.946	8.946	8.742

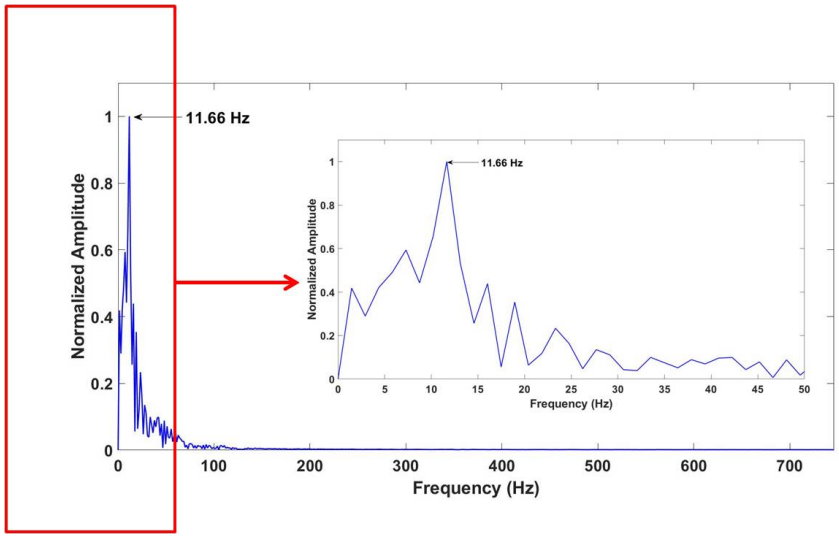

(a) **AoA = 14°**

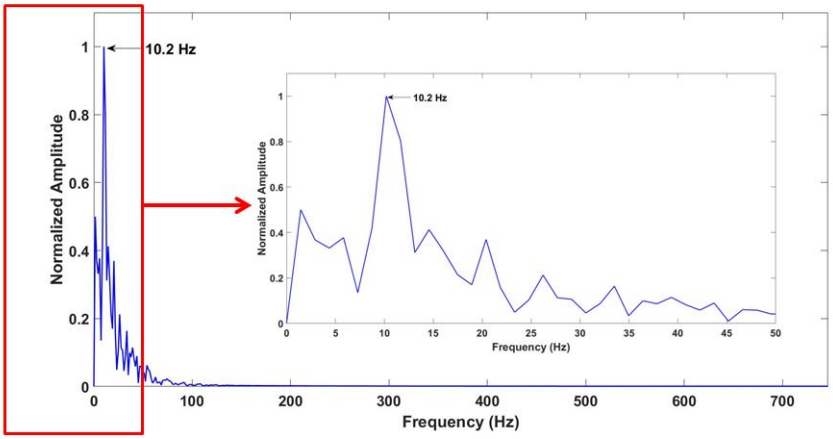

(b) **AoA = 16°**

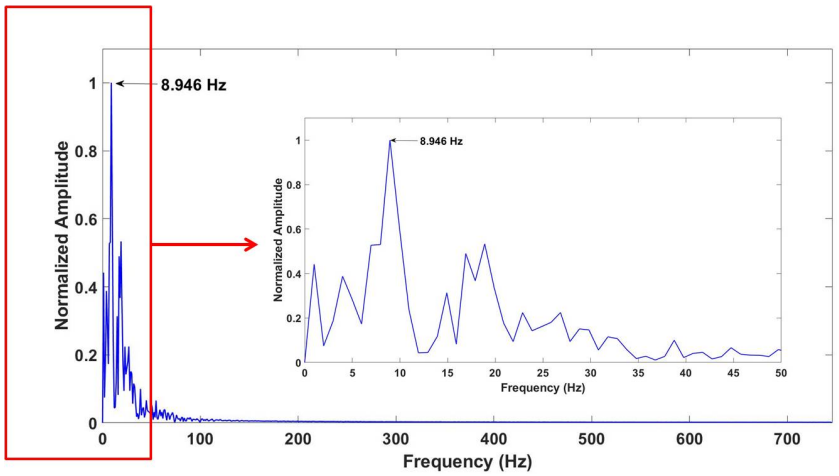

(c) **AoA = 18°**

Figure 5.23: FFT analysis of P_{static} at point P5 for the different AoA studied .

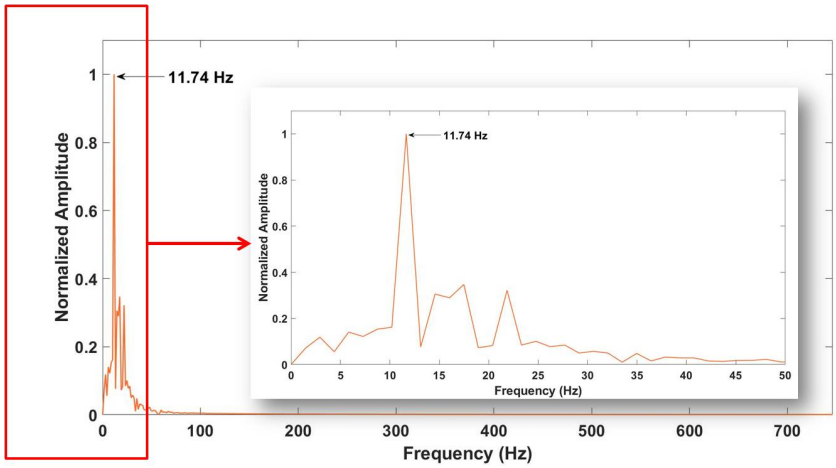

Figure 5.24: Fast Fourier Analysis of C_L for an AoA=14°.

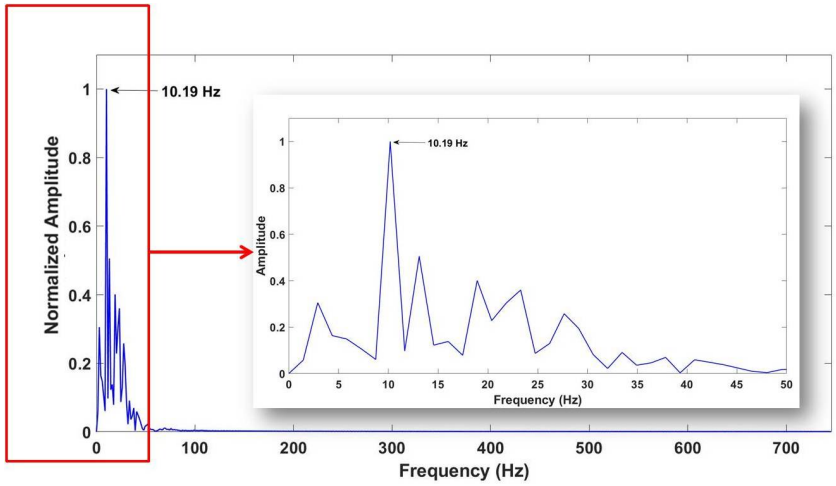

Figure 5.25: Fast Fourier Analysis of C_L for an AoA=16°.

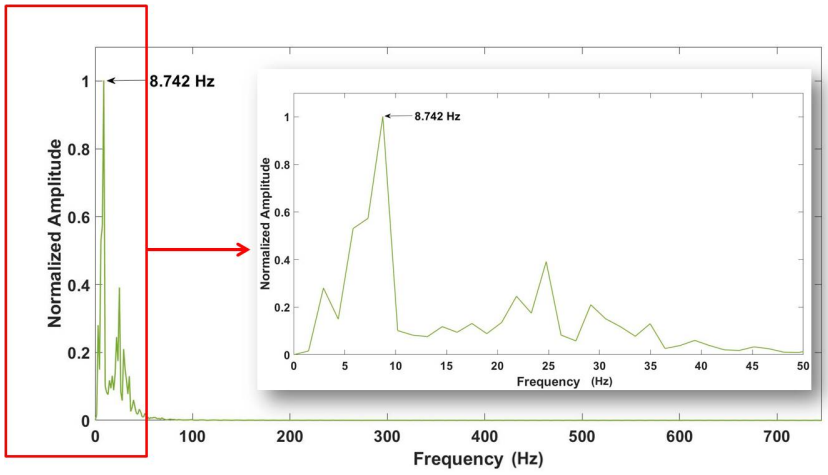

Figure 5.26: Fast Fourier Analysis of C_L for an AoA=18°.

In order to evaluate the quality of the previous results, the buffet frequency was measured in flight with accelerometers. The aim was to compare it with the shedding frequency obtained in the CFD flow calculations. The buffet had a duration of 4 seconds before the wing dropped, two stalls were performed and data was recorded for both. Those 4 seconds of data were analysed and a Fast Fourier Analysis was performed in order to obtain the buffet frequency. The acquisition frequency was 100 Hz and the amplitude was normalized.

The first second of the first stall performed in the Slingsby is shown in figure 5.27. The figure shows the signal and correspondent FFT of one second of data of the three second buffet. The dominant peak corresponds to a frequency of 11.76 Hz which represents the buffet frequency. Another peak is present and it engine frequency, which was computed from the RPM value.

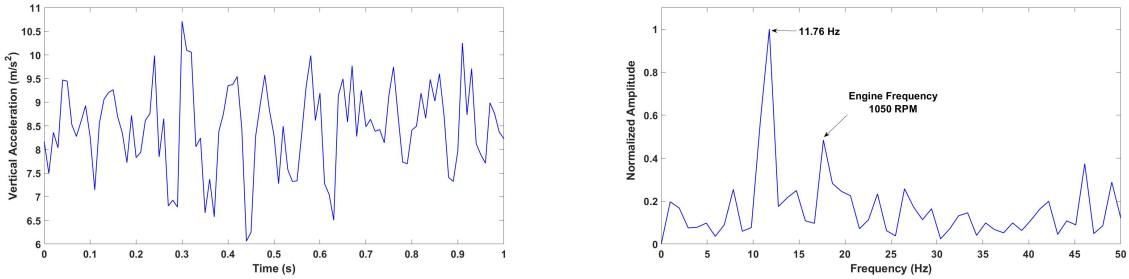

(a) Time signal of first second of stall (sensor n^{o}1)

(b) Fast Fourier Analysis of first second of stall (sensor n^{o}1) .

Figure 5.27: Sensor n^{o}1 stall data

A more detailed analysis was performed to the data from sensor n^o3, in order to verify if the increase in angle of attack would result in a decrease of the buffet frequency, as it was what was observed with the CFD flow calculations. In fact, that was observed and it is shown in figures 5.28, 5.29 and 5.30. The different peaks in the FFT are due to the signal noise from several vibration sources of the aircraft. A filter could be applied to eliminate the noise in the signal, however accurately applying a filter without damaging important data is a challenge and should be performed carefully. Due to time constraints, that was not possible but it is mentioned as a future improvement in chapter 6.

The AoA studies performed with CFD corresponded to the same AoA reached in the flight test (see section 5.2.1). Owing to this, the results obtained can be compared qualitatively and quantitatively. In table 5.10, the CFD and flight test results for the frequency of the vortex shedding and buffet, respectively, and its relative deviation are presented. In addition, the Strouhal number (St), based on the projected height, $h = \bar{c} \cdot sin(\alpha)$, was computed for the CFD and flight test results. The values of St varied from 0.1-0.115, which is typical for unswept wings with flow separation (S=0.1-0.2) according to Katz and Plotkin [128].

The relative deviation between the flight test and the monitored quantities is below 3% for all the conditions presented. Hence, considering all the simplifications in the CFD model and flight test errors, the results are promising.

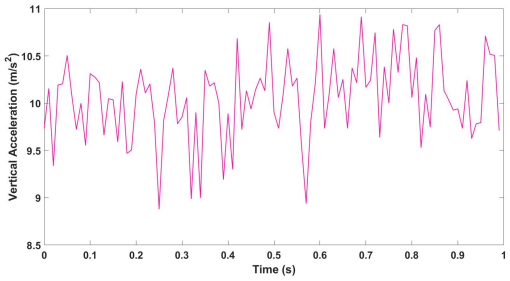

(a) Time signal of 1st second of stall (sensor n°3).

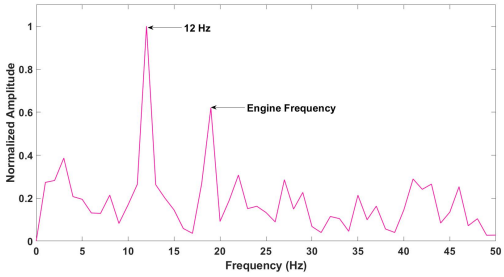

(b) Fast Fourier Analysis of 1st second of stall (sensor n°3).

Figure 5.28: Data correspondent to the 1st second of stall.

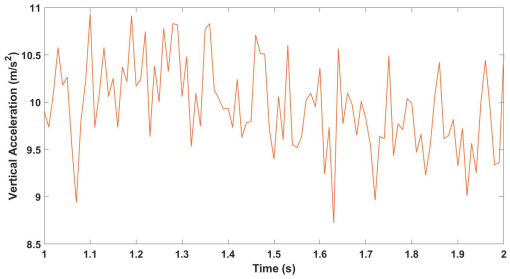

(a) Time signal of 2nd second of stall (sensor n°3).

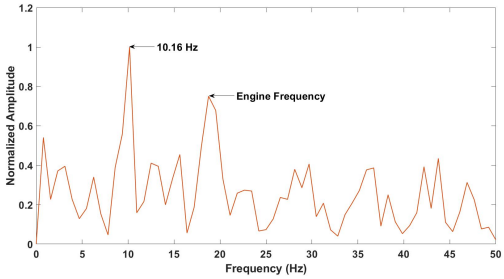

(b) Fast Fourier Analysis of 2nd second of stall (sensor n°3).

Figure 5.29: Data correspondent to the 2nd second of stall.

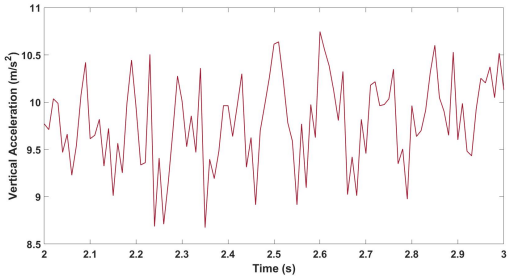

(a) Time signal of final second of stall (sensor n°3).

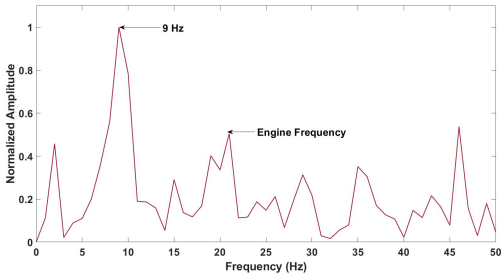

(b) Fast Fourier Analysis of final second of stall (sensor n°3).

Figure 5.30: Data correspondent to the final second of stall.

Table 5.10: Module of the relative deviation of P_{static} and C_L frequency.

AoA	$f_{Flight\ test}$ (Hz)	$f_{P_{static}}$ (Hz)	$\lvert\Delta_{rel}\rvert_{P_{static}}(\%)$	$f_{(C_L)}$	$\lvert\Delta_{rel}\rvert_{C_L}(\%)$	$St_{Flight\ test}$	$St_{P_{static}}$	St_{C_L}
14	12	11.66	2.83	11.74	2.17	0.115	0.111	0.106
16	10.16	10.2	0.39	10.19	0.3	0.111	0.105	0.105
18	9	8.946	0.6	8.742	2.87	0.110	0.103	0.10

Chapter 6

Conclusions

The thesis addresses the stall characteristics of a light aircraft, the Slingsby Firefly, more specifically the critical AoA and correspondent maximum lift coefficient, the patterns of the boundary layer flow separation on the upper surface of the wings for the pre and post stall conditions and finally the vortex shedding frequency that results in a vortex induced vibration, buffet. This last parameter is important from both an aerodynamic and structural point of view.

The above mentioned characteristics were computed numerically with the application of CFD. The mesh of half of the model of the Slingsby was computed with the commercial software ICEM CFD. The CFD flow calculations were performed with a steady RANS turbulence model $k-\omega$ SST and Detached-Eddy Simulation, with commercial solver ANSYS Fluent. The results obtained from the numerical calculations were qualitatively and quantitatively (with the relative deviation) evaluated with several flight tests performed.

Three different meshes with distinct densities (coarse, medium and fine mesh) were computed and their respective numerical calculation was performed for a Pre-Stall AoA = 12 $^\circ$ and a Post-Stall AoA = 18°. This was done in order to understand which mesh would be suitable to perform all the flow calculations based on the numerical and physical accuracy and the computational time required. The quantities monitored were both the lift and drag coefficient, the pressure distribution for three different section on the wing and the limiting streamlines contour for the AoA mentioned. Overall, the medium mesh presented the best physical accuracy with a computational time reduced compared to the fine mesh. Ultimately, the medium mesh density was applied to all the flow calculations.

The steady RANS flow calculations with the turbulence model $k-\omega$ SST were carried out for the AoA = 5, 7.5, 10, 12, 14, 16, 18 and 20 $^\circ$. The lift curve obtained showed that the pre-stall condition of the aircraft occurred up to the AoA = 14°. The pre-stall region had a linear behaviour, as it was expected. The best fit curve was: $C_L = 0.0845\alpha + 0.0734$, which gives a zero lift angle of -0.87 $^\circ$. The lift slope of the numerical simulations have a -6% deviation from the lifting-line theory curve. The lifting-line theory only accounts for the lift of a finite wing, whereas the CFD model has the influence of other components, hence the lift slope of the CFD results ought slightly different from the lifting line theory slope.

Due to the non-existence of the propeller, which augments lift over the section of the wing due

to the slipstream, in the CFD model, the lift coefficient in the pre-stall condition was under predicted when compared with the steady flight test, which had a linear curve with the following equation: $C_L = 0.0939\alpha + 0.0674$, giving a zero lift angle of -0.7 °. The post-stall region had a critical angle of attack of 16 ° and a maximum lift of 1.244. A flight test to obtain the critical angle of attack was performed and the value found was 18 °, which is two degrees higher in comparison with the CFD results due to the destalling effect of the propeller. The post-stall region had the highest deviation of the C_L, since close to the critical angle of attack the boundary layer flow on the upper surface of the wing is separated, which is an unsteady phenomenon that the steady RANS does not account for. Hence, the DES values of lift which account for the lift variations wee expected to give closer C_L results to reality, however the post-stall region was not accounted in the flight tests. The drag coefficient was also obtained from the CFD flow calculations. However due to the interaction of the different bluff bodies during flight, for instance the undercarriage and fuselage, which due to the mesh density used were not modelled accurately in the CFD model, the results could not be compared to the flight test results. Nevertheless, for a CFD model that lacks the propeller the lift curve slope and zero lift angle are in within a 10 % deviation, except for an angle of attack. Moreover, the application of DES for AoA close to the critical angle will ultimately give a good approximation of the lift coefficient. Hence, the steady RANS calculations can define the pre-stall condition of the aircraft and the DES flow calculation the post-stall condition.

The boundary layer flow separation patterns observed both with CFD and the wool tufts visualisation technique were similar. The patterns encountered were the same and their relative location in the wing as well, this means that the boundary layer in the CFD mesh was modelled correctly. Thus the importance of modelling the three regions of the turbulent boundary layer, viscous layer, buffer layer and log-law region. In an early design stage of an aircraft, where unsteady solutions of the flow are not possible, steady RANS flow calculations using the turbulence model $k - \omega$ SST can be performed in order to understand how the flow separation propagates in the wing surface. These findings are important because the flight tests are often costly and performed in a later design stage, hence at a low computational cost the flow separation mechanism can be performed.

The DES performed in converged solutions of the stall and post-stall conditions proved to predict the vortex shedding frequency accurately when compared to the buffet frequency measured during flight. Moreover, the increase of the AoA resulted in a decrease of the vortex shedding frequency for both the CFD and flight tests results. This is important in order to understand the limitations of the structure of the aircraft due to the vibrations induce by the buffet.

The work developed allows for the characterization of important stall characteristics, with a medium mesh density and CFD widely used turbulence model and a recent hybrid RANS/RANS mathematical model, that are usually only possible to obtain with flight and wind tunnel testing. This allows for a better understanding of the stall characteristics of an aircraft, thus reducing the costs of later alterations on the design when only flight tests were available. Moreover, the first stage of a spin is a stalled aircraft hence the present results can aid the description of the spin of the Slingsby Firefly.

6.1 Future Work

Though, the objectives of the present thesis were met and the results are promising for a first attempt, the author suggests some improvements that would ultimately produce better results overall.

Due to the results obtained with the steady RANS flow calculations, which under predict the lift coefficient, the aircraft model should in the future have the propeller modelled and the remaining aircraft components accurately represented by a finer mesh. This would conclude if the under-prediction of the lift coefficient was due to the turbulence model chosen, the lack of propeller or both. In addition, it would improve the results and the understanding of how the turbulence model is able to characterize highly separated flows. Moreover, the mesh density should be refined in order to have an accurate representation of the bluff bodies drag, thus giving a better prediction of drag.

An adaptive mesh technique should be implemented in the DES calculations. This could decrease the mesh density and optimize the focus region ergo reducing the computation cost and time. In addition, it would be beneficial to perform DES in all the angles of attack studied (if possible even more AoA) since there is flow separation before the critical angle of attack is achieved. In the present work,a constant time step and focus region density was used. It is advised to apply different time steps and mesh densities in the focus region in order to understand how sensitive is the solution to changes in these two parameters.

The flight tests performed should be repeated and with a bigger flight envelope, the errors associated with the tests should be computed. The measurement of angles during flight should be accomplish with another method than the use of inclinometer, which represents a big source of error. The flow visualisation technique using wool tufts should be repeated but with slightly smaller length in order to capture more patterns of the boundary layer separation in the upper surface of the wing. It would also be beneficial to perform oil flow visualization in order to further evaluate the CFD results. In addition, due to the noisy nature of the signal recorded by the accelerometers, filters should be applied to the signal.

Bibliography

[1] J. Chambers and H. P. Stough. Summary of NASA Stall/Spin research for general aviation configurations. In *AIAA General Aviation Technology Conference. Anaheim, CA, 29th September-1st October 1986.*, volume AIAA-86-25, Reston, VA. AIAA, AIAA-86-2597.

[2] V. de Brederode. *Aerodinâmica Incompressícel:Fundamentos*. IST Press, Lisboa, 1st edition, 2014. ISBN 978-989-8481-32-0.

[3] M. A. Mcveigh and E. Kisielowski. A design summary of stall chracteristics of straight wing aircraft. Technical report, NASA, Washington D.C, June 1971.

[4] D. McLean. *Understanding Aerodynamics - Arguing from the real physics*. John Wiley & Sons Ltd, 2013.

[5] E. Tinoco. The changing role of computational fluid dynamics in aircraft development. In *16th AIAA Applied Aerodynamics Conference, Albuquerque,NM,U.S.A., 15 - 18 June 1998*, Reston, VA. AIAA: AIAA-98-2512.

[6] Lycoming. Aeio-540-d4a5. Available at:https://www.lycoming.com/node/17434. Date acessed: 19 September 2019.

[7] Slingsby Firefly T67M260 . Available at:https://www.ukspacefacilities.stfc.ac.uk/Pages/Cranfield-University- Date acessed: 14 May 2019.

[8] S. A. Ltd. *Pilot's Operating Handbook: Firefly T67M260*. Ings Lane, Kikbymoorside, 1st edition, September 1996.

[9] R. Hoff. *The Aeroplane Spin Motion and an Investigation into Factors Affecting The Aeroplane Spin*. Phd, Brunel University London, 2017.

[10] B. Melvill Jones. Stalling. *The Journal of the Royal Aeronautical Society*, 38(285):753–770, 1934.

[11] Flightglobal. Aviation history 1939. Available at:https://www.flightglobal.com/pdfarchive/view/1939/1939 Date acessed: 09 May 2019.

[12] A. I. Neihouse. Tail-Design Requirements for Satisfactory Spin Recovery for Personal-Owner-Type Light Airplanes. *NACA TN 1329*, 1947.

[13] T. Kerr. A Criterion for the Prediction of the Recovery Characteristics of Spinning Aircraft. In *TN No. Aero 2251*, Farnborough, U.K., 1953.

[14] O. Seidman and C. J. Donlan. An Approximate spin design criterion for monoplanes, NACA-TN-711. Langley Field, VA, United States, 1939. National Advisory Committee for Aeronautics. Langley Aeronautical Lab.

[15] J. Bowman. Summary of spin technology as related to light general-aviation airplanes. National Advisory Committee for Aeronautics., 1971.

[16] R. S. Hultberg, B. , S. James, and C. A. Martin. Measurements of pressures on the tail and aft fuselage of an airplane model during rotary motions at spin attitudes. 1988.

[17] A. Broeren and M. B. Bragg. Low-frequency flowfield unsteadiness during airfoil stall and the influence of stall type. *16th AIAA Applied Aerodynamics Conference, 15 June 1998 - 18 June 1998, Albuquerque,NM,U.S.A.*

[18] R. Radespiel, D. Francois, D. Hoppmann, S. Klein, P. Scholz, and et al. Simulation of Wing and Nacelle Stall. *54th AIAA Aerospace Sciences Meeting, 4-8 January 2016, San Diego, California, USA.*

[19] B. A. Kish, M. Wilde, R. Kimberlin, I. Silver, E. Kolano, R. Schaller, D. Sizoo, and D. Webber. Stall characteristics and trim changes of six general aviation aircraft. 06 2018. doi: 10.2514/6.2018-2922.

[20] G. B. Gratton, R. I. Hoff, A. Rahman, C. Harbour, S. Williams, and M. Bromfield. Evaluating a set of stall recovery actions for single engine light aeroplanes. *The Aeronautical Journal (1968)*, 118 (1203):461–484, 2014.

[21] P. J. Bolds-Moorehead, V. G. Chaney, T. Lutz, and S. Vaux. Stalling transport aircraft. *The Aeronautical Journal (1968)*, 117(1198):1183–1206, 2013.

[22] E. Cichocka. Research on light aircraft spinning properties. *Aircraft Engineering and Aerospace Technology*, 89(5):730–746, 2017.

[23] C. Bennett, N. Lawson, J. Gautrey, and A. Cooke. The aircraft spin - a mathematical approach and comparison to flight test. In *AIAA Flight Testing Conference, 5-9 June 2017,Denver, Colorado.*, Reston, VA, 2017. AIAA: AIAA 2017-3652.

[24] R. I. Hoff and G. B. Gratton. Spin induced aerodynamic flow conditions on full-scale aeroplane wing and horizontal tail surfaces. *The Aeronautical Journal*, 117(1198):1207–1231, 2013.

[25] C. Bennett and N. Lawson. On the development of flight-test equipment in relation to the aircraft spin. *Progress in Aerospace Sciences*, 102:47 – 59, 2018.

[26] R. Hankers, F. Pätzold, T. Rausch, R. Kickert, M. Cremer, and J. Troelsen. EASA.2008/03: Safety Aspects of Light Aircraft Spin Resistance Concept. Technical report, 2009.

[27] G. A. S. Council. A Study of Fatal Stall or Spin Accidents to UK Registered Light Aeroplanes 1980 to 2008. Available at: http://peter-ftp.co.uk/aviation/misc-euroga/2018-Gasco-Spin-Final Proof Approved Version.pdf. Date acessed: 15 September 2019.

[28] A. A. S. Institute. Stall and Spin accidents: keep the wings flying., 2017.

[29] P. Swatton. *The Principles of Flight for Pilots*. John Wiley & Sons Ltd, West Sussex,UK, 2011.

[30] D. Stinton. *The Design of the Aeroplane*. Blackwell Science Ltd, 2nd edition.

[31] D. Stinton. *Flying qualities and flight testing of the Aeroplane*. Blackwell Science Ltd, 1996.

[32] A.C.Kermode. *Mechanics of Flight*. Pearson Education Limited, 12th edition, 2013.

[33] R. Kimberlin. *Flight Testing of Fixed-Wing Aircraft*. American Institute of Aeronautics and Astronautics, Inc., Reston, VA, 2003.

[34] G. McCulloug and D. Gault. NACA/TN-2502: Examples of three representative types of airfoil-section stall at low speed. Technical report, National Advisory Committee for Aeronautics, 1951.

[35] ESDU. The low-speed stalling characteristics of aerodynamically smooth aerofoils, 1966. ESDU 66034.

[36] K. Mulleners and M. Rütten. Analysis of intermittent trailing edge vortex shedding using recurrence plots. In *18th International Symposium on the Applications of Laser and Imaging Techniques to Fluid Mechanics, Lisbon, Portugal, July 4-7 2016.*, 2016.

[37] J. Lumley and A. M. Yaglom. A century of turbulence. *Flow, Turbulence and Combustion*, 66: 241–286, 05 2001.

[38] M. Gad-el Hak. *Flow Control: Passive, Active, and Reactive Flow Management*. Cambridge University Press, 2000.

[39] T. Mullin. Turbulent times for fluids. *New Scientist.*, 1989.

[40] I. Eames and J.-B. Flor. New developments in understanding interfacial processes in turbulent flows. *Philosophical transactions. Series A, Mathematical, physical, and engineering sciences*, 369:702–5, 02 2011.

[41] O. Reynolds. An experimental investigation of the circumstances which determine whether the motion of water shall be direct or sinuous, and of the law of resistance in parallel channels. *Philosophical Transactions of the Royal Society of London*, 174:935–982, 1883.

[42] J. Hinze. *Turbulence*. McGraw-Hill, second edition, 1975.

[43] T. Cebeci and A. M. O. Smith. *Analysis of Turbulent Boundary Layers,*. Ser. in Appl. Math & Mech. Academic Press, 1974.

[44] D. Wilcox. *Turbulence Modeling for CFD*. DCW Industried,Inc., California, 3rd edition, 2006.

[45] A. Tsinober. *An Informal Introduction to Turbulence*. Springer-Verlag New York Inc., New York, NY, United States, 2002.

[46] A. Winkelmann, J. Barlow, J. Saini, J. Anderson, and E. JONES. The effects of leading edge modifications on the post-stall characteristics of wings. In *18th Aerospace Sciences Meeting, Pasadena,CA,U.S.A, 14 - 16 January 1980.*

[47] A. E. Winkelmann. An experimental study of separated flow on a finite wing. In *7th Atmospheric Flight Mechanics Conference, Albuquerque,NM,U.S.A, 19 - 21 August 1981*, .

[48] A. E. Winkelman and J. B. Barlow. Flowfield model for a rectangular planform wing beyond stall. *AIAA Journal*, 18(8):1006–1008, 1980.

[49] A. E. Winkelmann. Some observations of separated flow on finite wings. In *20th Aerospace Sciences Meeting, Orlando,FL,U.S.A., 11-14 January 1982*, .

[50] D. Weihs and J. Katz. Cellular patterns in poststall flow over unswept wings. *AIAA Journal*, 21: 1757–1759, 12 1983.

[51] S. Crow. Stability theory for a pair of trailing vortices. *AIAA Journal*, 8(12), 1970.

[52] A. Winkelman and J. Barlow. Flowfield Model for a Rectangular Planform Wing beyond Stall. *AIAA Journal*, (8):1006–1008.

[53] E. F. Toro. *Riemann Solvers and Numerical Methods for Fluid Dynamics : A Practical Introduction.* Springer, Berlin, Heidelberg, 3rd edition, 2009.

[54] L. Richardson. The Approximate Arithmetical Solution by Finite Differences of Physical Problems Involving Differential Equations, with an Application to the Stresses in a Masonry Dam. In *Trans. R. Soc. London*, volume 210, pages 307–357, 1910.

[55] R. Courant, K. Friedrichs, and H. Lewy. Über die partiellen differenzengleichungen der mathematischen physik. *Mathematische Annalen*, 100(1):32–74, Dec 1928.

[56] J. D. Anderson. *A History of Aerodynamics and Its Impact of Flying Machines*. Cambridge Aerospace Series, 8. Cambridge University Press, Cambridge, 1997.

[57] B. Riemann. Über die fortpflanzung ebener luftwellen von endlicher schwingungsweite. *Abhandlungen der Königlichen Gesellschaft der Wissenschaften zu Göttingen*, 8, 01 1892.

[58] A. Thom. The flow past circular cylinder at low speeds. In *Proc. R. Soc. Lond*, volume 141 of *Series A*, pages 651–669, 1933.

[59] F. H. Harlow. LADC-5288: The particle-in-cell method for numerical solution of problems in fluid dynamics. Technical report, US Atomic Energy Commission (AEC), 1962.

[60] J. Shang. Three decades of accomplishments in computational fluid dynamics. *Progress in Aerospace Sciences*, 40(3):173 – 197, 2004.

[61] T. Baker. Mesh generation for the computation of flowfields over complex aerodynamic shapes. *Computers & Mathematics with Applications.*, 24(5-6):103–127, 1992.

[62] W. K. Anderson, R. D. Rausch, and D. L. Bonhaus. Implicit/Multigrid Algorithms for Incompressible Turbulent Flows on Unstructured Grids. *Journal of Computational Physics.*, 128(2):391–408, 1996.

[63] T. Barth and D. Jespersen. The design and application of upwind schemes on unstructured meshes. In *27th Aerospace Sciences Meeting, Reno, Nevada, 9-12 January 1989.*, Reston, VA, 1989. AIAA.

[64] T. Barth. Numerical aspects of computing high Reynolds number flows on unstructured meshes. In *29th Aerospace Sciences Meeting, Reno, Nevada, 7-10 January 1991.*, Reston, VA, 1991. AIAA.

[65] M. A. Yerry and M. S. Shephard. Automatic three-dimensional mesh generation by the modified-octree technique. *International Journal for Numerical Methods in Engineering*, 20(11):1965–1990, 1984.

[66] J. C. Cavendish, D. Field, and W. H. Frey. An approach to automatic three-dimensional mesh generation. *International Journal for Numerical Methods in Engineering*, 21:329 – 347, 02 1985.

[67] D. F. Watson. Computing the n-dimensional Delaunay tessellation with application to Voronoi polytopes. *The Computer Journal*, 24(2):167–172, 01 1981.

[68] C. Shaw. *Using Computational Fluid Dynamics*. Prentice Hall International (UK), Hemel Hempstead, 1992.

[69] J. Nelson. A triangulation algorithm for arbitrary planar domains. *Applied Mathematical Modelling*, 2(3):151 – 159, 1978.

[70] S. Lo. A new generation scheme for arbitrary planar domains. *International Journal for Numerical Methods in Engineering*, 21:1403 – 1426, 08 1985.

[71] M. L. Merriam. An efficient advancing front algorithm for Delaunay triangulation. In *Aerospace Sciences Meeting, 29th, Reno, NV, 7-10 January 1991*, Reston, VA. AIAA.

[72] P. Spalart. Strategies for turbulence modelling and simulations. *International Journal of Heat and Fluid Flow*, 21(3):252–263, 2000.

[73] F. Roelofs and A. Shams. 6 - cfd—introduction. In F. Roelofs, editor, *Thermal Hydraulics Aspects of Liquid Metal Cooled Nuclear Reactors*, pages 213 – 218. Woodhead Publishing, 2019.

[74] Large-eddy simulation: achievements and challenges. *Progress in Aerospace Sciences*, 35(4): 335 – 362, 1999.

[75] R. Nichols and C. Nelson. Applications of Hybrid RANS/LES Turbulence Models. In *41st Aerospace Sciences Meeting and Exhibit, Reno, Nevada, January 6-9, 2003*, Reston, VA. AIAA: AIAA 2003-0083.

[76] P. Spalart. Young-person's guide to detached eddy simulation grids. Technical report, NASA, July 2001.

[77] P. Spalart, W. Jou, M. Strelets, and S. Allmaras. Comments on the Feasibility of LES for Wings, and on a Hybrid RANS/LES Approach. In *International conference; 1st, Advances in DNS/LES: Direct numerical simulation and large eddy simulation; 1997; Ruston; LA*, pages 137–148. Greyden Press, 1997.

[78] F. Menter. Zonal two-equation k-w turbulence model for aerodynamic flows. In *23rd Fluid Dynamics, Plasmadynamics, and Lasers Conference, Orlando,FL,U.S.A., 06 - 09 July 1993*, Reston, VA, 1993. AIAA:AIAA-93-2906.

[79] F. Menter. Two-equation eddy-viscosity turbulence models for engineering applications. *AIAA Journal*, 32(8):1598–1605, 1994.

[80] F. Menter, M. Kuntz, and R. Langtry. Ten Years of Industrial Experience with the SST Turbulence Model. *Heat and Mass Transfer*, 4, 2003.

[81] J. Forsythe, W. Strang, and K. Hoffmann. Validation of several reynolds-averaged turbulence models in a 3-d unstructured grid code. In *Fluids 2000 Conference and Exhibit, Denver, CO, U.S.A, 19-22 June 2000*, 06 2000.

[82] D. Zhang. Comparison of various turbulence models for unsteady flow around a finite circular cylinder at re =20000. *Journal of Physics: Conference Series*, 910:012027, 10 2017.

[83] P. R. Spalart. Detached-eddy simulation. *Annual Review of Fluid Mechanics*, 41(1):181–202, 2009.

[84] T. Nishino, J. Roberts, and X. Zhang. Unsteady rans and detached-eddy simulations of flow around a circular cylinder in ground effect. *Journal of Fluids and Structures*, 24(1):18 – 33, 2008.

[85] M. Shur, P. R. Spalart, K. D. Squires, M. Strelets, and A. Travin. Three-dimensionality in reynolds-averaged navier-stokes solutions around two-dimensional geometries. *AIAA Journal*, 43(6):1230–1242, 2005.

[86] M. Strelets. Detached Eddy Simulation of Massively Separated Flows. In *Conference: 39th AIAA Fluid Dynamics Conference and Exhibit, Reno, NV, U.S.A., 08 - 11 January 2001*, 2001.

[87] J. R. Forsythe and S. H. Woodson. Unsteady cfd calculations of abrupt wing stall using detached-eddy simulation. *Journal of Aircraft - J AIRCRAFT*, 42:606–616, 05 2005. doi: 10.2514/1.2934.

[88] J. Forsythe, K. Squires, S. Morton, W. Strang, K. Wurtzler, R. Tomaro, M. Grismer, and P. Spalart. Progress on Detached-Eddy Simulation of Massively Separated Flows. In *40th AIAA Aerospace Sciences Meeting & Exhibit, 14 January 2002 - 17 January 2002, Reno,NV,U.S.A.*

[89] F. Liu and D. Cokljat. DES of turbulent flow over an airfoil at high incidence. In *40th AIAA Aerospace Sciences Meeting & Exhibit, 14 January 2002 - 17 January 2002, Reno,NV,U.S.A.*, Reston, VA, 2002. AIAA: AIAA 2002-0590.

[90] J. Forsythe, R. Cummings, and S. Morton. Detached-Eddy Simulation of Slat and Flap Aerodynamics for a High-Lift Wing. In *42nd Aerospace Sciences Meeting, 5-8 January 2004 Reno, Nevada*, Reston, VA, 2004. AIAA, AIAA-2004-1233.

[91] A. Travin, M. Shur, M. Strelets, and P. Spalart. *Physical and Numerical Upgrades in the Detached-Eddy Simulation of Complex Turbulent Flows*, volume 65, pages 239–254. 01 2004.

[92] S. Pope. *Turbulent Flows*. Cambridge University Press, 2000.

[93] J. Boussinesq. Essai sur la théorie des eaux courantes. Technical report, Académie des Sciences, 1877.

[94] ANSYS. Ansys fluent theory guide. 275 Technology Drive Canonsburg, PA 15317, November 2013.

[95] A. Travin, M. Shur, M. Strelets, and P. Spalart. Detached-eddy simulations past a circular cylinder. *Flow Turbulence and Combustion*, 63(1-4):293–313, 01 2000.

[96] P. Spalart, S. Deck, M. Shur, K. Squires, M. Strelets, and A. Travin. A new version of detached eddy simulation, resistant to ambiguous grid densities. *Theoretical and Computational Fluid Dynamics*, 20:181–195, 2006.

[97] M. L. Shur, P. R. Spalart, M. K. Strelets, and A. K. Travin. A hybrid rans-les approach with delayed-des and wall-modelled les capabilities. *International Journal of Heat and Fluid Flow*, 29(6):1638 – 1649, 2008.

[98] A. Travin, M. Shur, M. Strelets, and P. Spalart. *Physical and Numerical Upgrades in the Detached-Eddy Simulation of Complex Turbulent Flows*, volume 65, pages 239–254. 01 2004.

[99] K. Bauer. CFD investigation into the spinning of the slingsby aerobatic aircraft. Msc thesis, Cranfield University, 2018.

[100] N. Lawson, N. Salmon, J. Gautrey, and R. Bailey. Comparison of flight test data with a computational fluid dynamics model of a scottish aviation bulldog aircraft. *Aeronautical Journal*, 117(1198), December 2003.

[101] C. Bennett, N. Lawson, J. Gautrey, and A. Cooke. Cfd simulation of flow around angle of attack and sideslip angle vanes on a bae jetstream 3102 – part 1. *Aerospace Science and Technology*, 68:561 – 576, 2017.

[102] N. Lawson, H. Jacques, J. Gautrey, A. Cooke, J. Holt, and K. Garry. Jetstream 31 national flying laboratory: Lift and drag measurement and modelling. *AerospaceScienceandTechnology*, 60: 84–95, 2017.

[103] L. Casadei, L. Könözsy, and N. J. Lawson. Unsteady detached-eddy simulation (des) of the jetstream 31 aircraft in one engine inoperative (oei) condition with propeller modelling. *Aerospace Science and Technology*, 91:287 – 300.

[104] N. Lawson. Ansys fluent user guide - 3d cfd solutions. National Flying Laboratory Centre, Cranfield Univerity, 2017.

[105] C. Bennett, N. Lawson, J. Gautrey, and A. Cooke. Cfd simulation of flow around angle of attack and sideslip angle vanes on a bae jetstream 3102 – part 2. *Aerospace Science and Technology*, 68:577 – 587, 2017.

[106] S. Morton, J. Forsythe, K. Squires, and R. Cummings. Detached-Eddy Simulations of Full Aircraft Experiencing Massively Separated Flows. In *The 5th Asian Computational Fluid Dynamics Conference, Busan, Korea, 27-30 October, 2003*, .

[107] M. Schultz, J. Finlay, M. Callow, and J. Callow. Three models to relate detachment of low form fouling at laboratory and ship scale. *Biofouling*, 19 Suppl:17–26, 05 2003.

[108] S. A. Morton, J. R. Forsythe, K. D. Squires, and K. E. Wurtzler. Assessment of Unstructured Grids for Detached- Eddy Simulation of High Reynolds Number Separated Flows. In *The 8th International Conference Numerical Grid Generation in Computational Field Simulations*, pages 571–586, Birmingham, AL, . International Society for Grid Generation.

[109] P. Tisovská, P. Peukert, and J. Kolář. Verification of ansys fluent and openfoam cfd platforms for prediction of impact flow. *EPJ Web of Conferences*, 143, 01 2017.

[110] T. Frank. A Database of ANSYS Fluid Solver Verification & Validation Tests based on ANSYS EKM. In *ANSYS Conference & 31. CADFEM Users Meeting, Rosengarten Kongresszentrum, Mannheim, 19-21 June 2013*, 06 .

[111] A. Rocha. Assessment of grid convergence properties for the calculation of the flow around the kvlcc2 tanker in unstructured grids. Master's thesis, Instituto Superior Técnico, 2017.

[112] L. Mangani, W. Sanz, and M. Darwish. Comparing the performance and accuracy of a pressure based and a density-based coupled solver. In *16th International Symposium on Transport Phenomena and Dynamics of Rotating Machinery, 10-15 April 2016, Honolulu, United States.*

[113] Y.-H. Choi and C. Merkle. The application of preconditioning in viscous flows. *Journal of Computational Physics*, 105(2):207 – 223, 1993.

[114] A. Miettinen and T. Siikonen. Application of pressure- and density-based methods for different flow speeds. *International Journal for Numerical Methods in Fluids*, 79(5):243–267, 2015.

[115] Ansys, inc. ANSYS Fluent User's Guide, August 2017. Release 18.2.

[116] F. P. Incropera. *Fundamentals of Heat and Mass Transfer*. John Wiley & Sons, Inc., USA, 2006.

[117] ESDU. Properties of a standard atmosphere(ESDU 77021). Technical report, 2008.

[118] NASA. Vectored thrust. Available at:https://www.grc.nasa.gov/www/k-12/airplane/vecthrst.html. Date acessed: 12 May 2019.

[119] Boeing. What is angle of attack. Available at:http://www.boeing.com/commercial/aeromagazine/. Date acessed: 15 September 2019.

[120] D. Fisher and R. Meyer. Flow Visualization Techniques for Flight Research. In *73rd AGARD Symposium of the Flight Mechanics Panel on Flight Test Techniques; October 17, 1988 - October 20, 1988; Edwards AFB, CA; United States.*, NASA-TM-100455, H-1524, NAS 1.15:100455, AGARD-PAPER-20. NASA, 1988.

[121] Shimmer. Consensys imu shimmer3. Available at:http://www.shimmersensing.com/products/shimmer3-development-kit. Date acessed: 1 September 2019.

[122] M. Brenckmann. Experimental investigation of the aerodynamics of a wing in a slipstream. *Journal of the Aeronautical Sciences*, 25(5):324–328, 1958.

[123] ESDU. Subsonic lift-dependent drag due to trailing vortex wake for wings without camber or twist , 1996. ESDU 74035.

[124] K. Biber. Estimating propeller slipstream drag on airplane performance. *Philosophical Transactions of the Royal Society of London*, 48(6):2172–2174.

[125] R. N. B.R. Rakshith, S.M. Deshpande. Optimal low-drag wing plan-forms for tractor-configuration propeller-driven aircraft. *J. Aircr.*, 52(6):2172–2174.

[126] F. Catalano. On the effects of an installed propeller slipstream on wing aerodynamic characteristics. *Acta Polytechnica*, 44:8–14, 01 2004.

[127] I. Rodríguez, O. Lehmkuhl, R. Borrell, and A. Oliva. Direct numerical simulation of a naca0012 in full stall. *International Journal of Heat and Fluid Flow*, 43:194 – 203, 2013.

[128] J. Katz and A. Plotkin. *Low-Speed Aerodynamics*. Cambridge Aerospace Series. Cambridge University Press, second edition, 2001.

Appendix A

Mesh Sensitivity Analysis

A.1 Mesh Size

Part	Maximum Size(m)	Tetra Ratio
Aileron Lower Surface	0.015624	1.2
Aileron Upper Surface	0.007812	1.2
Elevator Upper Surface	0.015624	1.2
Elevator Lower Surface	0.031248	1.2
Flap Upper Surface	0.007812	1.2
Flap Lower Surface	0.015624	1.2
Fuselage	0.0625	1.2
Spinner	0.031248	1.2
Rudder	0.031248	1.2
Strake Upper Surface	0.003906	1.2
Strake Lower Surface	0.031248	1.2
Horizontal Stabiliser	0.031248	1.2
Wing Upper Surface	0.015624	1.2
Wing Leading-Edge	0.015624	1.2
Wing Lower Surface	0.03125	1.2
Wing Tip	0.007812	1.2

Table A.1: Mesh maximum size for different parts for the coarse mesh.

Part	Maximum Size(m)	Tetra Ratio
Aileron Lower Surface	0.007812	1.2
Aileron Upper Surface	0.007812	1.2
Elevator Upper Surface	0.007812	1.2
Elevator Lower Surface	0.007812	1.2
Flap Upper Surface	0.007812	1.2
Flap Lower Surface	0.007812	1.2
Fuselage	0.03125	1.2
Spinner	0.015625	1.2
Rudder	0.031248	1.2
Strake Upper Surface	0.003906	1.2
Strake Lower Surface	0.031248	1.2
Horizontal Stabiliser	0.015625	1.2
Wing Upper Surface	0.07812	1.2
Wing Leading-Edge	0.007812	1.2
Wing Lower Surface	0.007812	1.2
Wing Tip	0.007812	1.2

Table A.2: Mesh maximum size for different parts for the medium mesh.

Part	Maximum Size(m)	Tetra Ratio
Aileron Lower Surface	0.007812	1.2
Aileron Upper Surface	0.007812	1.2
Elevator Upper Surface	0.007812	1.2
Elevator Lower Surface	0.007812	1.2
Flap Upper Surface	0.007812	1.2
Flap Lower Surface	0.007812	1.2
Fuselage	0.03125	1.2
Spinner	0.015625	1.2
Rudder	0.031248	1.2
Strake Upper Surface	0.003906	1.2
Strake Lower Surface	0.031248	1.2
Horizontal Stabiliser	0.015625	1.2
Wing Upper Surface	0.003906	1.2
Wing Leading-Edge	0.007812	1.2
Wing Lower Surface	0.007812	1.2
Wing Tip	0.007812	1.2

Table A.3: Mesh maximum size for different parts for the fine mesh.

A.2 Mesh Quality

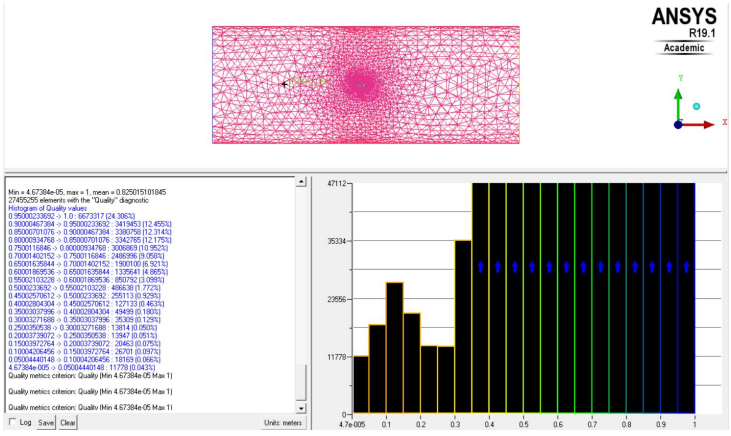

Figure A.1: Mesh Quality for the coarse mesh.

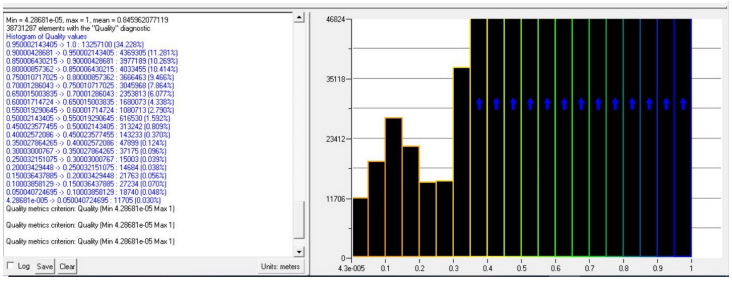

Figure A.2: Mesh Quality for the medium mesh.

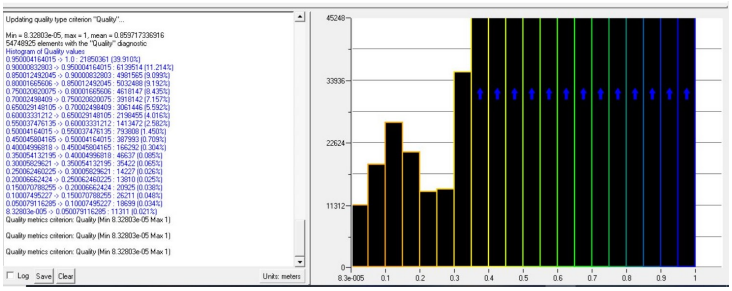

Figure A.3: Mesh Quality for the fine mesh.

A.3 Pressure Distribution

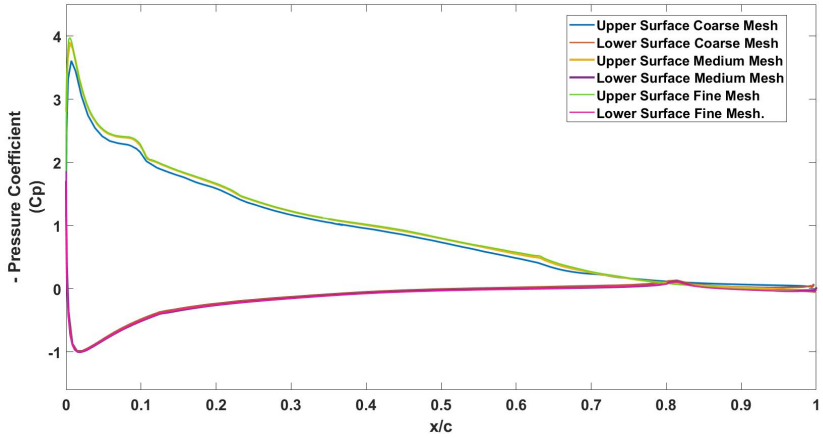

Figure A.4: Negative Pressure Coefficient as a function of the normalized chord of the AoA= 12° for the three mesh densities at a plane $z = 2.5m$.

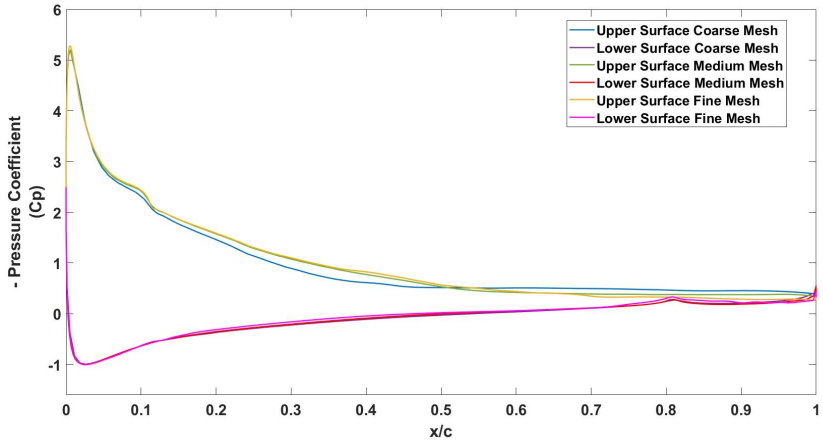

Figure A.5: Negative Pressure Coefficient as a function of the normalized chord of the AoA= 18° for the three mesh densities at a plane $z = 2.5m$.

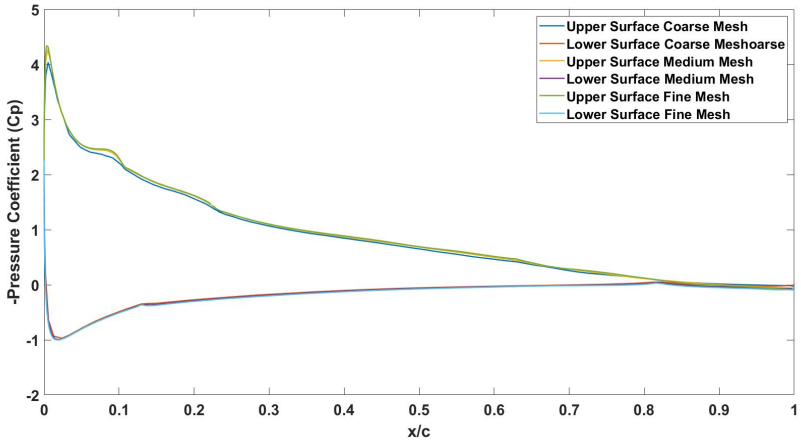

Figure A.6: Negative Pressure Coefficient as a function of the normalized chord of the AoA= 12° for the three mesh densities at a plane $z = 4m$.

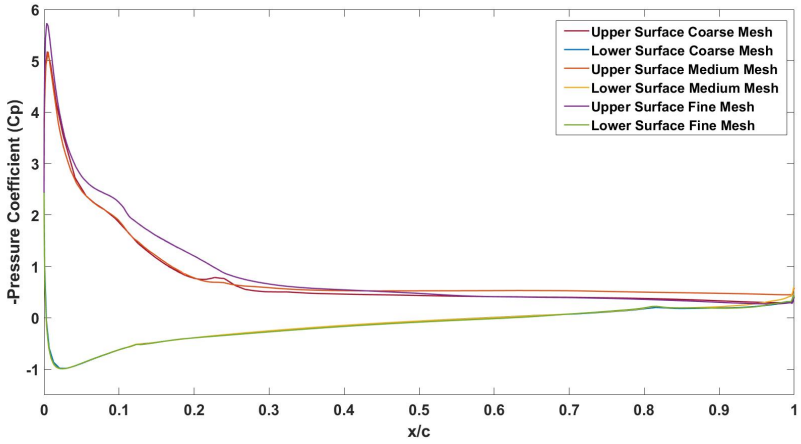

Figure A.7: Negative Pressure Coefficient as a function of the normalized chord of the AoA= 18° for the three mesh densities at a plane $z = 4m$.

Appendix B

Results

B.1 Wool tufts flight test

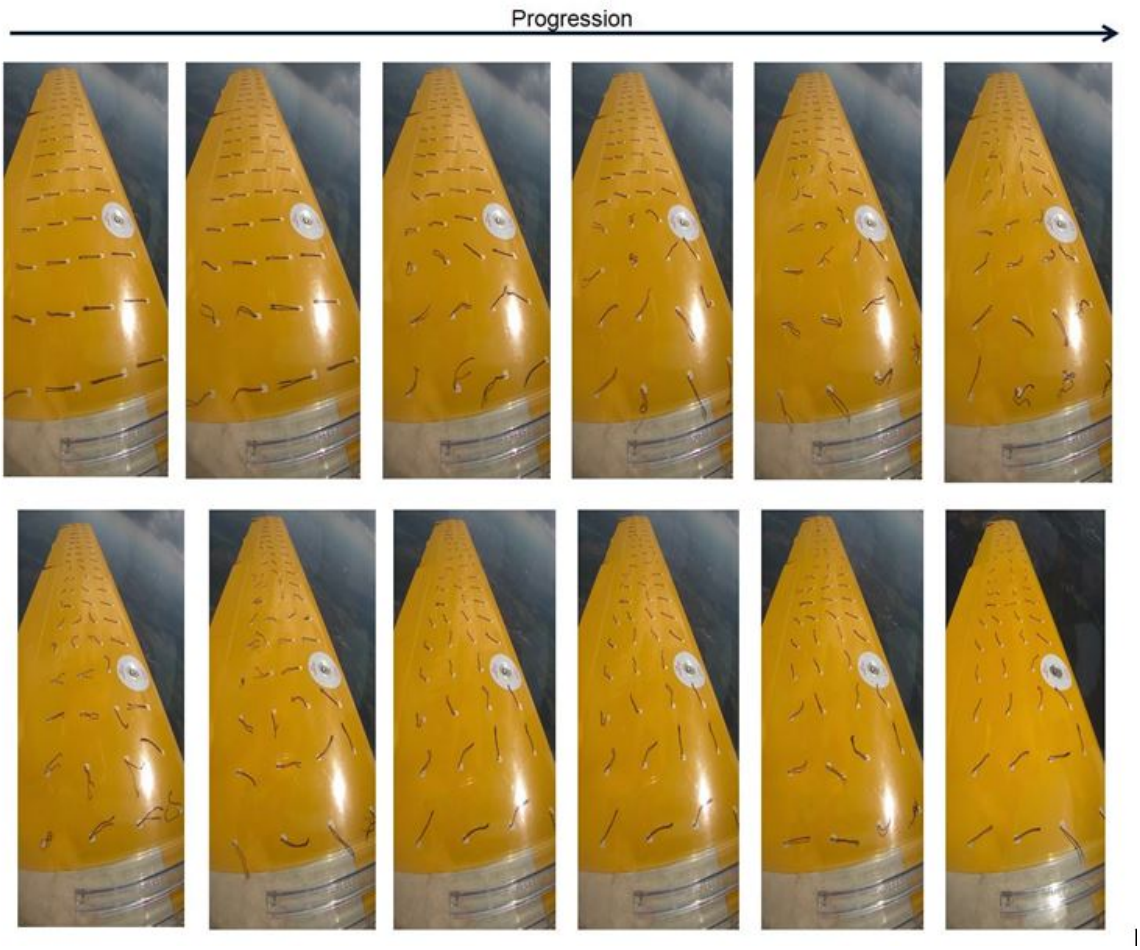

Figure B.1: Qualitative flow visualization using wool tufts during flight.

B.2 Vortex Shedding Frequency

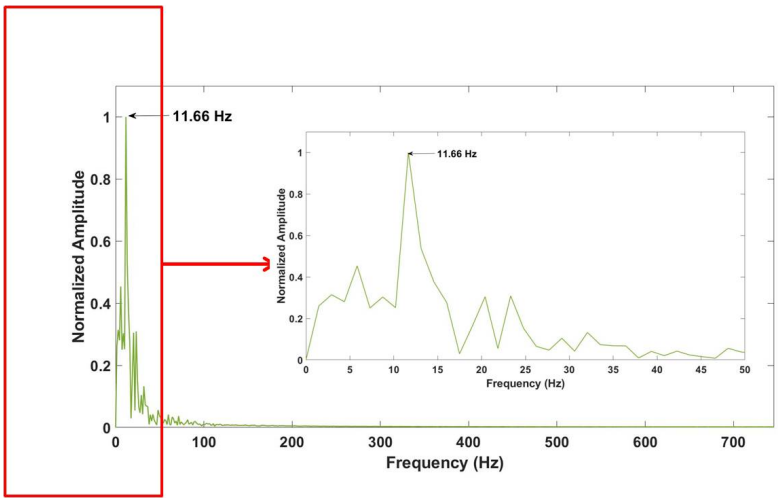

(a) **AoA = 14°**

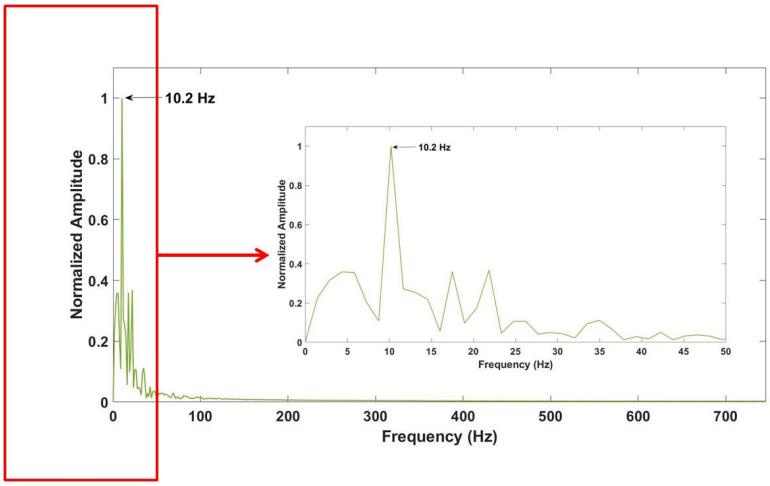

(b) **AoA = 16°**

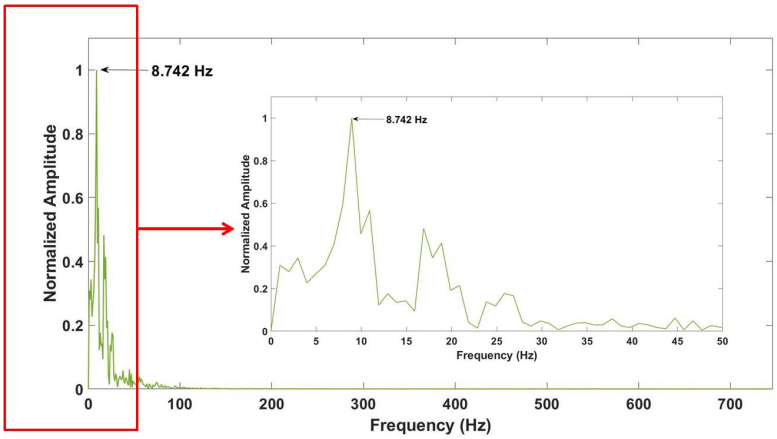

(c) **AoA = 18°**

Figure B.2: FFT analysis of P_{static} at point P10 for the different AoA studied .

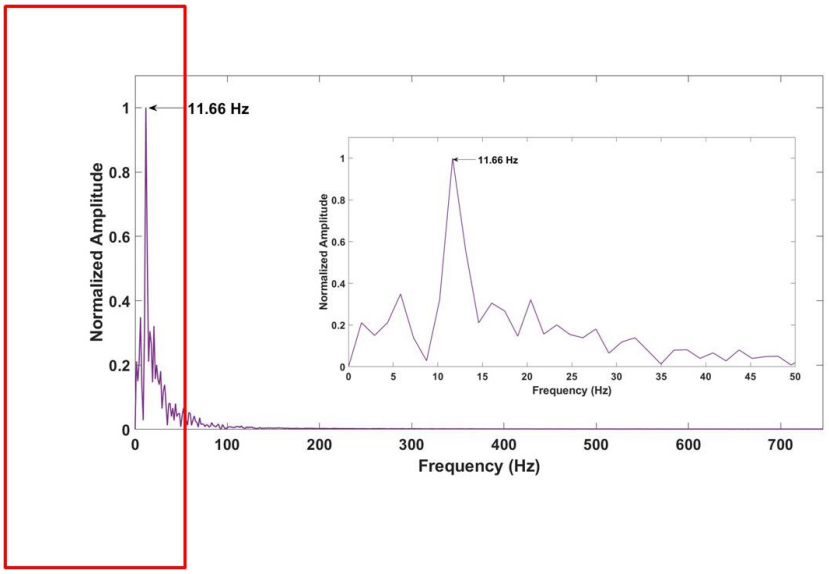

(a) **AoA = 14°**

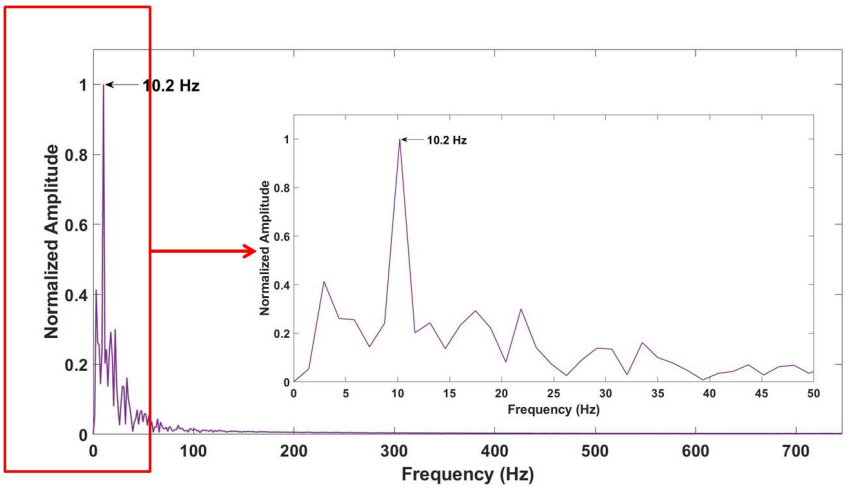

(b) **AoA = 16°**

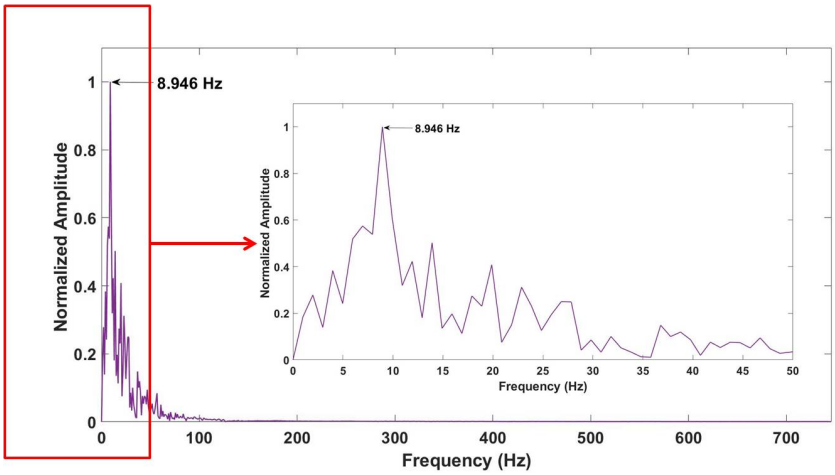

(c) **AoA = 18°**

Figure B.3: FFT analysis of P_{static} at point P14 for the different AoA studied .

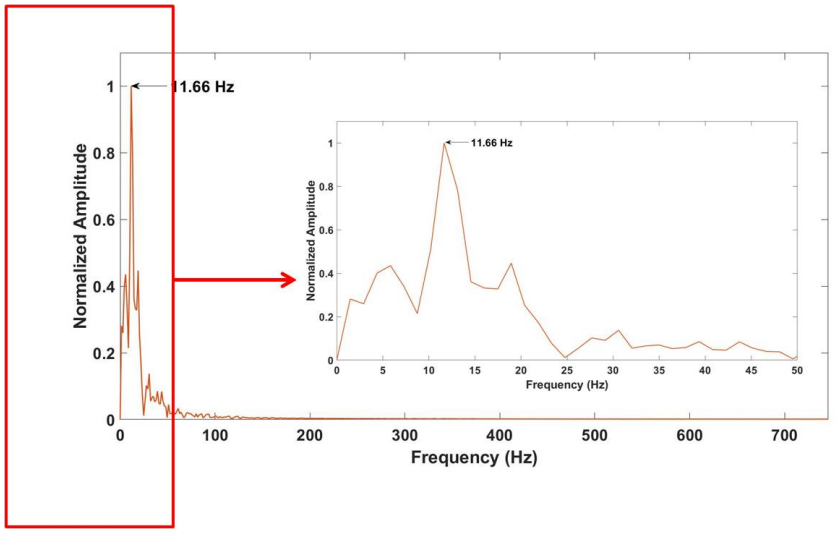

(a) **AoA = 14°**

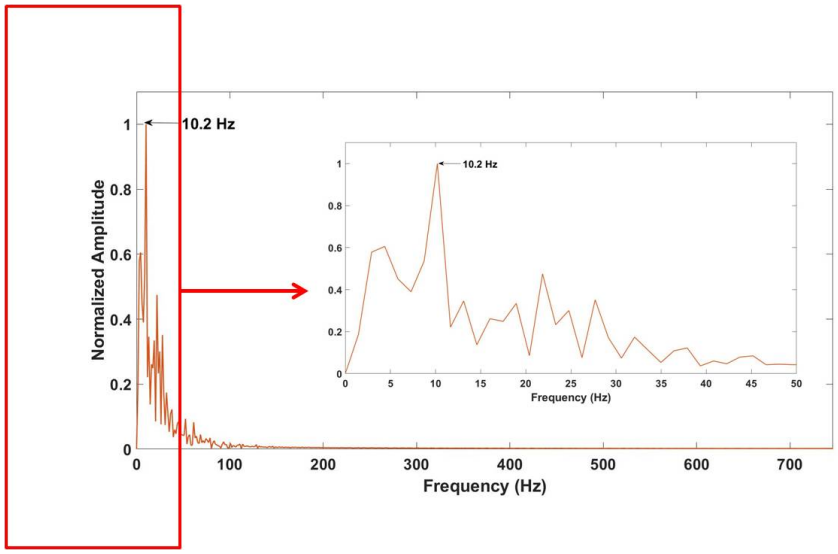

(b) **AoA = 16°**

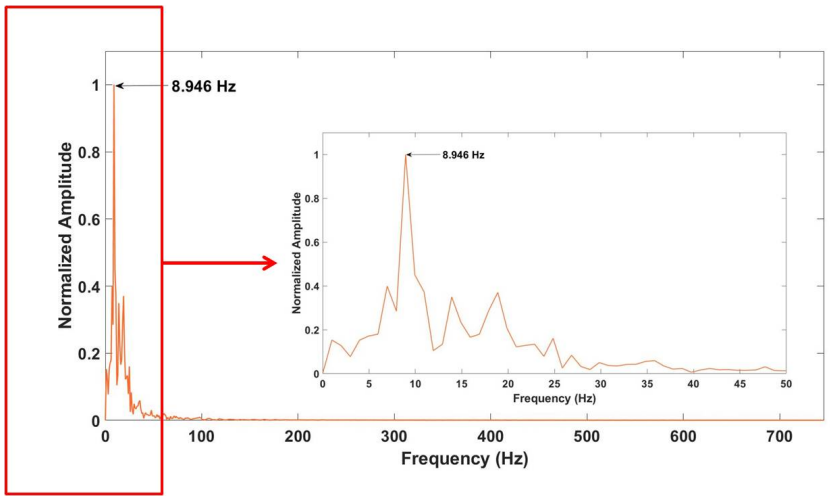

(c) **AoA = 18°**

Figure B.4: FFT analysis of P_{static} at point P15 for the different AoA studied .